Technische Universität München

Lehrstuhl für Experimentalphysik E18

Measurement of the electron antineutrino angular correlation coefficient *a* with the neutron decay spectrometer *a*SPECT

Martin Simson

Vollständiger Abdruck der von der Fakultät für Physik der Technischen Universität München zur Erlangung des akademischen Grades eines Doktors der Naturwissenschaften genehmigten Dissertation.

Vorsitzender:		Univ.-Prof. Dr. A. J. Buras
Prüfer der Dissertation:	1.	Univ.-Prof. Dr. O. Zimmer
	2.	Univ.-Prof. Dr. K. Schreckenbach

Die Dissertation wurde am 31.08.2010 bei der Technischen Universität München eingereicht und durch die Fakultät für Physik am 21.09.2010 angenommen.

Contents

1 Introduction

The current understanding of elementary particles and their interactions is described by the standard model (SM) of particle physics. This theory, developed since the 1960's, classifies the known elementary particles into two major groups, Quarks and Leptons. Each group is divided in three generations containing two particles each. Every particle has an antiparticle with the same mass but opposite charge.

Despite the huge success of the SM, it cannot answer all the questions that arise in modern particle physics.Among other shortcomings, the SM only describes three of the four known fundamental interactions: The strong, the weak, and the electromagnetic force. The SM does not contain gravity, furthermore it cannot explain the baryon asymmetry in the universe. Therefore the standard model, with its many parameters, might be a "low-energy" limit of a more general description of the physical world. One of the goals of modern experimental particle physics is to probe the SM in various different systems. The results of such experiments provide new input for theorists, but also allow to test the predictions of yet unproven theories beyond the SM, like for example super symmetry.

One such system is the neutron, it allows precision measurements which may indicate failures of the SM. In part, the information can be compared to results gained in high-energy, accelerator based experiments, but the neutron offers complementary results as well. For example, although the neutron is electrically neutral, it consists of charged constituents which might lead to a non zero electric dipole moment. Up to date all results of these studies are compatible with zero, still they already provided strong constraints on different theories beyond the SM [1].

Although the neutron is stable as long as it is bound in a nucleus, free

neutrons are unstable due to the slightly higher mass of the neutron n compared to the sum of the masses of the proton p and the electron e^-. It decays with a life time of about 15 minutes into a proton, an electron, and an electron antineutrino $\bar{\nu}_\mathrm{e}$:

$$n \rightarrow p + e^- + \bar{\nu}_\mathrm{e} + 782.3\,\mathrm{keV}. \tag{1.1}$$

The released energy is given by the differences of the masses of the neutron, proton, and electron [2].

In general, the decay of a nucleus into an electron, an antineutrino, and the daughter nucleus is called beta-minus (β^-) decay. The minus refers to the negative charge of the outgoing electron. The decay of the free neutron is the simplest form of a β^- decay. The daughter nucleus is a single proton, so no nuclear structure corrections are necessary.

Obviously, the life time is one of the measurable parameters in neutron decay. There are ongoing disputes about the exact value of the life time of the neutron, as there are only two published measurements with small error bars in the order of 1 s. Unfortunately those two results differ by about 6 standard deviations [3, 4]. Only further measurements with high statistics and clean systematics may resolve this conflict.

In the three body decay of the neutron one can define angular correlations between the participating particles and their spins [5]:

$$\frac{\mathrm{d}W(\vec{p_\mathrm{e}}, \vec{p_{\bar{\nu}}})}{\mathrm{d}\Omega_\mathrm{e}\mathrm{d}\Omega_{\bar{\nu}}\mathrm{d}E_\mathrm{e}} \propto 1 + b\frac{m_\mathrm{e}}{E_\mathrm{e}} + a\frac{\vec{p_\mathrm{e}} \cdot \vec{p_{\bar{\nu}}}}{E_\mathrm{e}E_{\bar{\nu}}} + \vec{P_\mathrm{n}} \cdot \left(A\frac{\vec{p_\mathrm{e}}}{E_\mathrm{e}} + B\frac{\vec{p_{\bar{\nu}}}}{E_{\bar{\nu}}} + D\frac{\vec{p_\mathrm{e}} \times \vec{p_{\bar{\nu}}}}{E_\mathrm{e}E_{\bar{\nu}}} \right) \tag{1.2}$$

where m_e is the mass of the electron, $\vec{p_{\bar{\nu}}}$, $\vec{p_\mathrm{e}}$, $E_{\bar{\nu}}$ and E_e the momenta and energies of antineutrino and electron, respectively. $\vec{P_\mathrm{n}}$ is the polarisation of the neutron.

The coefficients a, A, b, B, D can be determined experimentally as well as theoretically. Some of these coefficients explicitly violate parity or time reversal invariance or both. If one considers the spin of the outgoing electron further correlations can be defined. aSPECT aims to measure a, the angular correlation between the electron and the antineutrino which conserves both parity and time reversal invariance.

A direct measurement of a by measuring the electron and the antineutrino and inferring the angle between them is not possible, as the neutrino can

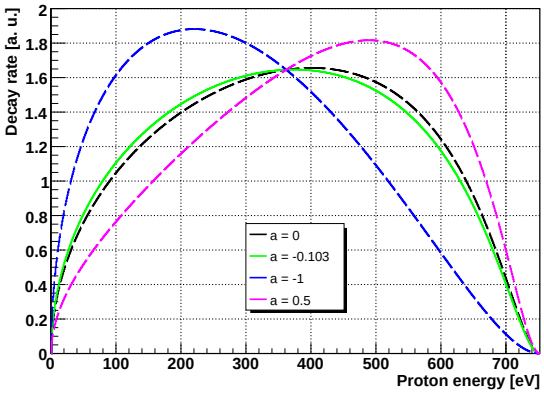

Figure 1.1: Expected proton spectra for different values of a.

hardly be detected. However, a can be extracted from the proton energy spectrum. Most of the released energy is carried away by the electron and the antineutrino, due to momentum conservation, the proton has a kinetic energy of 751 eV or less. Theoretical proton energy spectra for different values of a are shown in fig. 1.1.

The connection of the shape of the proton spectrum and a becomes visible if one considers the kinematics of two extreme cases of the decay: If electron and antineutrino are emitted with their momenta pointing in the same direction (this means $a = 1$), the proton will go in the opposite direction and carry a rather large momentum due to the law of momentum conservation. In the opposite extreme case, where electron and antineutrino are emitted anti-parallel ($a = -1$), the proton will carry rather low momentum and its energy spectrum will be shifted towards lower energies, as visible in fig. 1.1.

The experiment is done in a collaboration of several universities and institutes. The necessary tasks before, during, and after the beamtime were distributed mostly between four thesis students, three of them at the university of Mainz and me. Michael Borg was responsible for the collimation of the neutron beam and analysis of the data, Gertrud Konrad focussed on detailed simulations of the magnetic and electric fields and the flight paths of the decay particles inside the spectrometer. Fidel Ayala Guardia performed precise measurements of the magnetic field and developed an online

magnetometer.

This thesis mostly focusses on the proton detector and the analysis of the systematic effects concerning the detector. For details on the other parts of the spectrometer, the reader is referred to the other theses repeatedly throughout this work.

2 Theoretical background

In the following sections I will give a brief overview of the theory of the weak interaction and specifically the beta decay. The theory of the weak interaction is well-known and has been described in many textbooks and articles. For details on the theoretical background the reader is referred to the references given in the following sections.

2.1 Theory of β-decay

Neutron decay, as shown in eq. (1.1), as well as any other nuclear beta decay is a phenomenon of the weak interaction. In general it can be classified into two decay modes, depending on the transfer of angular momentum. If no angular momentum is transferred to the lepton, one speaks of an allowed decay, the case where the outgoing lepton carries angular momentum is called forbidden. As already implied by the terminology, decay channels with transfer of angular momentum are strongly suppressed.

The transfer of angular momentum can be regarded as a multipole expansion of the lepton wave function in terms of the product of momentum $|\vec{p}|$ and nuclear radius R. The momenta are of the order of few MeV/c and the nuclear radii of some 10^{-15} m, thus $|\vec{p}|R/\hbar$ is of the order of 10^{-2}. The decay probability is proportional to the square of this value, so every unit of transferred angular momentum results in a suppression of 10^{-4} to 10^{-3} [6].

Due to the small size of the free neutron ($\approx 1\,\mathrm{fm}$) and the rather low momentum transfer, its decay will be considered as a pure allowed decay in the following.

Both electron and antineutrino carry a spin, $\vec{\sigma}_\mathrm{e}$ and $\vec{\sigma}_{\bar{\nu}}$, respectively. Each

(a) (b)

Figure 2.1: Feynman graphs: a) An electron in an excited core emitting a photon. b) Neutron decay in Fermi's picture. The time arrow is pointing to the right.

spin is 1/2, thus they can couple to a total spin $\vec{S}$ of 0 or 1. If the spins couple to the singlet state $S = 0$, the transition is called Fermi decay. The transition to the triplet state $S = 1$ is called Gamow-Teller decay. Or, if we regard the spin $\vec{J}$ of the daughter nucleus (or proton in our case):

$$\Delta J = 0 \text{ Fermi decays}$$

$$\Delta J = 0, 1 \text{ Gamow} - \text{Teller decays}$$
$$(\text{ but not } 0 \rightarrow 0)$$

2.1.1 Fermi's theory

The weak interaction was initially discovered in β-decay, the first theory about it was proposed by Enrico Fermi in 1934 [7]. This phenomenological description was constructed in analogy to the theory of the electro-magnetic interaction. Fig. 2.1(a) shows the Feynman graph of the emission of an X-ray from an excited electron in an atom, fig. 2.1(b) the analogous view of neutron decay in Fermi's theory.

The coupling of the photon to the electron is given by the Hamiltonian

$$\mathcal{H} = e j_{\mu}^{\text{em}} \cdot A^{\mu}, \tag{2.1}$$

with the electron charge e, the 4-vector potential of the electromagnetic field A^μ, and the electromagnetic current density $j_\mu^{\mathrm{em}} = \bar{\Psi}_\mathrm{e}\gamma_\mu\Psi_\mathrm{e}$. Ψ_e is the electron spinor field function and $\bar{\Psi}_\mathrm{e}$ the corresponding adjoint function. $\gamma^\mu = (\gamma^0, \gamma^1, \gamma^2, \gamma^3)$ are the γ-matrices[1].

Fermi assumed a point like interaction between the particles participating in neutron decay in his theory and replaced the 4-vector potential by a leptonic current, the electromagnetic by a hadronic current, and the electric charge e by the Fermi coupling constant G_F:

$$A^\mu \rightarrow J_\mu^{\mathrm{lep}} = \bar{\Psi}_\mathrm{e}\gamma_\mu\Psi_{\bar{\nu}} \tag{2.2}$$

$$j_\mu^{\mathrm{em}} \rightarrow J_\mu^{\mathrm{had}} = \bar{\Psi}_\mathrm{p}\gamma_\mu\Psi_\mathrm{n} \tag{2.3}$$

$$e \rightarrow \frac{G_\mathrm{F}}{\sqrt{2}} \tag{2.4}$$

The Fermi coupling constant can be determined with high accuracy from muon decay, $G_\mathrm{F}/(\hbar c)^3 = 1.16637(1)\ \mathrm{GeV}^{-2}$ [2]. In analogy to eq. (2.1) the Hamiltonian density for the beta decay can now be written as

$$\mathcal{H} = \frac{G_\mathrm{F}}{\sqrt{2}} J_\mu^\dagger \cdot J^\mu + \mathrm{h.c.} \tag{2.5}$$

h.c. stands for the hermitian conjugate, the current J_μ is the sum of the hadronic and the leptonic part:

$$J_\mu = J_\mu^{\mathrm{had}} + J_\mu^{\mathrm{lep}}. \tag{2.6}$$

In its original form, Fermi's theory explicitly conserves parity, but in 1956 parity violation in β-decay was postulated by Lee and Yang [8] and demonstrated by Wu *et al.* [9] in the decay of ^{60}Co shortly after. In this experiment radioactive cobalt 60 atoms were kept at a low temperature with their spins aligned along the direction of a strong magnetic field and the direction of emission of the beta electrons was observed. Wu *et al.* were able to show that the electrons are preferentially emitted in a direction opposite to the direction of the nuclear spin. Other experiments confirmed this discovery. Thus Fermi's theory was expanded to the $V - A$ theory.

[1] $\gamma^0 = \begin{pmatrix} \mathbf{I} & 0 \\ 0 & \mathbf{I} \end{pmatrix}$, $\vec{\gamma} = \begin{pmatrix} 0 & \vec{\sigma} \\ -\vec{\sigma} & 0 \end{pmatrix}$, $\gamma^5 = i\gamma^0\gamma^1\gamma^2\gamma^3$, $\vec{\sigma}$ are the Pauli matrices.

2.1.2 $V - A$ theory

A more general form of the Hamiltonian in neutron decay can be constructed by including all possible interaction terms which are invariant under Lorentz-, parity-, and time-reversal transformation. As shown by Gamov and Teller in 1936 [10], one can create 16 linear independent 4×4 matrices from the γ-matrices:

Operator	Name	Number of matrices
$\bar{\Psi}\Psi$	Scalar (S)	1
$\bar{\Psi}\gamma_\mu\Psi$	Vector (V)	4
$\bar{\Psi}\gamma_\mu\gamma^\nu\Psi$	Tensor (T)	6
$\bar{\Psi}\gamma_5\Psi$	Pseudoscalar (P)	1
$\bar{\Psi}\gamma_5\gamma_\mu\Psi$	Axial-vector (A)	4

Table 2.1: The five possible current-current interactions.

With these operators the Hamiltonian can be written in its most general form as [11]

$$\begin{aligned}\mathcal{H} = 2\frac{G_\mathrm{W}}{\sqrt{2}} \sum_i \Big(& L_i \left(\bar{\Psi}_\mathrm{p}\Gamma_i\Psi_\mathrm{n}\right) \cdot \left(\bar{\Psi}_\mathrm{e}\Gamma_i(1-\gamma_5)\Psi_{\bar{\nu}}\right) + \\ & + R_i \left(\bar{\Psi}_\mathrm{p}\Gamma_i\Psi_\mathrm{n}\right) \cdot \left(\bar{\Psi}_\mathrm{e}\Gamma_i(1+\gamma_5)\Psi_{\bar{\nu}}\right)\Big) + \mathrm{h.c.}\end{aligned} \tag{2.7}$$

G_W is a general weak coupling constant, $i \in [S, V, T, P, A]$ and the operators Γ_i correspond to the interactions given in table 2.1:

$$\Gamma_\mathrm{S} = 1; \quad \Gamma_\mathrm{V} = \gamma_\mu; \quad \Gamma_\mathrm{T} = -i\frac{[\gamma_\mu, \gamma_\nu]}{2\sqrt{2}}; \quad \Gamma_\mathrm{P} = \gamma_5; \quad \Gamma_\mathrm{A} = -i\gamma_\mu\gamma_5. \tag{2.8}$$

Eq. (2.7) is constructed in a way that the first part of the sum corresponds to left-handed and the second part to right-handed[2] currents. The coupling constants for the left-handed part L_i and the right-handed part R_i have to be determined experimentally. $(1-\gamma_5)\Psi_\nu/2$ and $(1+\gamma_5)\Psi_\nu/2$ are the left-

[2]Left-handed particles are those with helicity $h = \frac{\vec{s}\cdot\vec{p}}{|\vec{s}|\cdot|\vec{p}|} = 1$, particles with $h = -1$ are right-handed.

handed and right-handed projections of the antineutrino wave functions, respectively. The Hamiltonian violates parity if $L_i \neq R_i$, time reversal invariance is violated if the coupling constants have a relative complex phase.

Fermi transitions do not change the spin ($\Delta J = 0$) and are mediated by scalar and vector couplings, whereas axial-vector and tensor couplings contribute to Gamow-Teller transitions.

So far parity violation in the weak interaction was found to be maximal by all experiments, this means only left-handed components of vector and axial-vector couplings contribute to beta decay and eq. (2.7) can be simplified to the Hamiltonian of the $V - A$ theory:

$$\begin{aligned} \mathcal{H} &= \frac{G_\mathrm{W}}{\sqrt{2}} \sum_{\mathrm{V,A}} L_i \left(\bar{\Psi}_\mathrm{p} \Gamma_i \Psi_\mathrm{n}\right) \cdot \left(\bar{\Psi}_\mathrm{e} \Gamma_i (1-\gamma_5) \Psi_{\bar{\nu}}\right) + \mathrm{h.c.} \\ &= g_\mathrm{V} (\bar{\Psi}_\mathrm{p} \gamma_\mu (1 + \lambda \gamma_5) \Psi_\mathrm{n}) \cdot (\bar{\Psi}_\mathrm{e} \gamma_\mu (1-\gamma_5) \Psi_{\bar{\nu}}) + \mathrm{h.c.} \end{aligned} \tag{2.9}$$

g_V and g_A are the vector and axial-vector coupling constants and λ is their ratio:

$$g_\mathrm{V} = G_\mathrm{W} L_\mathrm{V}, \quad g_\mathrm{A} = G_\mathrm{W} L_\mathrm{A}, \quad \lambda = \frac{g_\mathrm{A}}{g_\mathrm{V}}. \tag{2.10}$$

2.1.3 Standard model

Although the Hamiltonian in eq. (2.9) describes the parity violation in beta decay, it still assumes a point-like interaction. However, it was discovered that neutrons and protons are not elementary particles, but are composed of quarks. This, among other discoveries, lead to the formulation of the so-called standard model of particle physics. The fundamentals for this theory were developed by Salam, Glashow, and Weinberg in the 1960s [12, 13, 14].

The standard model follows the $V - A$ theory, except the beta decay is no longer a point-like interaction, but it is described by the exchange of a $W^\pm$ boson between the leptonic and the hadronic current. In general, the weak interaction is mediated by the exchange of the bosons $W^\pm$ and Z^0.

In the case of small momentum transfers the exchange bosons are very heavy and thus can only exist for very short times, determined by Heisenberg's relation of uncertainty $\tau < \hbar / M_{\mathrm{W,Z}}$. With $M_\mathrm{W} = 80.398(25)\,\mathrm{GeV}/c^2$ and $M_\mathrm{Z} = 91.1876(21)\,\mathrm{GeV}/c^2$ [2] and assuming the speed of light c as

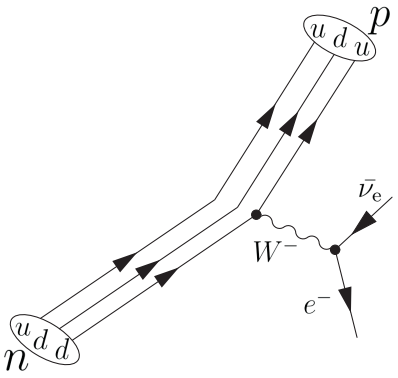

Figure 2.2: Feynman graph of neutron decay in the standard model a neutron (udd) decays into proton (uud), electron and antineutrino by the exchange of a $W^{\pm}$ boson.

maximum speed, the interaction has a range of $\sim 2.5 \cdot 10^{-18}$ m. Thus the point-like $V - A$ model for beta decay is included as low energy limit in the standard model. Furthermore, in the standard model proton and neutron are composed of up and down quarks and beta decay converts a down into an up quark.

The standard model groups the six known quarks into three families, depending on their charges and masses:

$$\begin{pmatrix} u \\ d \end{pmatrix}, \quad \begin{pmatrix} c \\ s \end{pmatrix}, \quad \begin{pmatrix} t \\ b \end{pmatrix}. \tag{2.11}$$

The quarks have a charge of $+2/3$ in the upper row and $-1/3$ in the lower row. Most transitions between the quarks happen within one family, but due to the weak interaction also decays between families are observed. The eigenstates of the weak interaction are not the mass eigenstates, but can be written for the first two families as a rotation matrix with sine and cosine of the Cabibbo angle [15] θ_C:

$$\begin{pmatrix} |d'\rangle \\ |s'\rangle \end{pmatrix} = \begin{pmatrix} \cos\theta_C & \sin\theta_C \\ -\sin\theta_C & \cos\theta_C \end{pmatrix} \cdot \begin{pmatrix} |d\rangle \\ |s\rangle \end{pmatrix}, \tag{2.12}$$

where the primed values ($|d'\rangle$ and $|s'\rangle$) are the eigenstates of the weak

interaction and the unprimed values the mass eigenstates.

Later the third generation of quarks was found and eq. (2.12) was extended to a 3×3 matrix, the Cabibbo-Kobayashi-Maskawa (CKM) matrix [16]:

$$\begin{pmatrix} |d'\rangle \\ |s'\rangle \\ |b'\rangle \end{pmatrix} = \begin{pmatrix} V_{\mathrm{ud}} & V_{\mathrm{us}} & V_{\mathrm{ub}} \\ V_{\mathrm{cd}} & V_{\mathrm{cs}} & V_{\mathrm{cb}} \\ V_{\mathrm{td}} & V_{\mathrm{ts}} & V_{\mathrm{tb}} \end{pmatrix} \cdot \begin{pmatrix} |d\rangle \\ |s\rangle \\ |b\rangle \end{pmatrix}. \tag{2.13}$$

The squares of the single matrix elements $|V_{\mathrm{qq'}}|^2$ describe the probability of the transition of a quark $|q\rangle$ to $|q'\rangle$. To take this into account for beta decay, the coupling constants get an additional factor $|V_{\mathrm{ud}}|$:

$$G_{\mathrm{V}} = g_{\mathrm{V}} \cdot |V_{\mathrm{ud}}|, \qquad G_{\mathrm{A}} = g_{\mathrm{A}} \cdot |V_{\mathrm{ud}}|. \tag{2.14}$$

The standard model assumes that there are only three quark generations, thus the CKM matrix has to be unitary. This means the sum of the squares of each row has to be equal to one, for example, for the first row:

$$|V_{\mathrm{ud}}|^2 + |V_{\mathrm{us}}|^2 + |V_{\mathrm{ub}}|^2 = 1. \tag{2.15}$$

With this conditions, the measured limits for the elements of the matrix are [2]:

(2.16)

$$(|V_{ij}|) = \begin{pmatrix} 0.97419 \pm 0.00022 & 0.2257 \pm 0.0010 & 0.00359 \pm 0.00016 \\ 0.2256 \pm 0.0010 & 0.97334 \pm 0.00023 & 0.0415^{+0.0010}_{-0.0011} \\ 0.00874^{+0.00026}_{-0.00037} & 0.0407 \pm 0.0010 & 0.999133^{+0.000044}_{-0.000043} \end{pmatrix}.$$

2.2 Measurable parameters in neutron decay

To calculate the total decay probability, Fermi's golden rule can be used:

$$W = \frac{2\pi}{\hbar} |\mathcal{M}_{\mathrm{fi}}|^2 \cdot \rho'_{\mathrm{e}}(E_{\mathrm{e}}), \tag{2.17}$$

where $\rho'_{\mathrm{e}}(E_{\mathrm{e}})$ is the phase space density of the final states and $\mathcal{M}_{\mathrm{fi}}$ is the transition matrix element. With the Hamiltonian given in eq. (2.9) it can be expressed as a function of the coupling constants. For beta decay this was done by J.D. Jackson *et al.* in 1957 [5] and the distribution of electron and antineutrino energies (E_{e} and E_{ν}, respectively) and momenta ($\vec{p_{\mathrm{e}}}$, $\vec{p_{\nu}}$) was calculated to be

$$\begin{aligned} \frac{dW}{dE_{\mathrm{e}}d\Omega_{\mathrm{e}}d\Omega_{\bar{\nu}}} &= \frac{G_{\mathrm{W}}^2}{(2\pi)^4\hbar}\rho'_{\mathrm{e}}(E_{\mathrm{e}})\xi \cdot \\ &\cdot \left\{ 1 + a\frac{\vec{p_{\mathrm{e}}}\vec{p_{\bar{\nu}}}}{E_{\mathrm{e}}E_{\bar{\nu}}} + b\frac{m_{\mathrm{e}}}{E_{\mathrm{e}}} + \frac{\vec{P}_{\mathrm{n}}}{P_{\mathrm{n}}} \cdot \left(A\frac{\vec{p_{\mathrm{e}}}}{E_{\mathrm{e}}} + B\frac{\vec{p_{\bar{\nu}}}}{E_{\bar{\nu}}} + D\frac{\vec{p_{\mathrm{e}}} \times \vec{p_{\bar{\nu}}}}{E_{\mathrm{e}}E_{\bar{\nu}}} \right) + \dots \right\}. \end{aligned} \tag{2.18}$$

Jackson *et al.* derived two more correlation coefficients which are not important for the following discussion and thus are not shown. ξ is the sum of the squares of the coupling constants, as presented in general form in [11]:

$$\begin{aligned} \xi = &\left(|L_{\mathrm{S}}|^2 + |L_{\mathrm{V}}|^2 + |R_{\mathrm{S}}|^2 + |R_{\mathrm{V}}|^2\right) + \\ &3\left(|L_{\mathrm{A}}|^2 + |L_{\mathrm{T}}|^2 + |R_{\mathrm{A}}|^2 + |R_{\mathrm{T}}|^2\right). \end{aligned} \tag{2.19}$$

The pre-factor 3 of the second part of eq. 2.19 indicates the triplet state of the Gamow-Teller decay mediated by axial-vector and tensor couplings, in contrast to the singlet state of the Fermi decay (scalar and vector type couplings).

Within the standard model the equation simplifies to

$$\xi = |L_{\mathrm{V}}|^2 + 3|L_{\mathrm{A}}|^2, \tag{2.20}$$

or, with the commonly known coupling constants of the weak interaction from eq. (2.10):

$$\xi = \frac{|g_{\mathrm{V}}|^2 + 3|g_{\mathrm{A}}|^2}{G_{\mathrm{W}}^2}. \tag{2.21}$$

Each of the correlation coefficients a, b, A, B, D can now be expressed as a function of the coupling constants L_i, R_i,. In the standard model a, A, B, D depend only on the ratio of the coupling constants λ and $b = 0$. From a measurement of one of the parameters one can infer $|\lambda|$,

measuring several parameters allows to cross-check the results for the different measurements to avoid unknown systematic effects.

Using the world average for $\lambda = -1.2694(28)$ [2] the sensitivities towards λ for the single parameters are

$$\frac{da}{d\lambda} = 0.298, \qquad \frac{dA}{d\lambda} = 0.374, \qquad \frac{dB}{d\lambda} = 0.076. \tag{2.22}$$

A offers the best sensitivity towards λ and the most precise values for it from neutron decay have been retrieved by measuring this angular correlation between neutron spin and electron momentum. The most precise value for $A = 0.1189(7)$ was measured by the Perkeo II experiment [17] but is not in good agreement with previous experiments. Thus the error bar of the world average value was increased to a value of $A = 0.1173(13)$ [2]. Although a is slightly less sensitive to λ it still offers a good possibility for a systematically independent measurement of λ. However, the experimental relative uncertainty of a is much bigger than for A. The present world average value is $a = -0.103(4)$ [2].

aSPECT aims to measure the electron antineutrino angular correlation a, thus only this parameter will be discussed here, for information on the other parameters the reader is referred to [11].

In general a takes the form

$$a = \frac{1}{\xi}\left(|L_{\mathrm{V}}|^2 - |L_{\mathrm{S}}|^2 + |L_{\mathrm{T}}|^2 - |L_{\mathrm{A}}|^2 + |R_{\mathrm{V}}|^2 - |R_{\mathrm{S}}|^2 + |R_{\mathrm{T}}|^2 - |R_{\mathrm{A}}|^2\right), \tag{2.23}$$

in the standard model

$$a = \frac{1 - |\lambda|^2}{1 + 3|\lambda|^2}. \tag{2.24}$$

Eq. (2.23) shows that a non zero value for a does not violate parity, as it does not contradict $L_i = R_i$, nor does it violate time reversal invariance.

Besides the calculation of λ, a measurement of a can be used to search for contributions of scalar and tensor type interactions to the decay.

Experimentally a is more difficult to measure than A, as it cannot be directly measured due to the difficulty of detecting neutrinos. Thus a has to

be inferred from other experimentally accessible properties. So far only two ways have been realised. The aCORN experiment plans to determine a by comparing the coincidence rates of electron and proton for two kinematically distinct regions corresponding to $\vec{p_\mathrm{p}} \uparrow\uparrow \vec{p_\mathrm{e}}$ and $\vec{p_\mathrm{p}} \uparrow\downarrow \vec{p_\mathrm{e}}$ [18]. The arrows indicate the projection of the momenta on the axis of the spectrometer. The second option is to measure the shape of the proton spectrum as described in sect. 1. This method is used by aSPECT as well as the three previous experiments which are taken into consideration for the world average value [19, 20, 21].

2.3 Kinematics

In a general view, neutron decay is a three-body decay, as shown in fig. 2.3 one ingoing particle decays into three outgoing ones. The particles have

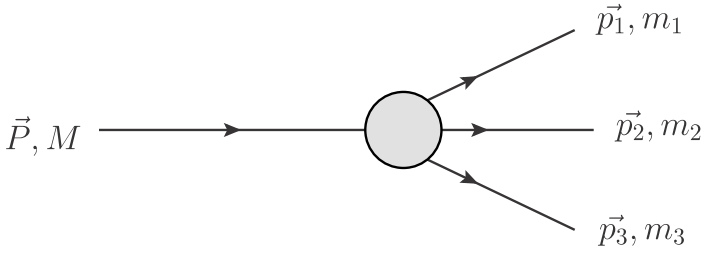

Figure 2.3: General three-body decay: The ingoing particle with momentum $\vec{P}$ and Mass M decays into three particles with momenta $\vec{p_\mathrm{i}}$ and masses m_i, with $\mathrm{i} \in (1, 2, 3)$.

to be treated relativistically with their four-momenta $p_\mathrm{i} = (E_\mathrm{i}, \vec{p_\mathrm{i}})$. If we write the sum of two four-momenta as $p_\mathrm{ij} := p_\mathrm{i} + p_\mathrm{j}$ and define $m_\mathrm{i}^2 := p_\mathrm{ij}^2$, according to [2], we can express the absolute value of the momentum of the third particle as

$$|\vec{p_3}| = \frac{\left[(M^2 - (m_{12} + m_3)^2) \cdot (M^2 - (m_{12} - m_3)^2)\right]^{1/2}}{2M}. \tag{2.25}$$

p_3 becomes maximal if the particles one and two have the same vector velocity, this means $m_{12} = m_1 + m_2$. Using the well known masses of

the particles participating in neutron decay, the endpoints of the energy spectra of the daughter particles can be calculated with the relativistic energy-momentum relation in natural units:

$$E_{0,i} = \sqrt{m_{0,\mathrm{i}}^2 + |\vec{p}_\mathrm{i}|^2}, \tag{2.26}$$

where $E_{0,i}$ is the endpoint energy and $m_{0,\mathrm{i}}$ the rest mass of the respective particle, with $\mathrm{i} \in (\mathrm{p}, \mathrm{e}, \bar{\nu}_\mathrm{e})$. The resulting values for the different particles are shown in table 2.2.

Particle	Index i	$m_{0,\mathrm{i}}$ [MeV]	$E_{0,\mathrm{i}}$ [MeV]	$E_{0,\mathrm{i}} - m_{0,\mathrm{i}}$ [MeV]
Neutron	n	939.565346(23)		
Proton	p	938.272013(23)	938.272764(23)	0.000751(33)
Electron	e	0.510998910(13)	1.292581(53)	0.781582(53)
antineutrino	$\bar{\nu}_\mathrm{e}$	<0.000002	0.782008(54)	0.782008(54)

Table 2.2: Rest mass $m_{0,\mathrm{i}}$, endpoint energies $E_{0,\mathrm{i}}$, and resulting maximal kinetic energy for the neutron and its daughter particles.

2.3.1 Lepton spectra

The energy distribution of the decay particles depends on the available phase space. If we neglect the proton recoil, the electron energy spectrum can be calculated from the number of states in a given phase space volume $\mathrm{d}^3p_\mathrm{e}\mathrm{d}^3p_{\bar{\nu}}$. Using the energy relation $E_0 := E_\mathrm{e} + E_{\bar{\nu}} = m_\mathrm{n} - m_\mathrm{p}$ [6] the electron spectrum becomes

$$\mathrm{d}\rho_\mathrm{e} = \frac{(4\pi)^2}{(2\pi\hbar)^6} E_\mathrm{e}\sqrt{E_\mathrm{e}^2 - m_\mathrm{e}^2} \cdot (E_0 - E_\mathrm{e})^2 \mathrm{d}E_\mathrm{e}, \tag{2.27}$$

where E_0 is slightly larger than the value $E_{0,\mathrm{e}}$ given in table 2.2. For the further calculations the more accurate value $E_{0,\mathrm{e}}$ will be used.

To take the Coulomb interaction of the outgoing electron and proton into account, the spectrum has to be corrected with the Fermi function $F(Z, E)$. For non-relativistic electrons in the field of a point-like proton it is given

by [6]

$$F(E) = \frac{2\pi\eta}{1 - e^{2\pi\eta}}, \quad \text{with} \quad \eta = \frac{\alpha}{v_\mathrm{e}}. \tag{2.28}$$

α is the fine structure constant and v_e the velocity of the electron in units of c. This correction mostly affects low energetic electrons, eq. (2.27) is modified to

$$\rho'(E_\mathrm{e}) = \frac{(4\pi)^2}{(2\pi\hbar)^6} F(E) E_\mathrm{e} \sqrt{E_\mathrm{e}^2 - m_\mathrm{e}^2} \cdot (E_{0,\mathrm{e}} - E_\mathrm{e})^2. \tag{2.29}$$

Analogous to eq. (2.27), the neutrino spectrum can be calculated:

$$\rho'(E_{\bar{\nu}}) = \frac{(4\pi)^2}{(2\pi\hbar)^6} \sqrt{(E_{0,\bar{\nu}} + m_\mathrm{e} - E_{\bar{\nu}})^2 - m_\mathrm{e}^2} \cdot (E_{0,\bar{\nu}} + m_\mathrm{e} - E_{\bar{\nu}}). \tag{2.30}$$

Both electron and neutrino spectrum are plotted in fig. 2.4.

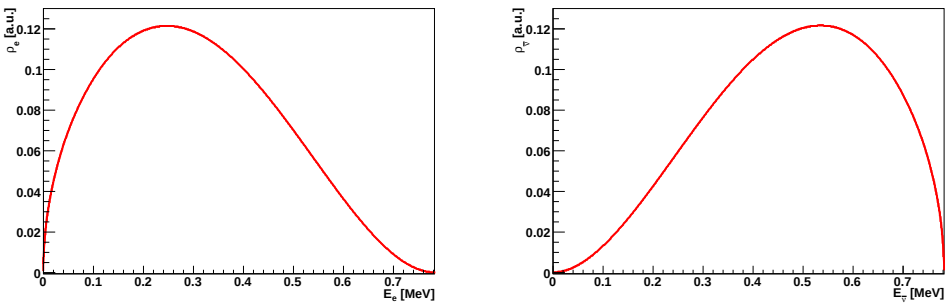

(a) (b)

Figure 2.4: Energy spectra of electrons (a) and neutrinos (b) from the decay of the free neutron ($F(E) = 1$).

2.3.2 Proton spectrum

The shape of the proton spectrum was relativistically derived by O. Nachtmann [22][3]. Similar to the derivation of the electron spectrum, the transition probability is a product of a phase space factor, a matrix element, and a Coulomb correction factor. Neglecting the latter, the proton spectrum becomes

$$\begin{aligned} \mathrm{d}W(T) = \frac{\Sigma\Delta^3 G_{\mathrm{V}}^2}{16\pi^3(1+2\delta)} \left(\frac{\sigma-x^2}{\sigma}\right)^2 \sqrt{1-\sigma} \left\{ \left(1+\frac{x^2}{\sigma}-\sigma\right) - \right. \\ \left. -\frac{1}{3}\frac{\sigma-x^2}{\sigma}(1-\sigma) + \lambda^2 \left[\left(1+\frac{x^2}{\sigma}+\sigma\right) - \frac{1}{3}\frac{\sigma-x^2}{\sigma}(1-\sigma) \right] \right\} \mathrm{d}T, \end{aligned} \tag{2.31}$$

where T is the kinetic energy of the proton, λ the ratio of the coupling constants as introduced in eq. (2.10), and

$$\begin{aligned} \Sigma &= m_{\mathrm{n}} + m_{\mathrm{p}} & \Delta &= m_{\mathrm{n}} - m_{\mathrm{p}}, \\ \delta &= \Delta/\Sigma & \sigma &= 1 - 2T \cdot m_{\mathrm{n}}/\Delta^2, \\ x &= m_{\mathrm{e}}/\Delta. \end{aligned} \tag{2.32}$$

The theoretical proton spectrum can be decomposed into a linear combination of a part dependent on a and an independent part [24]:

$$\frac{\mathrm{d}W(T)}{\mathrm{d}T} \propto g_1 + a g_2, \tag{2.33}$$

with

$$g_1 = \left(\frac{\sigma-x^2}{\sigma}\right)^2 \sqrt{1-\sigma} \cdot \left[4\left(1+\frac{x^2}{\sigma}\right) - \frac{4}{3}\left(\frac{\sigma-x^2}{\sigma}(1-\sigma)\right) \right],$$

and

$$g_2 = \left(\frac{\sigma-x^2}{\sigma}\right)^2 \sqrt{1-\sigma} \cdot \left[4\left(1+\frac{x^2}{\sigma}-2\sigma\right) - \frac{4}{3}\left(\frac{\sigma-x^2}{\sigma}(1-\sigma)\right) \right],$$

[3] A sign error was found in that paper by C. Habeck [23].

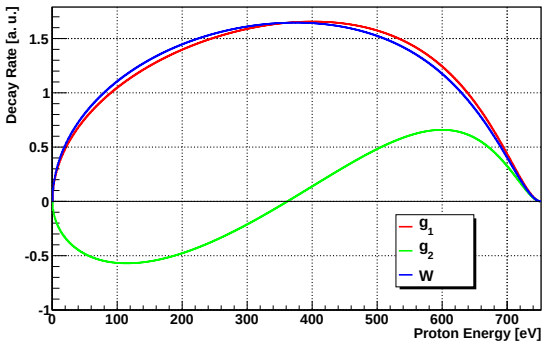

Figure 2.5: The theoretical functions g_1 and g_2 for the proton spectrum and the linear combination of them for the present world average value of $a = -0.103$.

In eq. (2.33) a gives the contribution of the function g_2 to the overall proton spectrum $W(T)$. The shapes of g_1, g_2, and the linear combination of them for the present world average value for a are shown in fig. 2.5.

3 Description of the spectrometer

The spectrometer was already described in detail in my Diploma thesis [25]. I am going to follow the argumentation therein closely and will update changes to the spectrometer.

As indicated in fig. 3.1, a beam of unpolarised, cold neutrons passes through the spectrometer which is essentially cylindrically symmetric. Statistically about 10^{-8} of the neutrons in the beam decay in a region close to the vertical axis of the spectrometer where the *decay volume* is situated. Protons produced in this decay volume are guided by a strong magnetic field perpendicular to the direction of the neutron beam and gyrate around a magnetic field line either in the direction of the proton detector on top of the setup or in the opposite direction where they are reflected by a electrostatic mirror and then also guided towards the detector. Therefore a detection in 4π solid angle is realised.

The momenta of the protons coming from the decay volume are aligned by the *inverse magnetic mirror effect* (see sect. 3.1 for further description). Afterwards the protons are energy selected by a potential barrier in the *analysing plane* and focused by a strong magnetic field onto the detector. In order to obtain a detectable signal the protons have to be post-accelerated. Therefore the detector is operated on a high voltage of $\sim 15\,\mathrm{kV}$.

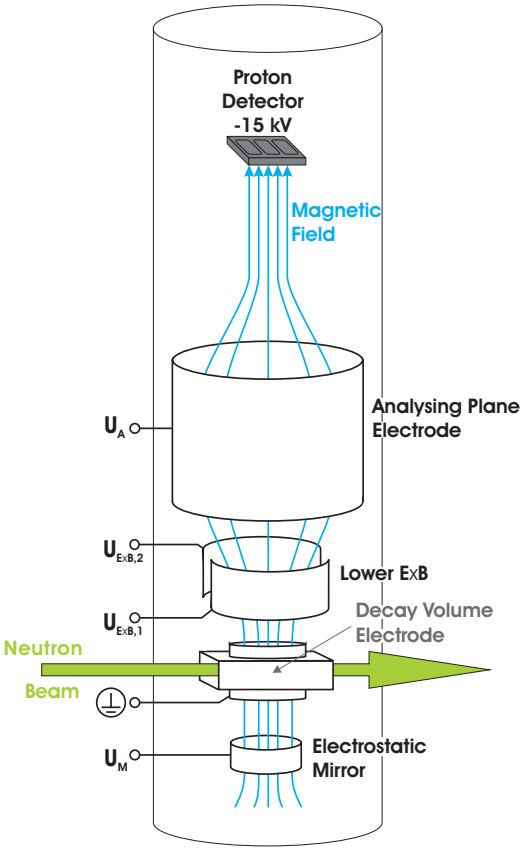

Figure 3.1: A scheme of the *a*SPECT spectrometer. Protons coming from the decay volume are guided by the magnetic field either directly to the detector or in the opposite direction, where they are reflected by an electrostatic mirror potential. The protons are energy selected by the big cylindrical analysing plane electrode.

3.1 The concept of adiabatic invariance and the magnetic mirror effect

In *a*SPECT the protons are guided along a magnetic field and shall be energy selected by a potential barrier which is only sensitive to the longitudinal energy component of the proton. Thus, practically all of the proton's

momentum should be transferred to the parallel component without changing the kinetic energy of the proton. The inverse magnetic mirror is a suitable tool to do this.

The concept of adiabatic invariance can be derived from classical mechanics. With p_i and q_i being the generalised canonical momenta and coordinates one can define the action integral for every periodic coordinate:

$$J_i = \oint p_i dq_i. \tag{3.1}$$

These integrals are constant for a mechanical system with given initial conditions. If now the system changes in some way, it is possible, but not required that the action integrals change. In fact it can be proved[1] that the action integrals stay invariant if the change of the system is slow compared to the relevant period of the motion and if the change is not related to the period. If these conditions are fulfilled, one speaks of an *adiabatic change* of the system. In practice, this means that we can change the properties of our system towards a different motion without changing the values of the action integral if only the change is slow enough.

Protons in a static magnetic field are forced on helical tracks by the Lorentz force:

$$\vec{F}_{\mathrm{L}} = q\left(\vec{v} \times \vec{B}\right), \tag{3.2}$$

where $\vec{B}$ is the strength of the magnetic field, $\vec{v}$ the velocity, and q the charge of the proton. The velocity can be decomposed in a circular and a longitudinal component. The circular component now forms a periodic property of the motion and one can show that

$$\left.\begin{array}{r} Br^2 \\ p_\perp^2/B \\ \gamma\mu \end{array}\right\} \text{ are adiabatic invariants.} \tag{3.3}$$

r is the radius of the proton orbit, $p_\perp$ the transverse momentum, and μ is the magnetic moment of the current loop of the proton. $\gamma = 1/\sqrt{1 - v^2/c^2}$ is the usual relativistic factor. Because of the low energies of the protons

[1] See [26] and the references given therein.

from neutron decay we can set $\gamma = 1$. For the full calculation the reader is referred to textbooks [26].

Next we consider a cylindrically symmetric, static magnetic field with a small gradient (field increase) along positive z-direction. A proton spirals about the z-axis with a velocity component $\vec{v}_{\perp 0}$ transverse and a component $v_{\parallel 0}$ parallel to the magnetic Field $\vec{B}$ at $z = 0$. From eq. (3.3) we can deduce that, if only a static magnetic field is present, the speed and the energy of the proton are constant. Therefore for any position along the z-axis the following equation is valid:

$$v_\parallel^2 + v_\perp^2 = v_0^2. \tag{3.4}$$

Since $p_\perp^2/B$ is an adiabatic invariant we may write

$$\frac{v_\perp^2}{B} = \frac{v_{\perp 0}^2}{B_0}. \tag{3.5}$$

Then the parallel velocity at any position of the z-axis is given by

$$v_\parallel^2 = v_0^2 - v_{\perp 0}^2 \cdot \frac{B(z)}{B_0}. \tag{3.6}$$

If the magnetic field increases, the second term in the last equation increases as well and the velocity of the proton parallel to the z-axis $v_\parallel$ becomes smaller. This means that the gyration length of the particle is getting smaller and smaller, until at some point along the z-axis the right hand side of this equation vanishes and the particle is reflected while still spiralling in the same sense with respect to the magnetic field.

This principle can be used to trap charged particles (e.g., a plasma) magnetically in a setup with a strong magnetic field at both ends and a weak field in the middle.

The other way round, if a particle is moving from a strong to a weak field the parallel velocity component is enlarged. This so called *inverse magnetic mirror effect* is used in our experiment. A sketch of the normal and the inverse magnetic mirror can be seen in fig. 3.2.

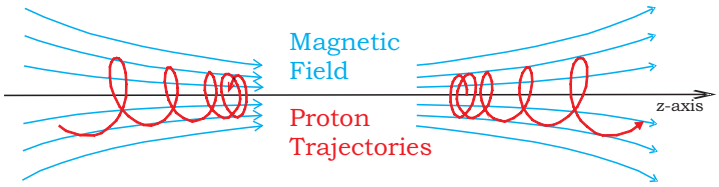

Figure 3.2: Field lines and proton trajectories in the normal (left) and the inverse (right) magnetic mirror effect.

3.2 Transmission function

As the velocity of a proton was decomposed in a longitudinal and a transverse component in the previous section, we now decompose the energy:

$$T_\perp(z) = T(z)\sin^2\theta(z), \tag{3.7}$$

$$T_\parallel(z) = T(z)\cos^2\theta(z), \tag{3.8}$$

where θ is the angle between the momentum of the proton and the z-axis. Although $T(z)$ is no longer conserved if also an electric field is present, in the adiabatic approximation the orbital momentum μ is still invariant

$$\mu = \frac{p_\perp^2(z)}{2m_\mathrm{p}B(z)} = \frac{T_\perp(z)}{B(z)} = \frac{T(z)\sin^2\theta(z)}{B(z)} = \text{const.} \tag{3.9}$$

Thus, the value of the orbital moment of the proton at any point P of its trajectory is equal to its magnetic moment in the decay volume in the instant of the decay:

$$\mu|_{\text{decay volume}} = \frac{T(0)\sin^2\theta(0)}{B(0)} = \mu|_\mathrm{P} = \frac{T(P)\sin^2\theta(P)}{B(P)}. \tag{3.10}$$

Since the points of interest are only the point of the decay and the analysing plane, we will denote the values at these places with indices 0 and A, respectively (e.g., B_0, T_A). Furthermore the "(z)" for values without index will not be written any more. Then we can deduce a relation for $\sin\theta$ from

eq. (3.10):

$$\sin^2\theta = \frac{B}{B_0}\frac{T_0}{T}\sin^2\theta_0. \tag{3.11}$$

Due to the inverse magnetic mirror most of the proton's transversal momentum is transferred into longitudinal momentum on its way from the decay volume to the analysing plane. Since the total energy is constant in the adiabatic approximation, also the proton's transversal kinetic energy is transferred into longitudinal energy. With $\cos^2\theta = 1 - \sin^2\theta$ and eq. (3.11) we can write for the longitudinal kinetic energy in the adiabatic approximation $T_\parallel^{\mathrm{ad}}$:

$$T_\parallel^{\mathrm{ad}} = T\left(1 - \sin^2\theta\right) = T - \frac{B}{B_0}T_0\sin^2\theta_0. \tag{3.12}$$

The total energy E of the proton inside the magnetic and electric field is conserved:

$$E = T + V = T + e(U - U_0), \tag{3.13}$$

where V is the potential energy of the proton and U the electrostatic potential at a point along the z-axis. In the decay volume the potential energy is $V_0 = 0$, hence we can substitute $E = T_0$ and deduce for the kinetic energy at any point

$$T = T_0 - e(U - U_0). \tag{3.14}$$

Thus, eq. (3.12) can be rewritten as

$$T_\parallel^{\mathrm{ad}} = T_0 - e(U - U_0) - \frac{B}{B_0}T_0\sin^2\theta_0. \tag{3.15}$$

A proton reaches the detector if $T_\parallel^{\mathrm{ad}} > 0$ for every point along its trajectory. If at some point $T_\parallel^{\mathrm{ad}} \leq 0$ is valid, the proton will be reflected. Therefore a precise knowledge of the fields is vital, to be sure that the minimum of the parallel energy is equal to the potential energy of the analysing plane.

The minimal initial kinetic energy needed for a proton to overcome the

potential barrier in the analysing plane is given by

$$T_{\mathrm{tr}} = \frac{e(U_{\mathrm{A}} - U_0)}{1 - \frac{B_{\mathrm{A}}}{B_0}\sin^2\theta_0}. \tag{3.16}$$

This is a function of the initial angle between the momentum of the proton and the z-axis. Therefore we can distinguish three parts of the transmission function. For $\sin\theta_0 = 0$ the minimum transmission energy is given by

$$T_{\mathrm{tr}}^{\mathrm{min}} = e(U - U_0). \tag{3.17}$$

All protons with energies equal to or smaller than $T_{\mathrm{tr}}^{\mathrm{min}}$ are reflected by the potential barrier. On the other hand, for $\sin\theta_0 = \pm 1$ we get the transmission energy above which all protons with energies higher than $T_{\mathrm{tr}}^{\mathrm{max}}$ are transmitted,

$$T_{\mathrm{tr}}^{\mathrm{max}} = \frac{T_{\mathrm{tr}}^{\mathrm{min}}}{1 - \frac{B_{\mathrm{A}}}{B_0}}. \tag{3.18}$$

The third case for proton energies between $T_{\mathrm{tr}}^{\mathrm{min}} < T_0 < T_{\mathrm{tr}}^{\mathrm{max}}$ is more complicated. In this region, the transmission function is a function of the initial angle θ_0. To obtain the function we have to compare the rate of transmitted protons $\rho_{\mathrm{tr}}(T_0)$ with the rate of protons emitted in the total solid angle $\rho_{\mathrm{total}}(T_0)$ for a given initial energy T_0:

$$\rho_{\mathrm{tr}}(T_0) = \int_0^{2\pi} d\phi \int_0^{\theta_0^{\mathrm{max}}} \sin\theta_0 d\theta_0 W(T_0), \tag{3.19}$$

and

$$\rho_{\mathrm{total}}(T_0) = \int_0^{2\pi} d\phi \int_0^{\pi/2} \sin\theta_0 d\theta_0 W(T_0), \tag{3.20}$$

where θ_0^{max} is the maximum angle at which protons are still transmitted through the analysing plane. $w(T_0)$ is the proton recoil spectrum which has no angular dependence for an unpolarised neutron beam and thus can be

taken out of the integral. Then the integration is trivial and results in

$$\rho_{\mathrm{tr}}(T_0) = 2\pi W(T_0)\,(1-\cos\theta_0^{\max})\,, \tag{3.21}$$

$$\rho_{\mathrm{total}}(T_0) = 2\pi W(T_0), \tag{3.22}$$

and

$$F_{\mathrm{tr}}(T_0)|_{T_{\mathrm{tr}}^{\min}<T_0<T_{\mathrm{tr}}^{\max}} = \frac{\rho_{\mathrm{tr}}(T_0)}{\rho_{\mathrm{total}}}(T_0) = 1-\cos\theta_0^{\max}, \tag{3.23}$$

where $F_{\mathrm{tr}}(T_0)|_{T_{\mathrm{tr}}^{\min}<T_0<T_{\mathrm{tr}}^{\max}}$ is the transmission function for proton energies between $T_{\mathrm{tr}}^{\min}$ and $T_{\mathrm{tr}}^{\max}$. For the angle $\theta_0^{\max}$ we obtain from eq. (3.16)

$$T_0 = \frac{e(U_{\mathrm{A}}-U_0)}{1-\frac{B_{\mathrm{A}}}{B_0}\sin^2\theta_0^{\max}}. \tag{3.24}$$

After replacing $\sin^2\theta_0^{\max}$ by $1-\cos^2\theta_0^{\max}$ and a trivial transformation we get

$$F_{\mathrm{tr}}(T_0)|_{T_{\mathrm{tr}}^{\min}<T_0<T_{\mathrm{tr}}^{\max}} = 1-\cos\theta_0^{\max} = 1-\sqrt{1-\frac{B_0}{B_{\mathrm{A}}}\left(1-\frac{T_{\mathrm{tr}}^{\min}}{T_0}\right)}. \tag{3.25}$$

Finally the full transmission function is given by

$$F_{\mathrm{tr}}(T_0) = \begin{cases} 0 & \text{if } T_0 \le T_{\mathrm{tr}}^{\min} \\ 1-\sqrt{1-\frac{B_0}{B_{\mathrm{A}}}\left(1-\frac{T_{\mathrm{tr}}^{\min}}{T_0}\right)} & \text{if } T_{\mathrm{tr}}^{\min} < T_0 < T_{\mathrm{tr}}^{\max} \\ 1 & \text{if } T_0 \ge T_{\mathrm{tr}}^{\max} \end{cases} \tag{3.26}$$

The shape of the transmission function is shown in fig. 3.3.

3.3 The retardation spectrometer

In reality the design of the electric and magnetic fields inside the spectrometer is much more complex than shown in fig. 3.1. A detailed sketch of the electrodes can be seen in fig. 3.4.

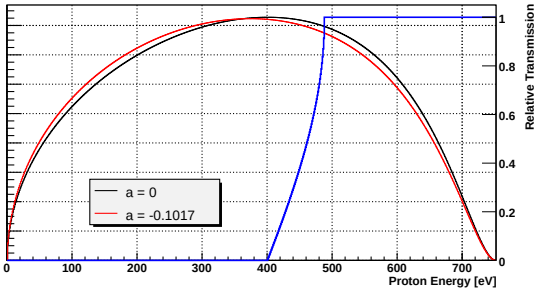

Figure 3.3: The theoretical proton spectrum for two values of a (black and red) and the transmission function for $U_A - U_0 = 400\,\mathrm{V}$ (blue).

3.3.1 Design of the electric fields

The neutron beam passes through a region with high magnetic field ($\sim 3\,\mathrm{T}$ at maximum coil current and about $2.2\,\mathrm{T}$ during the beamtime). This region (called the *decay volume*) is held at $0\,\mathrm{V}$ by the electrodes e3 - e6. The decay volume consists of three parts. Neutrons pass through a rectangular tunnel with an opening on side for vacuum pumping. Protons from neutrons decaying in this region are guided towards the detector through two more cylindrical openings on top and bottom of the electrode. Two separate longer cylinders follow on both sides with a small gap. They are kept a ground potential as well to ensure a homogeneous field in the decay region. The protons are either directly guided to the detector towards the top or they are reflected by the electrostatic potential created by the mirror electrodes (e1 and e2) on the bottom. Since the electric field is conservative, one can reflect the protons like this without changing their initial kinetic energy (changing the kinetic energy would change the shape of the proton recoil spectrum as well). To avoid a too low electrical field in the centre of the mirror electrode a grid of copper wires is installed on the lower end of electrode e1. e2 is a quadrupole electrode, 4 quarter cylinders are separated by small slits, every part can be powered individually. In normal measurement runs all four parts have the same potential, the quadrupole function is needed for tests with an ion source which can be mounted below the spectrometer. By applying different potentials to the parts, the beam from the ion source can be shifted.

The analysing plane is situated in the middle of the big cylindrically

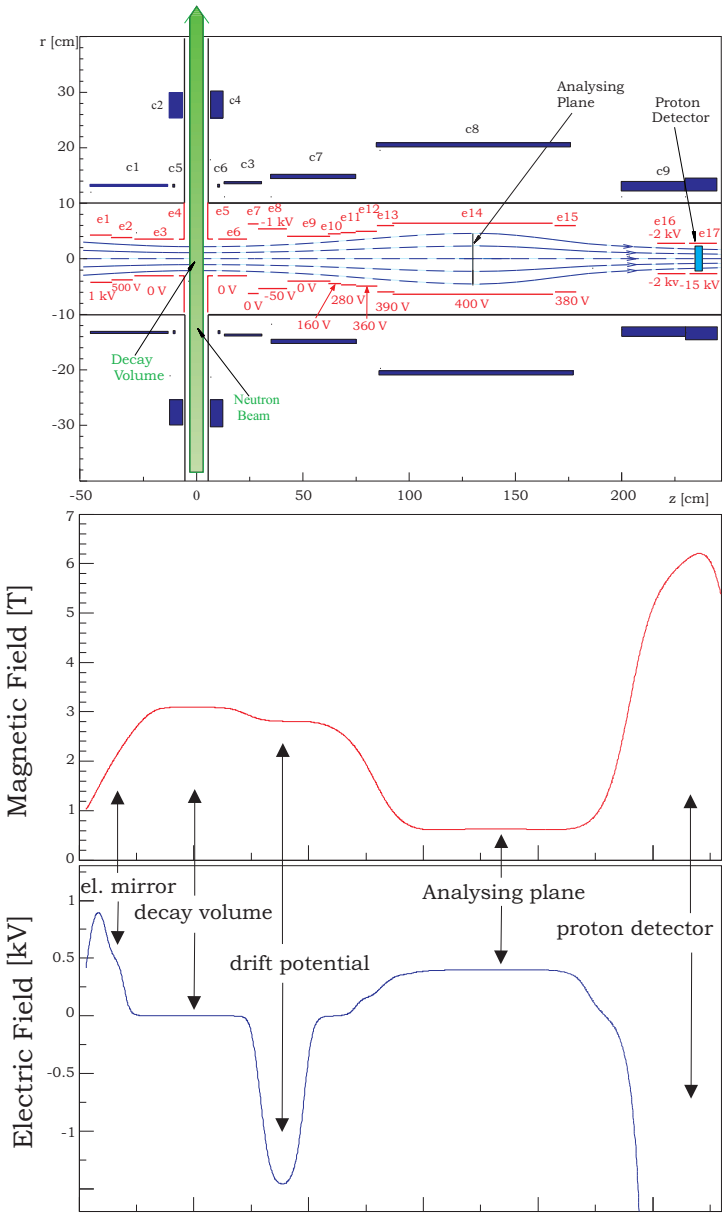

Figure 3.4: Top: A detailed sketch of the coils and electrodes inside *a*SPECT, denoted c1 to c9 and e1 to e17, respectively. The sketch is turned by 90° for better comparability to the lower pictures. Magnetic field (middle) and electrostatic potential (bottom) along the z-axis of the spectrometer. These pictures are taken from [27] and are simulated for the settings given therein.

symmetric electrode e14. Protons with enough energy to overcome the potential barrier are focussed on the detector by the high magnetic field and post-accelerated by the high electric potential created by electrode e17 which is surrounding the detector[2]. The electrodes e10-e13 and e15 are set to similar potentials as electrode e14 to avoid a lower field reaching into the analysing plane and to ensure an adiabatic movement of the protons. Electrodes e10 to e15 are all powered by the same power supply, e14 is connected directly, the others via resistor based voltage dividers.

Two pairs of $\vec{E} \times \vec{B}$ electrodes are installed in the spectrometer. Each electrode pair provides an electric field perpendicular to the magnetic field. As soon as a charged particle moving in the magnetic field enters the perpendicular electric field the particle keeps spiralling about the magnetic field lines, but this movement is accompanied by a uniform drift with velocity $\vec{u}$:

$$\vec{u} \propto \frac{\vec{E} \times \vec{B}}{B^2}. \tag{3.27}$$

This means the particle drifts perpendicular to both electric and magnetic field. The direction of the drift only depends on the directions and strengths of the $\vec{E}$ and the $\vec{B}$ field, but not on the initial direction of the through-going particle. Further details can be found in [26].

As can be seen from eq. (3.27), the displacement of a charged particle in an $\vec{E} \times \vec{B}$ field depends only on the time spent in the field. Electrons from neutron decay have much higher velocities than the protons, thus they spend less time in the $\vec{E} \times \vec{B}$ field and are displaced less than the protons.

The lower pair of $\vec{E} \times \vec{B}$ electrodes is situated between the decay volume and the analysing plane (e8 in fig. 3.4). Protons that cannot overcome the analysing plane are trapped and oscillate between the electrostatic mirror on the bottom of the spectrometer and the analysing plane. Every time a trapped proton passes the $\vec{E} \times \vec{B}$ it is displaced a few millimetres and finally it is absorbed on the spectrometer wall after a few oscillations. According to eq. (3.27) the direction of drift is the same, regardless of the direction of flight of the proton.

Another pair of $\vec{E} \times \vec{B}$ electrodes is installed in front of the detector for two reasons: On the one hand it ensures that the acceleration voltage

[2] See sect. 4.3.2 for a detailed description of the detector mechanics.

reaches sufficiently deep into the cryostat that all protons overcome the magnetic mirror created by the increasing magnetic field. For this, a simple cylindrical electrode would be sufficient. On the other hand, with the pair of $\vec{E} \times \vec{B}$ electrodes, the protons can be shifted with respect to the detector.

The lower electrode pair shifts the particles longitudinal, the upper one perpendicular to the neutron beam. As the total decay volume is longer than the actually detected part, the lower $\vec{E} \times \vec{B}$ causes only a minor systematic effect, whereas the upper pair allows to choose the position of the detector with respect to the neutron beam. For normal operation the voltages on the upper $\vec{E} \times \vec{B}$ electrodes are chosen to map the centre of the neutron beam to the detector and thus minimise the edge effect (see sect. 3.4.6). For systematic studies of the edge effect the voltages may be chosen to investigate one side of the neutron beam.

The electrodes e1 to e15 are mounted on one rigid support structure. This system is often referred to as the electrode system. The upper $\vec{E} \times \vec{B}$ electrodes are fixed on the top flange of the spectrometer. The detector can be moved into the spectrometer with the moveable mechanics described in sect. 4.3.2. Electrodes e1 to e15 are made from oxygen and hydrogen free copper (OHFC) and coated with gold. This fulfils both the demands for ultra high vacuum and the needed electrical potential. As it will be explained in sect. 3.4.1, especially in decay volume and analysing plane the potentials have to be well defined and very homogeneous. Table 3.1 shows the typical voltages on the single electrodes during normal measurement runs.

3.3.2 Design of the magnetic field

The magnetic field is created by 9 superconducting coils (c1 to c9 in fig. 3.4). Except for coils c5 and c6, all coils are operated in a serial configuration, thus, even if there are minor fluctuations in the current through the coils, the ratio of the magnetic fields in the decay volume, the analysing plane, and at the detector stays constant. To minimise fluctuations of the magnetic field the magnet is operated in persistent mode. This means, after the current is introduced into the coils with an external power supply, the magnet is shorted with an internal superconducting switch. Thus the magnet is

Electrode	Voltage	Comments
e1	800 V	Electrostatic mirror (grid on bottom side)
e2	1000 / 820 V	Electrostatic mirror (quadrupole electrode)
e3 to e6	grounded	Decay volume electrodes (parts wired individually)
e7	Grounded	Usable for systematic checks
e8	-1000 / -50 or -200 / 0 V	Lower $E \times B$ drift electrodes
e10	$0.4 \times U_{\mathrm{A}}$	Variable
e11	$0.7125 \times U_{\mathrm{A}}$	Variable
e12	$0.9 \times U_{\mathrm{A}}$	Variable
e13	$0.9925 \times U_{\mathrm{A}}$	Variable
e14	U_{A}	Analysing plane electrode (variable)
e15	$0.9875 \times U_{\mathrm{A}}$	Variable
e16	-2 / -2 or -3.7 / -4.2 kV	Upper $E \times B$ drift electrodes
e17	-10 to -15 kV	Detector HV

Table 3.1: Typical settings of the electrodes.

decoupled from possible fluctuations of the power supply. The magnetic field decreases very slowly when the magnet is in persistent mode. However this minor decrease does not affect the measurement, as the magnetic field ratio r_{B} stays constant.

The correction coils c5 and c6 allow to adjust the shape of the magnetic field in the decay volume. A maximum of the magnetic field in the middle of the decay volume might lead to a trapping of particles with very low longitudinal momentum between the electrostatic mirror and the decay volume due to the magnetic mirror effect. Therefore a small magnetic field gradient with the maximum below the lower end of the decay volume is generated. This ensures that the decay particles can leave towards the detector.

The spectrometer magnet consists of two separated, nested vacuum chambers and was manufactured by Cryogenic Inc. The outer chamber houses the superconducting coils which are made from niobium-titanium and mounted on a common support structure. To make them superconducting they have to be cooled below their superconducting edge temperature of $T_c \approx 9\,\mathrm{K}$. They are cooled by two cryocoolers[3], the outer vacuum chamber is needed to isolate them against the room temperature outside the spectrometer. The outer chamber is sealed with rubber rings and pumped to below $10^{-3}\,\mathrm{mbar}$ before the cooldown is started. During the cooldown the vacuum improves further. For the decay particles a much better vacuum is needed, thus the inner chamber (called the main vacuum) is separated from the outer one and sealed with CF copper gaskets. The demand of ultra high vacuum limits the choice of used materials, details on the needed vacuum conditions are given in sect. 3.4.3.

Two pairs of external correction coils[4] allow to adjust the magnetic field in the analysing plane. One pair is operated in Helmholtz configuration to alter the ratio of the magnetic fields in analysing plane and decay volume r_B and thus the transmission function (see sect. 3.2). This pair is used only for systematic investigations of the spectrometer. The other pair is operated in anti-Helmholtz configuration (i.e. the current in one coil is going in the opposite direction than in the other one), this setup creates a field gradient in z-direction. The magnetic field has a local maximum in the analysing plane. Close to the analysing plane, the electrostatic potential is nearly uniform, $U \sim U_A$. A magnetic field minimum in this region would have to be extremely uniform to fulfil the transmission condition. With a small local maximum the transmission function is automatically fulfilled [27]: The transmission condition $T_{\parallel}^{\mathrm{ad}} > 0$ for eq. (3.15) and eq. (3.16) require

$$\frac{B_0 - B\sin^2(\theta_0)}{B_0 - B_A\sin^2(\theta_0)} > \frac{U - U_0}{U_A - U_0}. \tag{3.28}$$

U is maximal exactly in the analysing plane, thus $U_A > U$ holds everywhere in the region around the analysing plane and the right hand side of the equation is always < 1. For $B < B_0$ the left hand side of the equation is

[3] Sumitomo RDK408D.
[4] Not indicated in fig. 3.4.

always > 1 and the transmission condition is automatically fulfilled.

To create a working analysing plane, the local maximum of the magnetic field has to be on the same height as the maximum of the electric potential. To achieve this the anti-Helmholtz coils were operated with a current of 27.5 A.

To minimise stray magnetic field, the spectrometer is surrounded by an iron screen consisting of a top and a bottom plate ($1.8 \times 1.8\,\mathrm{m}^2$ each) which are connected by four iron pillars with a cross section of $20 \times 20\,\mathrm{cm}^2$ each. To access the flanges on top and on the bottom of the spectrometer the plates have holes with a diameter of 50 cm in the centre. This setup offers good magnetic screening on the outside but has only minor influence on the magnetic field inside the main bore tube.

Details about simulations and design of the magnetic and electrical fields as well as the anti-magnetic screen can be found in [28].

3.4 Systematic effects

In any measurement a good knowledge of systematic effects of the experimental apparatus is vital. In our case several different possible sources of systematic effects have been considered. In the following section I will present the results of these considerations. I am basically following the presentation of these results of F. Glück *et al.* given in ref. [27].

The final goal of *a*SPECT is to measure a with a precision of $\frac{\Delta a}{a} \approx 3{\cdot}10^{-3}$. Thus the limit for the influence of each systematic effect was chosen to be $\frac{\Delta a}{a} < 10^{-3}$.

3.4.1 Adiabatic transmission function

For a precise calculation of a the parameters of the transmission function eq. (3.26) have to be know very precisely. The magnetic field in the decay volume, B_0, and in the analysing plane, B_A, has to be known with a relative uncertainty of 10^{-4}. A crucial point is the stability of the magnetic field. To measure the field a special dewar made from non-magnetic materials is inserted in the main bore tube of the magnet instead of the electrode

system. Dewar and electrode system can only be exchanged when the cryostat is warm, thus the field cannot be measured during a data taking run. Therefore, we need a good stability of the field. Additionally, to avoid a detailed measurement of the neutron density distribution inside the decay volume, the inhomogeneity in this region should be less than 10^{-4}. For further beamtimes a monitoring system is in preparation which will allow to monitor the magnetic fields in the analysing plane and the decay volume while the electrode system is installed. This system will be based on nuclear magnetic resonance of either polarised ^{3}He or hydrogen. Sample cells will be placed close to the decay volume and the analysing plane, but outside the actual electrodes, from the ratio of the measured NMR frequencies the ratio of the magnetic fields can be inferred [29].

For the electric potentials similar problems arise. The potential in the decay volume U_0 has to be less than 1 mV, the variations of the potential in the analysing plane U_A less than 2 mV. To achieve this accuracy the main source of deviation, field penetration into the cylindrical electrode e14, has to be minimised. This is done by the length (54 cm) of electrode e14 and by setting the neighbouring electrodes to similar potentials (see fig. 3.4). The absolute voltage difference of electrode e14 to the decay volume has to be known with an accuracy of 10 mV.

The accumulation of negative space charges around the analysing plane could change the potential of the analysing plane, as well as surface charges on a possible insulating surface layer of the electrodes. To reduce these effects, the electrodes are coated with 1 μm of gold on a layer of 2 μm of silver for adhesive reasons. They are all kept at the same temperature of about 70 K, the temperature of the bore tube. This cancels the differences in the work functions of the different materials. In a cylindrical sample electrode which was gold-coated in the same way as the electrodes in the spectrometer as they were used in a previous beamtime, variations of the work function of up to 200 meV were found in a measurement with a Kelvin probe at room temperature. After this result the most important electrodes were coated with a 2 μm layer of gold on 5 μm of silver and electro-polished to improve the homogeneity of the work functions.

To reach the final precision in a, the surfaces of the electrodes have to be further improved. Furthermore, a monoenergetic ion source is under construction by our collaboration partners in Mainz to investigate the effects

further and to measure the difference of the potentials U_A and U_0 *in situ*.

3.4.2 Non-adiabatic proton motion

In the adiabatic approximation the transmission function eq. (3.26) can be calculated analytically and the trajectory's magnetic moment μ is considered to be constant. Deviations of μ from its initial value could destroy the adiabacity and thus change the transmission function.

Calculations show that the value of μ in the analysing plane is indeed close to its initial value. On the other hand, between the decay volume and the analysing plane there are regions with high electric and magnetic field gradients where the value of μ oscillates with a period equal to the local gyration period. The amplitude of these oscillations increases with the gradient of the fields. Fortunately, we can define an adiabatic invariant $\hat{\mu} = \mu + \delta\mu$ which varies much less than μ. The term $\delta\mu$ is a complicated expression, proportional to first and higher order derivatives of magnetic field and electrostatic potential[5]. If the field is homogeneous, the derivatives are small and $\hat{\mu} \approx \mu$. Protons inside *a*SPECT start their life in a highly homogeneous region (the decay volume) and move through an inhomogeneous region to another homogeneous one (the analysing plane). $\hat{\mu}$ is nearly constant in any region, whereas, in the inhomogeneous region μ (and thus, to keep $\hat{\mu}$ constant, also $\delta\mu$) shows large oscillations. But, as soon as the proton enters the analysing plane region, the oscillations of $\delta\mu$ disappear and $\hat{\mu} \approx \mu$ is valid again. The protons seem to have some kind of "memory" [27] of their initial orbital momentum when they pass from one region to another.

The problem of a non-adiabatic proton motion is more severe for protons trapped between the analysing plane and the electrostatic mirror e1. These protons perform several oscillations between the two potential barriers until they are finally removed by the lower $\vec{E} \times \vec{B}$ electrode e8. Therefore they have a higher probability to change their trajectory non-adiabatically and to pass the analysing plane. In principle a higher voltage $|U_8|$ at electrode e8 would be useful because it removes the trapped protons faster, but protons are accelerated by the negative potential of the electrode and thus their

[5] A full description of $\delta\mu$ can be found in textbooks on plasma physics, for example in [30].

gyration length becomes larger. This causes a deviation from the adiabatic approximation. Calculations show that the adiabatic condition breaks down for $|U_8| > 3\,\mathrm{kV}$.

The non-adiabacity effect increases exponentially with decreasing magnetic field. The calculated effects on a for different values of the magnetic field and $U_8 = -3\,\mathrm{kV}$ are shown in Table 3.2. For values above 1.5 T in the decay volume the effect on a is negligible. During the beam time usually a drift potential of 1 kV was used.

B_0	3 T	1.5 T	1.2 T	0.9 T	0.6 T
δa	10^{-6}	$4 \cdot 10^{-5}$	$5 \cdot 10^{-4}$	$4 \cdot 10^{-3}$	$2 \cdot 10^{-2}$

Table 3.2: Systematic effect on a due to non-adiabatic proton motion for different values of the magnetic field in the decay volume for a voltage in the lower $\vec{E} \times \vec{B}$ electrode $U_8 = 3\,\mathrm{kV}$.

3.4.3 Residual gas

Protons should be counted by the detector if and only if they have kept their initial energy T_0 and have moved adiabatically until they arrive at the analysing plane. On their way from the decay volume to the detector they may interact with residual gas molecules - and thus change their energy or direction - in three different ways:

- Elastic scattering
- Inelastic energy loss
- Charge exchange

The systematic effect due to these interactions is proportional to the residual gas density and therefore, since the temperature in the main bore tube of aSPECT is constant ($\approx 70\,\mathrm{K}$), the effects are proportional to the pressure of the gas. Thus we can define a critical pressure p_{cr} at which a considered type of collision introduces a systematic effect on a on a level of $\frac{\Delta a}{a} = 10^{-3}$.

Elastic scattering and inelastic energy loss

In elastic scattering processes energy and pitch angle (the angle between the magnetic field line and the direction of the proton) is changed. A proton with sufficient initial energy $T_0 > T_{\mathrm{tr}}$ to be transmitted through the analysing plane could loose energy in a scattering process and thus be hindered to be counted, whereas a proton with $T_{\mathrm{tr}}^{\mathrm{min}} < T_0 < T_{\mathrm{tr}}$ could be transmitted if it changes it angle to the magnetic field.

The second effect is more important, since these protons are trapped between the potential barriers of the analysing plane electrode and the electrostatic mirror they perform several axial oscillations and their path length in the spectrometer is much longer. The scattering probability is proportional to the path length. The lower $\vec{E} \times \vec{B}$ electrode e8 removes the trapped protons after several oscillations. The higher the potential U_8, the faster the trapped protons are removed. The critical pressure for different settings of the lower $\vec{E} \times \vec{B}$ electrode has been calculated [27] for different values of U_8. The results can be seen in table 3.3. As expected, the critical pressure is decreasing for lower voltages U_8, due to the rise in trapping time.

U_8 [kV]	-3	-0.3	-0.03
p_{cr} [mbar]	$5 \cdot 10^{-8}$	10^{-8}	$1.4 \cdot 10^{-9}$

Table 3.3: Critical pressure values of elastic p-H_2 scattering for different settings of the lower $\vec{E} \times \vec{B}$ electrode.

Furthermore, protons may loose energy by inelastic scattering processes on hydrogen molecules, like for example rotational and vibrational excitations. The critical pressure for the dominating excitation of vibrations in p-H_2 has been calculated to $p_{\mathrm{cr}} = 4 \cdot 10^{-8}$ mbar.

Charge exchange

Additionally to the scattering processes, protons can be lost if they capture an electron from a residual gas molecule, resulting in a hydrogen atom and a positive ion: $\mathrm{p} + \mathrm{M} \rightarrow \mathrm{H} + \mathrm{M}^+$. Usually the ion will have very little energy and, if the process happens below the analysing plane, no event will

be detected. The critical pressures for different gasses have been calculated using published cross-sections, the results can be seen in table 3.4.

Gas	H_2	Ar	N_2	O_2	He
p_{cr} [mbar]	$2 \cdot 10^{-8}$	10^{-8}	$2 \cdot 10^{-8}$	$4 \cdot 10^{-8}$	10^{-6}

Table 3.4: Critical pressure values of the charge exchange process for different residual gasses.

According to these considerations our vacuum should be better than 10^{-8} mbar. This vacuum can be easily reached because the cold bore tube acts like a cryogenic pump. In the beamtime a vacuum of about $8 \cdot 10^{-9}$ mbar was measured on a 2 m long, warm CF 40 vacuum tube attached to the bottom flange of the spectrometer. This long tube is needed, as the vacuum is measured by a cold cathode gauge[6] which uses a strong permanent magnet. This permanent magnet has to be sufficiently far away from the main magnet. Inside the cold main bore tube the vacuum should be a lot better.

3.4.4 Background

Regarding the background one has to distinguish between correlated and uncorrelated background. When a neutron decays in the decay volume of *a*SPECT a proton and an electron are produced simultaneously. A fraction of the electrons will reach the detector causing a background signal correlated with a proton event. Since electron and proton are produced at the same time, they are detected in near coincidence. Electrons that can reach the detector move with velocities close to the speed of light due to their high energy and thus reach the detector after very short flight times. Electrons emitted directly towards the detector have flight times of about 10 ns. The proton needs at least $\sim 6\,\mu$s to reach the detector. With a too long dead time the proton would be concealed by the electron and only one event with the pulse-height of an electron is detected. As the time of flight of the protons depends on their energy, the loss of correlated protons would have a strong influence on a. For high analysing plane voltages the time of flight of the protons is longer as they travel with reduced velocity

[6] Pfeiffer IKR.

through the long analysing plane electrode. The dead time of the electronics is 5.2 μs, thus no correlated protons should be lost. Unfortunately, in the last beamtime correlated protons were concealed by a saturation effect described in sect. 6.5.

On the other hand, uncorrelated events can occur due to γ-radiation and cosmic rays, positive ions coming from residual gas or the electrodes, and high energy electrons created by neutron capture. This type of background can again be separated in beam-related and environmental (not beam-related) background. Although beam-related background is often a problem in neutron decay experiments, it does not have to be treated separately in our analysis as long as it does not depend on the setting of the analysing plane. With the retardation principle it is possible to measure the background separately and subtract it from the signal. Since the proton spectrum ends at $T_{\mathrm{max}} \sim 750\,\mathrm{eV}$ applying a voltage of $U_{\mathrm{A}} \sim 800\,\mathrm{V}$ at the analysing plane electrode e14 blocks all the decay protons from reaching the detector. Additional studies have to be performed to make sure that this does not change the background. For example, this can be done by applying 1 kV in electrode e14 to make sure that really all the protons are blocked, or by applying the barrier voltage at another position, like for example setting both parts of the lower $\vec{E} \times \vec{B}$ electrode e8 to +1 kV.

In the first beamtime with the *a*SPECT spectrometer at the research reactor FRM-II in Munich a background component depending on the analysing plane voltage was discovered and prevented the extraction of a value for a [31, 32]. As possible sources field emissions by high voltage electrodes, penning discharges, and trapped particles were identified. Several steps have been taken before the beamtime at the ILL to improve the background conditions. Several electrodes were redesigned and their surface conditions were improved by electro-polishing. The vacuum was improved by the installation of getter pumps[7] inside the main bore tube. Furthermore, the new detector allowed us to reduce the acceleration voltage from 30 to 15 kV.

The spectrometer offers several possibilities to study the different contributions to the background. A summary of the applied settings is given in table 3.5.

[7] SAES "CapaciTorr D400-2".

Type of background contribution	**Parameter settings**
Electronic/ thermal noise (detector and pre-amplifier)	Neutron beam: off Detector HV: on/ off Magnetic field: off
Beam related neutral background (gammas and fast neutrons)	Neutron beam: on/ off Detector HV: on Magnetic field: off
Beam related charged background (decay electrons)	Neutron beam: on/ off Detector HV: on Magnetic field: on AP voltage: +780 V
Environmental neutral background (e.g., cosmic rays)	Neutron beam: off Detector HV: off Magnetic field: off
Extra background depending on Analysing plane voltage	Neutron beam: on/ off Detector HV: on Magnetic field: on AP voltage: 0...+780 V Mirror voltage: on/ off Lower and upper $\vec{E} \times \vec{B}$: varying

Table 3.5: Parameter settings for different background studies. All background contributions except for the extra background can be subtracted by measurements without protons at 780 V analysing plane voltage.

3.4.5 Doppler effect due to neutron motion

The Doppler effect is a well known phenomenon in acoustics and optics. The frequency of a source moving with respect to the recipient is shifted depending on the direction of the movement.

In beta decay processes the movement of the decaying particle changes the observed energies of the outgoing particles in the laboratory system with respect to the energies in the centre-of-mass system (CMS) of the decaying particle. This effect may change the transmission function. In *a*SPECT the source of protons is a beam of cold neutrons with an average kinetic energy of about $T_\mathrm{n} = 5\,\mathrm{meV}$. A proton with an energy of $T_\mathrm{CMS} = 400\,\mathrm{eV}$ in the CMS and being emitted in the direction of the decaying neutron, has an energy in the laboratory system of $T_\mathrm{LAB} = T_\mathrm{CMS} + \delta T$, with $\delta T = 2\sqrt{T_\mathrm{n} T_\mathrm{CMS}} \approx 2.8\,\mathrm{eV}$. This is an enormous change compared to the needed accuracy of 10 meV. In a measurement with the magnetic field lines parallel to the direction of the neutron beam and without an electrostatic mirror a very precise measurement of the neutron velocity spectrum would be needed to be able to correct this systematic effect.

Therefore we use a geometry where the field is perpendicular to the neutron beam and ensure 4π detection of the protons. Since the decay protons are emitted equally in the full solid angle protons are emitted in a direction opposite to the movement of the neutrons as well. These protons have a lower laboratory energy than their CMS energy, thus a large cancellation of the Doppler effect is achieved. The effects on a were calculated for a typical neutron velocity distribution and different settings of the analysing plane voltage U_A. For $U_\mathrm{A} < 500\,\mathrm{V}$ the systematic effect is smaller than 10^{-4}, so we do not expect any essential systematic uncertainty from the Doppler effect.

3.4.6 Edge effect

The neutron beam passing through the spectrometer is wider than the detector, hence only a fraction of the produced protons actually hits the active area of the detector, the magnetic field projects the shape of the neutron beam onto the detector. As shown in fig. 3.5 the projection of the beam profile can be decomposed into three parts. In the central part, all produced protons hit the active area, in turn, any proton that is produced far

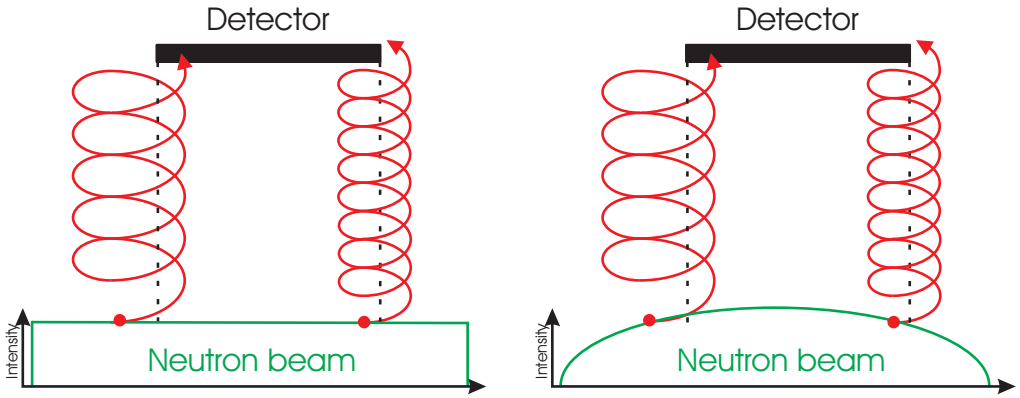

(a) In the ideal case of a perfectly flat beam profile the edge effect is negligible.

(b) For a inhomogeneous beam profile the value for a has to be corrected for the edge effect.

Figure 3.5: Illustration of the edge effect. Protons with different energies have different gyration radii.

outside the projected area will not hit the detector. Protons produced in between these two regions may hit the detector or not due to their gyration radii in the magnetic field.

In the ideal case of a perfectly flat beam profile over all three regions the edge effect would cancel as the probability that a proton from outside the direct projection area hits the detector is the same as the probability that a proton from inside misses the detector. For a inhomogeneous beam profile it becomes a significant systematic effect as the probabilities are no longer the same. The gyration radii of the proton and thus also the width of the intermediate region depend on the proton energy. This means also that the fraction of protons that may or may not hit the detector depends on the energy which causes a direct effect on a. This effect only concerns the direction transversal to the neutron beam. Along the neutron beam the profile can be considered flat.

There are two possible options to minimise this effect, one can either try to obtain a beam profile as flat as possible by optimising the neutron apertures. Or one has to ensure that any proton produced in the decay volume hits the detector. The setbacks of the second option are the difficulties in ensuring that all protons hit the detector, as protons missing the

detector can not be easily measured. Furthermore, a narrow beam reduces the amount of neutrons passing through the spectrometer strongly, thus the available statistics is reduced. For the last beamtime the first option with a wide beam was chosen.

This effect has been investigated both with numerical simulations and by measurements with different beam profiles during the beam time. Details of the neutron beam collimation are discussed in sect. 5.1.1.

3.4.7 Detection efficiency

Not all protons hitting the detector will actually be detected due to the dead layer and the response function of the detector. The probability that a proton is detected, the detection efficiency, depends on the energy and the impact angle. The average detection efficiency can be neglected, since it just reduces the count rate at the detector but cancels out for the overall measurement.

The impact energy of the protons is between the acceleration voltage of the detector and the acceleration voltage plus the endpoint energy of the proton spectrum $T_{\mathrm{Det}} \approx 15^{+0.75}_{-0}\,\mathrm{keV}$. Therefore, in first order, the energy-dependent detection efficiency can be written as $f_{\text{impact energy}} \propto (1 + c_1 \cdot T_0)$ with the initial energy of the proton T_0 and c_1 being a small number. With the usual level of tolerance $\delta a < 10^{-4}$ this results in the condition $|c_1| < 2 \cdot 10^{-4}\,\mathrm{keV}^{-1}$.

The impact angle and energy dependence of the detection efficiency can be calculated in detailed simulations of the detector properties, see sect. 4.5. With the results of these simulations the count rates can be corrected.

4 The detection system

4.1 A short introduction to semiconductors and semiconductor detectors

In the following a very brief introduction to the properties of semiconductors will be given, further information can be found in various textbooks [33, 34].

Semiconductors are solid materials with an electrical conductivity between the one of a conductor and an insulator. Silicon, the most commonly used semiconductor, has a conductivity at room temperature of $2.52 \cdot 10^{-6} \frac{1}{\Omega\text{cm}}$, compared to $5.0 \cdot 10^{-18} \frac{1}{\Omega\text{cm}}$ for the insulator sulfur and $6.0 \cdot 10^{5} \frac{1}{\Omega\text{cm}}$ for the conductor copper [33].

The reason for this intermediate conductivity is the small band gap between the valence and the conduction band of about 1 eV in semiconductors. In conductors the two bands overlap, in insulators they are separated by several eV. In semiconductors electrons can be excited from the valence to the conduction band by thermal vibrations at room temperature. For every electron that is moved into the conduction band a positive charge in the valence band, a so-called hole, is generated. Both electrons and holes can be treated as free particles if one introduces an effective mass for them. This mass is usually different from the elementary mass of an electron.

A pure semiconductor is called intrinsic, but the electrical behaviour of a semiconductor can be influenced by adding specific impurities to the crystal. If one adds an atom with one valence electron more or less than the semiconductor an additional free electron or hole is created, respectively. In the case of silicon, boron can be used to create holes or arsenic to create free electrons. Semiconductors with additional holes or electrons are called

p-doped or n-doped, respectively. Since semiconductor crystals are difficult to produce with sufficient purity, almost any semiconductor material available for technical use is faintly doped. Typically, slightly n-doped silicon is used as intrinsic material.

The energy to create electron hole pairs may come from thermal vibrations, but also from other processes like optical excitation or penetration of charged particles. The specific energy loss $-\frac{dE}{dx}$ of a charged particle travelling through material in x-direction is described by the Bethe-Bloch formula [35, 36]:

$$-\frac{dE}{dx} = \frac{4\pi e^4 z^2}{m_\mathrm{e} v^2} NZB, \tag{4.1}$$

where v is the velocity of the particle and ze its charge. N and Z are the number density and the atomic number of the penetrated material, m_e is the rest mass of the electron. B is a rather complicated expression depending on the particle's energy and the excitation and ionisation energy of the absorber.

The maximum energy that can be transferred from the incoming particle to an electron is, for kinematic reasons, $4E\frac{m_\mathrm{e}}{M}$, with E and M being the energy and mass of the incoming particle, respectively. For protons this is about 2 ‰ of their energy, so the proton will undergo many scattering processes on its way through the detector before it stops. This statistical process leads to a broadening of the initial energy distribution. This broadening is called straggling.

In a semiconductor only a fraction of the energy lost by the proton is converted to electron-hole-pairs, the rest creates phonons. The band gap of silicon is 1.12 eV, but to create one electron-hole-pair an average of 3.6 eV is needed.

Conventional silicon detectors usually are PIN diodes. Here, the the PN-structure of a normal diode is separated by an intrinsic layer to increase the active volume of the detector. The major setback of this detector type is that the capacitive noise of the detector is proportional to its active area. This means, to implement a larger detector surface one has either to live with large noise, or one has to divide the detector in many single active areas with a separate readout for each area. aSPECT uses a more

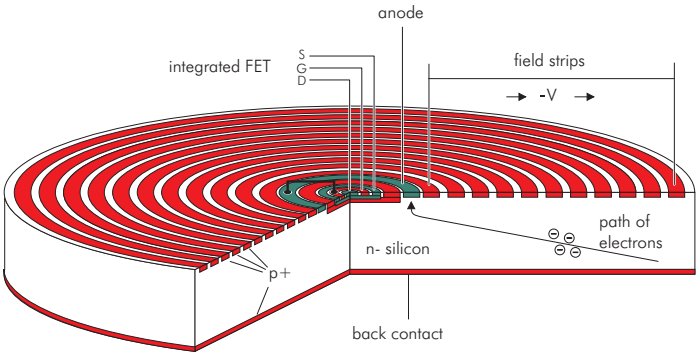

Figure 4.1: The principle of a silicon drift detector. Picture taken from [38].

elaborate semiconductor detector, a so-called silicon drift detector, where the thermal noise is decoupled from the active area.

4.2 The principle of a silicon drift detector

The principle of a silicon drift detector (SDD) was first described by Gatti and Rehak in 1984 [37]. Classical semiconductor detectors typically consist of a thin silicon wafer with a continuous n-doped layer on one side and p-doped strips on the other side. An electrical field in reverse bias mode is used both for depleting the detector and creating the field gradient to collect charges created by penetrating particles. In contrast, the SDD is based on the sidewards depletion principle. Here, instead of using one field for both depletion and charge separation, two separate fields are used.

As can be seen in fig. 4.1 the bulk material of the detector is n^- doped silicon. The superscript $-$ refers to a faint degree of doping, a $+$ indicates a strong doping. On one side of the SDD a smooth p^+ layer is implemented, whereas the other side has a structure of concentric p^+ rings.

The back contact is put to a positive voltage of about -150 V, the rings on the front side have different potentials, starting with about -15 V on the

innermost ring and rising to about -230 V on the outermost ring. The n^- doped regions between the rings have a rather high resistivity and thus act as voltage divider. Thus a potential valley (see fig. 4.2) is created inside the detector. Free electrons created inside the valley will drift towards the centre of the front side of the detector, where they are collected by a small n^+ doped anode.

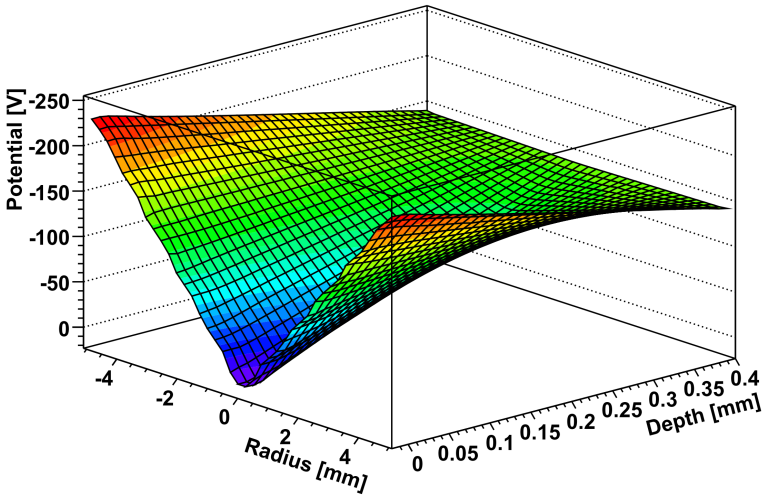

Figure 4.2: A simulation of the potential inside an SDD detector with typical values. Free electrons created within the potential valley drift towards the centre on the front side, where they are collected by the anode. For better visibility of the potential valley, the axis of the potential is plotted inverted.

4.3 The *a*SPECT detector

4.3.1 The detector chip

*a*SPECT uses three SDD detectors implemented in a row on one silicon chip. Each of those detector pads has an active area of 100 mm^2 in the form of a square with a side length of 10.3 mm and rounded edges with 2 mm

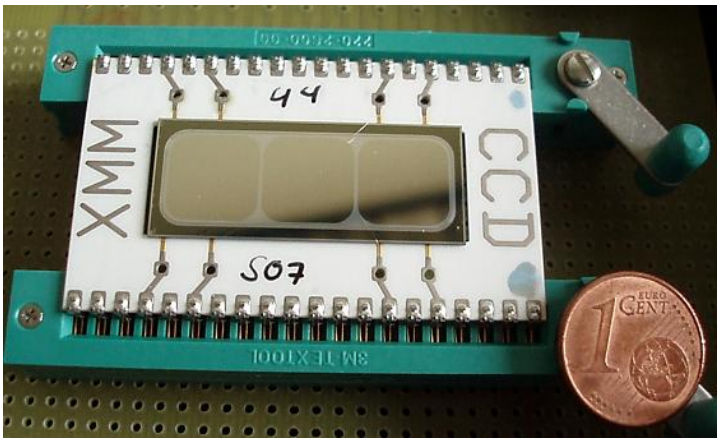

Figure 4.3: The detector chip used in *a*SPECT.

radius. This results in a maximum drift length of the charge carriers of 6.4 mm. The total size of the chip is $34 \times 14 \times 0.45\,\mathrm{mm}^3$. A picture of the entrance side of the detector can be seen in fig. 4.3.

To create the potential valley, 73 rings with distances from 70 to 95 μm are implemented on the backside of the detector, requiring voltage step of about 3 to 3.5 volts from one ring to the next. The entrance side of the detector is covered with a protective layer of 30 nm of aluminium. Each single pad is surrounded by a separation mesh. A common multi guard ring structure surrounds all three pads to reduce the leakage current on both entrance and ring structure side.

A special feature of this detector is the amplifying FET[1] on the detector chip itself. Compared to conventional detectors this minimises the cable length from the detector to the first amplification stage to essentially zero and thus decreases the capacitive noise and the pick-up of external noise. Every cable acts as an antenna and picks up electrostatic noise. The length of the cable from the detector to the first amplifying device is crucial, as the non-amplified signals are very small. Furthermore, a temperature diode is implemented on the detector chip which changes its output voltage depending on the temperature.

The chip is supplied by PNSensor on a special, UHV-suitable ceramics

[1]Field-effect transistor.

board. To provide an electrical connection wires are bonded between the chip and the board. 7 bond pads with a size of $150 \times 150\,\mu\text{m}^2$ are arranged in the centre of each pad on the ring structure side. The ceramics board has 40 pins with a pitch of 0.1 inch. This is a standard distance as the chip is meant to be inserted in two 20 socket zero-insertion-force connectors like the ones shown in fig. 4.3. Unfortunately these commercially available connectors are not suitable for UHV, thus a special holder for the use inside the spectrometer was designed. This holder is constructed out of only ceramics, stainless steel, and gold coated springs. On one side the detector is introduced and clamped, on the other side the holder offers a 50 pin SUB-D connector to connect it to the detector mechanics.

4.3.2 Mechanical setup

During the measurement the detector has to be placed in the high magnetic field that guides and focuses the protons onto the detector. Thus the detector has to be inside the cold bore tube of *a*SPECT. However, if maintenance is needed during the beam time, the detector should be rather easily accessible. Due to the cold bore tube, the cryostat has to be warm before it can be opened. Warming up the cryostat and cooling it back down takes at least ten days, so this is not an option to access the detector.

Instead, a retractable system is used, where the detector can be moved out of the magnet. Then the main bore tube is separated from the detector vacuum by a CF 150 UHV[2] gate valve and the detector can be maintained without venting the main bore tube.

A detailed sketch of the mechanical setup is given in fig. 4.4. The mechanics can be divided into two parts. The lower part is on high voltage, the upper part stays on ground potential. These two parts are electrically separated by a ceramics tube with CF 35 flanges. The high voltage part consists of two nested tubes. The inner tube has a indium sealed flange to allow a larger diameter of the lower part of the tube which houses the preamplifier. Unfortunately, non-magnetic insulators are only available with CF 35 or smaller flanges, but the preamplifier is too big to fit through such a small flange. Outside the closed lower end of the inner tube, the detector

[2]CF: Conflat®, a vacuum flange system with copper gaskets suitable for ultra high vacuum (UHV).

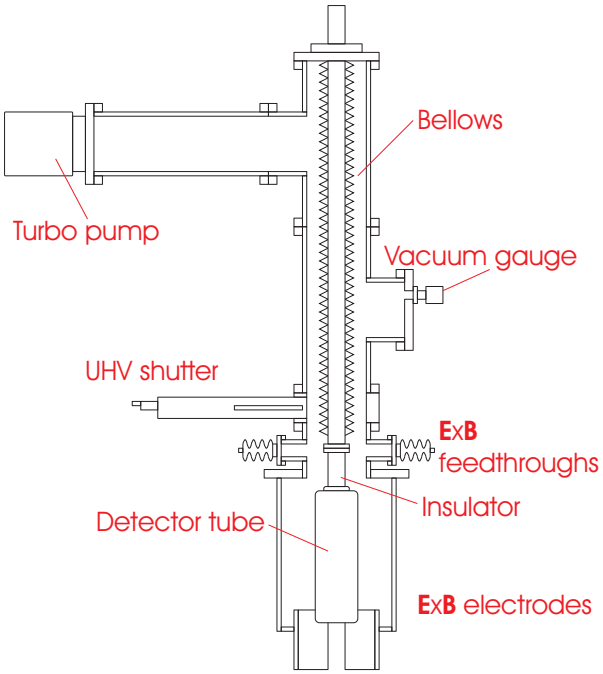

Figure 4.4: The mechanics to move the detector and the upper $\vec{E} \times \vec{B}$ electrode. The sketch shows the mechanics with the detector inside the spectrometer.

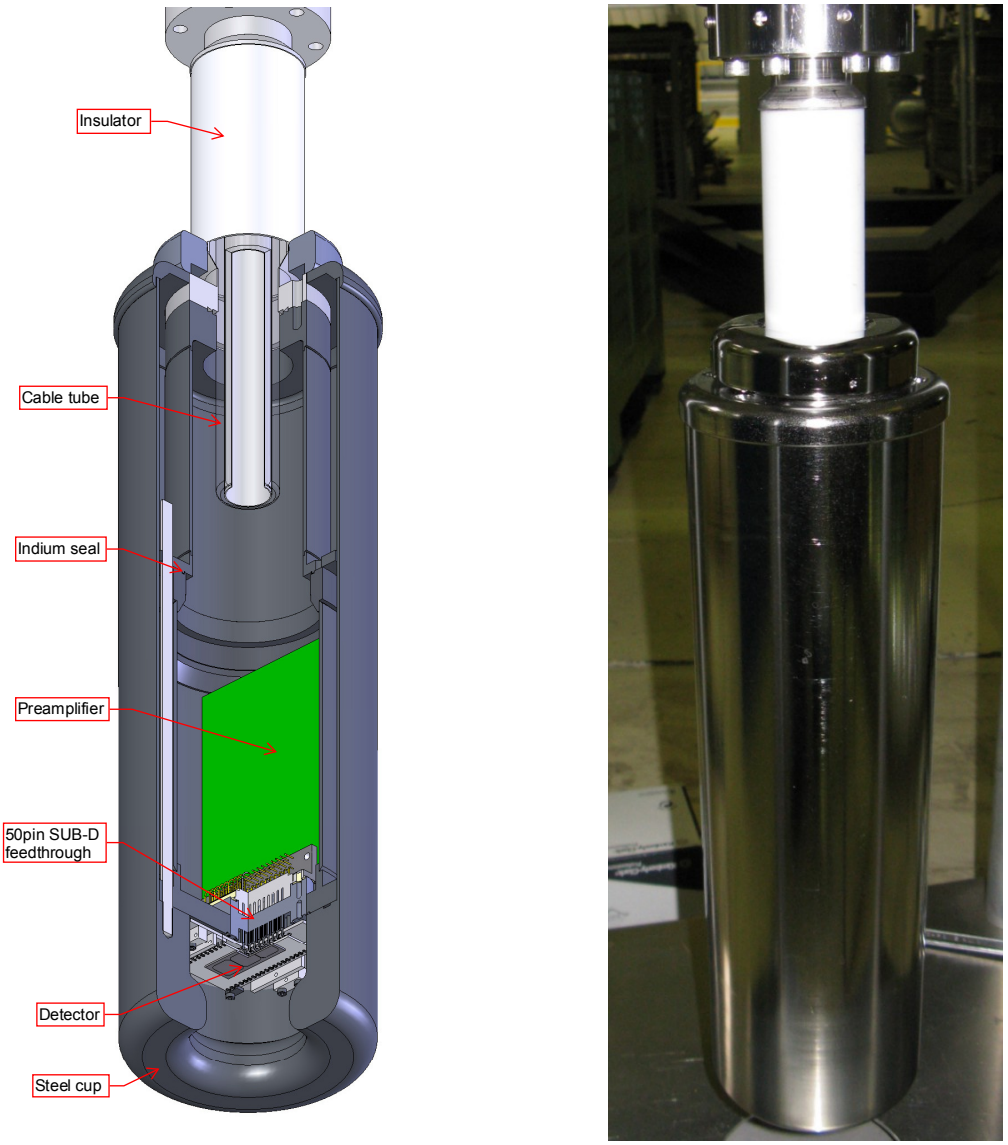

(a) (b)

Figure 4.5: a) Detailed drawing of the high voltage part. b) Photograph of the insulator, the preamplifier-tube, and the shielding cup.

is mounted. To connect the detector to the preamplifier a 50 pin UHV SUB-D feedthrough[3] is used. The detector is surrounded by the outer tube which has a massive stainless steel cup on the bottom to shield the detector from radioactive background (mostly γ's from the neutron apertures and from neighbouring instruments). The outer diameter of the tube is about 110 mm. To let the protons and electrons from the neutron decay access the detector, the cup has a round hole with a diameter of 45 mm. Furthermore, all edges of the outer tube are carefully rounded and electro-polished to avoid electrical breakdowns. The screws to connect the insulator to the preamplifier tube are covered with two semicircular, rounded, and electro-polished pieces.

A membrane bellows is connected to the ground potential side of the insulator. It separates the inner steel tube, which is on atmospheric pressure, from the UHV inside the spectrometer and it also makes the movement of the lower part possible.

The digital part of the electronics is too large and generates too much excess heat to be placed inside the cryostat and thus is mounted on top of the setup inside an aluminium box for electrical shielding. The aluminium box in turn is inside a bigger perspex box to protect people against the high voltage. The cables to connect the two parts of the electronics are contained in an acrylic glass tube inside the central stainless steel tube. A thin walled steel tube that just fits inside the acrylic tube is connected to the high voltage and thus ensures that the cables are inside a homogeneous potential. Furthermore, it helps to shield the cables against electrostatic noise. A plastic tube, which is also inside the central tube, is used to blow pressurised air for cooling onto the preamplifier board. The air escapes through the central tube and thereby also ensures that no water can condense on the inside of the ceramics tube. The ceramics tube is cooled passively by the surrounding, cold spectrometer walls. Water on the inside of the tube may cause electrical brakedowns. A second pressurised air tube is used to cool the digital electronics inside the aluminium box.

The entire setup is contained in two T-shaped CF 150 vacuum pieces. At the upper side access, a turbo-molecular pump is attached to evacuate the setup after it has been attached to the spectrometer. A vacuum sensor is attached to the lower side access. The setup can be moved vertically by

[3] Ceramaseal 16804-01-W.

means of a gear drive which is mounted on the outside of the T-pieces and connected to the central stainless steel tube. The membrane bellows allows for a total movement distance of about 70 cm, which is enough to extract the detector from its measurement position to behind the UHV gate valve. If the detector is in this retracted position, closing the valve separates the vacuum inside the setup from the main vacuum of the spectrometer and the setup can be aired and detached from *a*SPECT.

If the detector is in its retracted position, the central tube sticks out over the two T-pieces and the entire setup is too high for the surroundings in the guide hall of the ILL. A bridge crane is installed to transport heavy loads. The height of the bridge is lower than the height of the retracted detector mechanics. It is possible to install the detector mechanics, but the crane would be blocked as long as the mechanics are retracted. Due to the high vacuum demands it takes a long time until the detector can be moved into the spectrometer. To avoid the crane to be blocked for long times, both parts of the central tube can be separated roughly in the middle with threads. The moveable part is fastened with a clamp, then the connection to the gear drive is removed and the tubes are separated. Hence, the crane is only blocked for some minutes during the insertion of the detector.

4.4 Signal processing electronics

4.4.1 The amplification boards

To achieve the shortest possible distance between detector and amplification[4] the preamplifier board is directly connected with a 50 pin SUB-D connector on its one end to the detector feedthrough. A picture of the board can be seen in fig. 4.6. The signals coming from each pad of the detector are amplified in two steps first by three Amptek A250 chips (one per detector channel) and then by one Analog Devices AD 8024 chip. This chip can process up to 4 channels, 3 channels are used, the fourth is not needed in *a*SPECT and thus grounded. After the amplification, the signals are transferred by 3 coaxial cables in the central tube of the detector mechanics (see fig. 4.5) to the outside of the spectrometer.

[4] A long cable between detector and amplification results in high electronic noise.

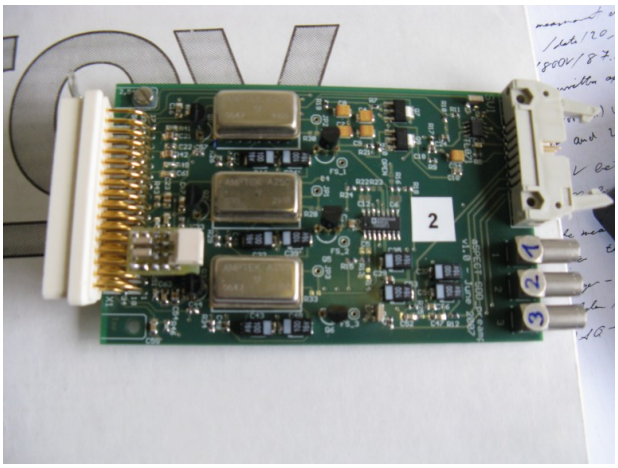

Figure 4.6: The preamplifier board.

Furthermore, a readout circuit for the temperature diode on the detector chip is implemented on this board. The board also serves to distribute the various voltages needed to operate the detector. These voltages are fed to the preamplifier board through the central tube of the mechanics as well, by a 16-core ribbon cable.

The signals coming from the preamplifier are fed into an adapter board inside the aluminium box on top of the spectrometer. This board shapes the signals and distributes them to the ADC. The raw signals from the detector consist of a steep rising part and a long exponentially falling part. The shaper is mostly sensitive to the rising part and shortens the pulse, so it can be treated by the digital electronics. The shaping is done by a chain of two Analog Devices AD 847N and one AD 8138 chip for each channel. This board also distributes the different voltages from the voltage divider board (see sect. 4.4.5) to the different parts of the electronics.

4.4.2 Digital electronics and the trigger algorithm

The last part of the signal processing electronics is the sADC[5] board. This board is also installed in the aluminium box on top of the spectrometer

[5]Sampling Analogue to Digital Converter. Although several other tasks are performed by this board it is usually just called “the sADC”.

and allows to analyse signals from up to 32 channels in parallel. It was already used for the previous detector, a conventional silicon PIN diode with 25 strips [39]. With the new SDD only three channels are used for the detector signals, another one is used for the readout of the temperature diode on the detector chip. The sADC board already performed well in the previous beam time, thus we decided to keep it the same. For each channel, the signals coming from the preamplifier are continuously digitised by a 12 bit ADC. The sampling frequency is 20 MHz, resulting in time bins with a width of 50 ns. The events typically have a length of about 5 μs, so this frequency offers a decent compromise of a good resolution in time while keeping the data volume on a reasonable level.

After digitising the signals are treated by two Xilinx Virtex-II 1000 field programmable gate arrays (FPGA). Each FPGA provides data buffering and processing for 16 channels. The full amount of data sampled by the ADCs is far too large to be stored on a conventional personal computer (about 28.6 MB/s per channel), thus the data is analysed by the two FPGAs with respect to a trigger algorithm. This trigger algorithm is necessary as there is no external trigger in our experiment.

The data from the ADC is continuously shifted through a register and discarded at the end if no pulse was detected. The general algorithm is based on the comparison of two windows within the shift register. If the mean values of those two windows differ by more than an externally set threshold, the trigger condition is fulfilled. As shown in fig. 4.7, window w1 is used to determine the baseline, whereas w2 is separated from w1 by the window distance. If an event is registered by the electronics, the mean value of w2 will be higher than the one of w1 and the threshold condition is fulfilled. An additional parameter in the algorithm, called delay, can be set, so that this threshold condition has to be fulfilled several times in a row before a trigger decision is made. This feature helps to suppress triggers on noise. The exact stored region around the event is determined by the length of the event window and the trigger buffer. This buffer ensures that a sufficient amount of data before the event is stored.

This trigger algorithm is used in various experiments [40]. In the case of the *a*SPECT electronics, the lengths of the two windows w1 and w2, the trigger buffer, and the event window as well as the delay can be set from the control program, the window distance is fixed to 16 time bins. For most

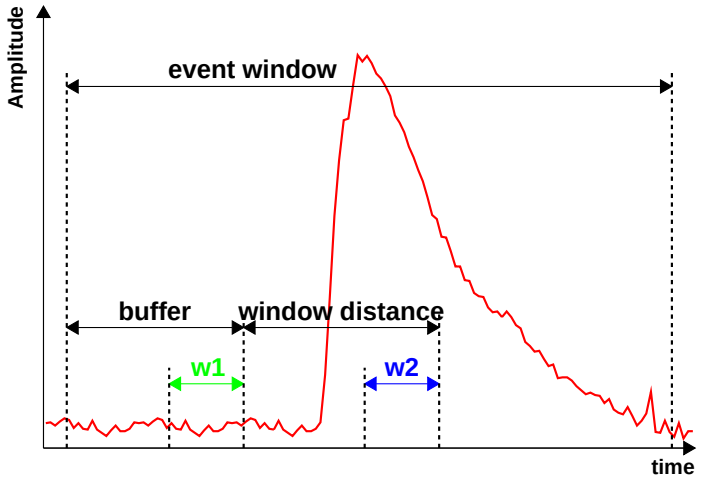

Figure 4.7: General overview of the average windows and buffer used by the trigger algorithm.

of the measurements during the beam time, both w1 and w2 were set to a length of 16 time bins, the delay was 3, the trigger buffer had a length of 15, and the event window 100 time bins.

In case of a trigger the data of the corresponding channel is stored in a buffer on the sADC board. This buffer can store up to 1024 ADC values and is operated according to a first in - first out (FIFO) principle. The events are pulled from the buffer by a multiplexer in a ring. This means a FPGA checks one channel after another if it has data waiting. After channel 32 was checked, the procedure starts again at channel 1. If a channel has data waiting, the FPGA attaches a header with additional information[6] about the pulse and sends it to the DAQ computer via a HOTLINK interface. This optical data transfer standard allows us to operate the sADC board on the same high voltage as the detector, while the DAQ computer is on earth potential. To avoid unnecessary events all unused channels are set to very high thresholds, so that no trigger can occur in those channels.

The data from the sADC board is received by a card mounted in one

[6]See sect. 4.4.3 for details on the header.

of the Peripheral Component Interconnect (PCI) buses in the DAQ PC. As can be seen in fig. 4.8, this PCI card consists of a mother card which is actually plugged into the PCI bus and a mezzanine card plugged into a socket on the mother card. The mother card is a standard card developed for the COMPASS experiment [41], where the S-LINK standard is used for data transfer to the DAQ PC. The mezzanine card is needed, as *a*SPECT uses the HOTLINK standard for data transfer.

Data retrieved by the mezzanine card is passed on to a FPGA on the mother card which stores the data in a standard 512 MB SDRAM chip mounted on the mother card. From this memory buffer the data can be accessed by the PC via the PCI bus and finally be stored on the hard drive of the PC.

4.4.3 Data structure

The data written to the hard drive of the DAQ PC has a defined structure for each event, shown in table 4.1. Each event consists of 32 bit data words. There are five header words, followed by the words containing the ADC values, and finally one footer word. As the ADC has only 12 bit, each word contains two ADC values plus 8 unused bits.

For the data analysis only the ADC header, the time stamp, and the ADC values are important. The binary structure of the ADC header is shown in table 4.2. Each ADC header starts with the binary sequence 10000, followed by the heartbeat bit h, the slow-control bit s, and the overflow bit o. The firmware of the sADC offers the possibility to send out events without a trigger after a certain time has passed, the so-called heartbeat. This feature can be used for diagnostics of the sADC, for those events the heartbeat bit is set, for normal events this bit is 0. One of the ADC channels is used to read the temperature diode of the detector. As there is no trigger for this channel, similarly to the heartbeat, temperature events are sent by the sADC board every two seconds without a trigger. These events are marked by the slow control bit. The overflow bit is set, if the FIFO buffer is full and the event cannot be buffered any more. In this case, only the time stamp is recorded. This would point to a too high event rate and a possible loss of data. Under normal conditions this does not happen during the measurements at the neutron beam. The overflow bit is followed by three zeros, then five bits denote the ADC channel of the event. After four

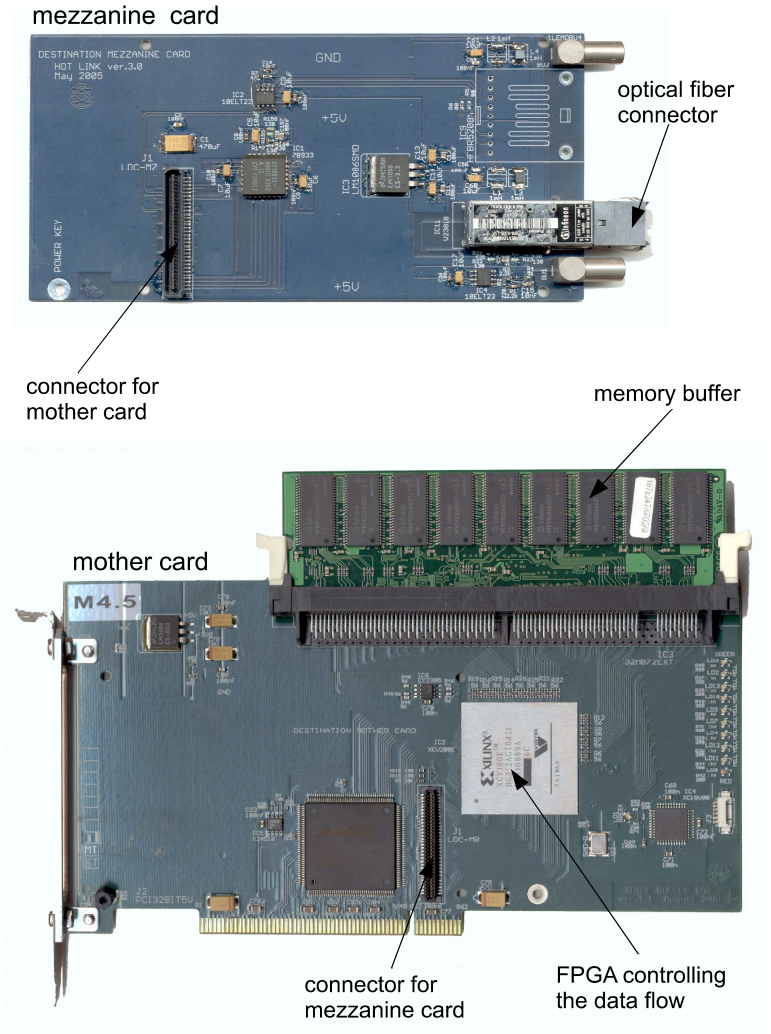

Figure 4.8: The interface card mounted in the DAQ PC to communicate with the sADC. Pictures take from [39].

0 word (32 bit)			
S-LINK header 1 (32 bit)			
S-LINK header 2 (32 bit)			
S-LINK header 3 (32 bit)			
ADC header (32 bit)			
0	1	time stamp (30 bit)	
unused (8 bit)		ADC data (12 bit)	ADC value (12 bit)
⋮			
unused (8 bit)		ADC data (12 bit)	ADC value (12 bit)
footer (32 bit)			

Table 4.1: Structure of one event.

1	0000	h	s	o	000	channel (5 bit)	0000	size (12 bit)

Table 4.2: Structure of the ADC header.

more zeros, 12 bit are reserved for the size of the event, i.e. the number of words the event consists of. This allows to cross check if the event was completely retrieved by the PC.

4.4.4 Readout software

The user interface to control the interactions with the sADC is based on LabVIEW™. This software is developed by National Instruments and is optimised for the control of any kind of electrical device. It offers a graphical user interface (GUI) both for programming and user interaction. In our detector control application it interacts with the electronics by calling C

libraries. This way, the GUI does not interfere with the data stream, but still it is possible to decode selected events while the measurement is running and display the shape of those events in a histogram on the GUI, similar to the picture on an oscilloscope. Furthermore several other informations (e.g., the measurement time and the event rate) are displayed. This offers the possibility to check the results of the measurement online.

After one measurement file is completed, the data structure has to be converted to a format suitable for data analysis. This step is usually called decoding and is done by a C/C++ program. For the analysis the ROOT [42] code is used, the decoding program creates a ROOT tree with all important information about every event from the raw data file[7]. Furthermore for each event the program calculates a baseline from the mean value of the first 15 ADC values, a preliminary pulse-height value from the maximum difference of the signal and the baseline, and a file with simple pulse-height histograms.

4.4.5 Powering of the electronics

The SDD and the electronics need several different supply voltages from 5 to $\sim 200\,\mathrm{V}$ to be operated correctly[8]. All these voltages have to be provided on the high potential of the acceleration voltage.

To reduce the amount of needed power supplies, an additional voltage converter board was designed. This board creates the needed voltages from the three input voltages ± 30 and $0\,\mathrm{V}$ with the help of several DCDC voltage converters.

The input voltages are created by two laboratory power supplies also on the high potential of the acceleration voltage. The power supplies are connected to the standard $230\,\mathrm{V}$ AC power via an insulating transformer. In this transformer the primary and secondary windings are electrically separated, so that the power can be fed to the primary side of the transformer on earth potential and taken out on the secondary side on high voltage. To protect against the high voltage, both power supplies and the insulating transformer are inside a second perspex box usually situated on top of the anti-magnetic iron screen of the spectrometer.

[7] See app. A.3 for details on the structure of the ROOT tree.
[8] See app. A.1 for the values of the needed voltages for the detectors.

4.5 Simulations of detector properties

To simulate the properties of the detector the program SRIM (short for "The stopping and range of ions in matter", [43]) was used. The input for this program was created by using the theoretically expected distribution of proton energy and angles in the decay volume. If, according to the transmission function eq. (3.26), the proton overcomes the analysing plane its energy and impact angle on the detector are calculated and the simulation is run with these parameters. SRIM produces an output file with the position and kinetic energy of each proton after it lost a given amount of energy. If this energy is chosen small enough, the position after each scattering process is given. From these values the expected pulse-height has to be inferred.

4.5.1 The partial event model

Low energy protons penetrate only about 0.2 μm into the detector, thus the efficiency of a detector for proton detection is extremely sensitive to the detector properties near the surface. A proton penetrating the detector has first to overcome the entrance window, 30 nm of aluminium in our case. Free charge carriers produced by the proton in this region will not be detected at all. Even after the entrance window not all charge carriers will be collected in the central anode of the detector. Close to the surface a large fraction of the created electrons and holes will recombine. The charge collection efficiency (CCE) can be described by the partial event model [44]:

$$f_{\mathrm{CCE}}(z) = \begin{cases} 0 & \text{if } z < 0 \\ S + B\left(\frac{z}{l}\right)^c & \text{if } 0 \le z \le l, \\ 1 - Ae^{-\frac{z-l}{\tau}} & \text{if } l \le z \le D \end{cases} \tag{4.2}$$

where z is the depth into the detector with $z = 0$ at the transition from the aluminium window to active silicon region. The total thickness D of the detector is about 450 μm. As this is much thicker than the maximum penetration depth of low energy protons, the exact thickness of the detector is of minor importance for us.

The parameters A and B can be eliminated by the condition of a conti-

nuous and differentiable transition at $z = l$:

$$A = (1 - S) \cdot \frac{\tau c}{l + \tau c} \tag{4.3}$$

$$B = (1 - S) \cdot \left(1 - \frac{\tau c}{l + \tau c}\right). \tag{4.4}$$

The 4 remaining parameters are:

- S describes the minimum fraction of collected electrons and thus the value of the CCE at $z = 0$. S can take values between 0 and 1, for our detectors $S \approx 0.4$.
- l defines the depth of the transition from the second to the third part of the CCE function. Typically this is about 50 to 100 nm.
- c defines the curvature of the CCE function at $z = l$. Typically $1 < c < 2$.
- τ is the rise of the exponential part of the function and defines how fast the CCE goes to 1. Typical values are about 100 nm.

A simulation now has to provide the path of a proton into the detector and its energy loss at any point of the path. The exact values of the variables depend on the detector and have to be found by matching measured spectra with different systematics (e.g., different acceleration voltages) to the results of the simulation.

4.5.2 Results of the simulations

Penetration depth and energy loss distribution

The simulations show how deep into the detector the protons penetrate and the distribution of the energy loss. Fig. 4.9 shows the distributions of the maximum penetration depth and energy loss of 96352 protons. The maximum penetration depth is not necessarily equal to the stopping point of the proton. A proton changes its direction inside the detector with every scattering process, so it is possible that it enters the detector to a certain depth and then turns around and stops less deep inside the detector or even leaves the detector again.

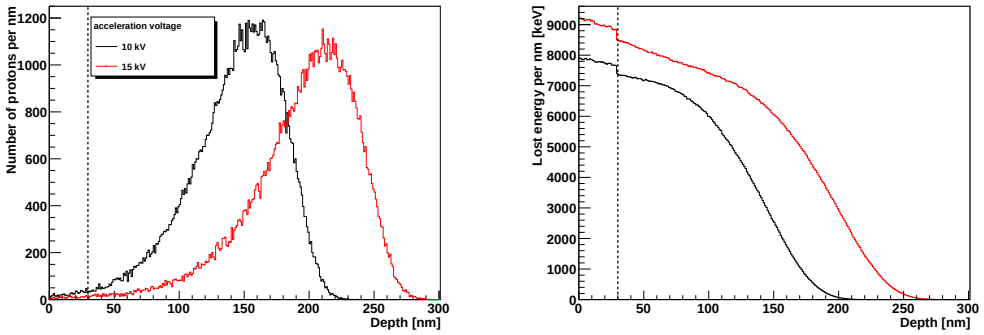

(a) Maximum penetration depth.

(b) Energy lost by 96352 protons, each with an impact energy of 15 kV (red) .

Figure 4.9: Simulation of maximum penetration depth and energy loss of protons as they are expected for a measurement with 50 V in the analysing plane and with 10 and 15 kV detector high voltage. The dashed lines denote the transition from the dead layer to the active region of the detector.

For an acceleration voltage of 10 kV the protons reach a mean maximum depth of 143 nm, for 15 kV this increases to 195 nm. The median is 148 nm for 10 kV and 203 nm for 15 kV.

Reproduction of proton spectra

To construct the pulse-height spectrum from the results of the SRIM simulation, the energy loss has to be combined with the CCE at each point and for each proton. The parameters of the CCE have to be tuned to reproduce the different measured spectra. Furthermore, an artificial broadening of the simulated spectra is necessary to take the noise of the electronics into account.

To determine the parameters of the charge collection efficiency function, measurements for each measured analysing plane voltage, with 10 and 15 kV acceleration voltage were compared to the results of the simulation. By variation of the parameters they were determined to: $S = 0.40$, $\tau = 70\,\text{nm}$, $c = 1.57$, and $l = 56\,\text{nm}$. The simulation gives the energy loss of the protons in units of keV. Tto convert this to the pulse-height values from

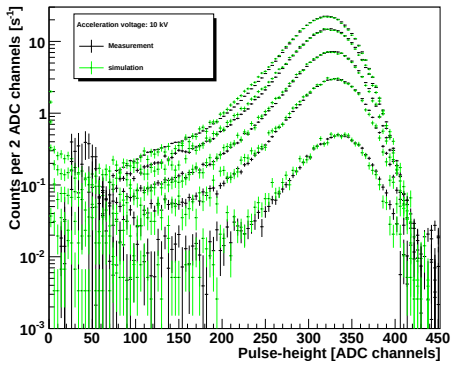

(a) Acceleration voltage 10 kV, measured data from from May 11$^{\text{th}}$, 2008/night.

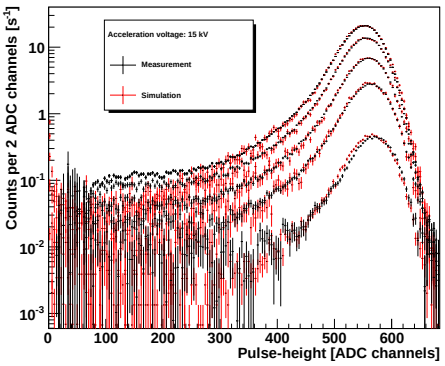

(b) Acceleration voltage 15 kV, measured data from from May 20$^{\text{th}}$, 2008/night.

Figure 4.10: Comparison of the results of the simulations with spectra from the beam time. Each picture shows spectra for analysing plane voltages of 50, 250, 400, 500, and 600 V. The background has been subtracted by subtracting the 780 V measurements. Each spectrum shows the sum of all measurements with the according voltage of that day to achieve better statistics.

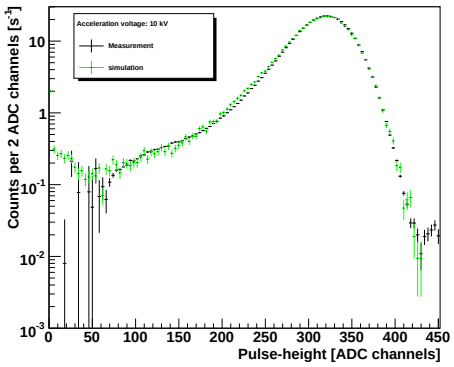

(a) Acceleration voltage 10 kV.

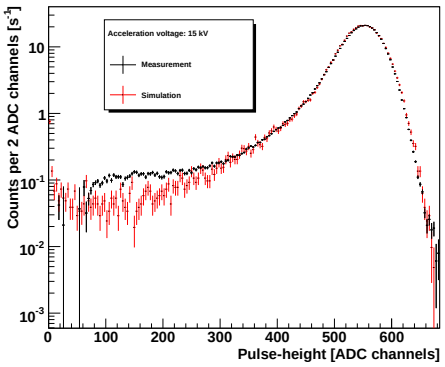

(b) Acceleration voltage 15 kV.

Figure 4.11: Comparison of the results of the simulations with the 50 V spectrum from the beam time, same data as in fig 4.10. The count rate at low pulse-heights cannot be reproduced by the simulations.

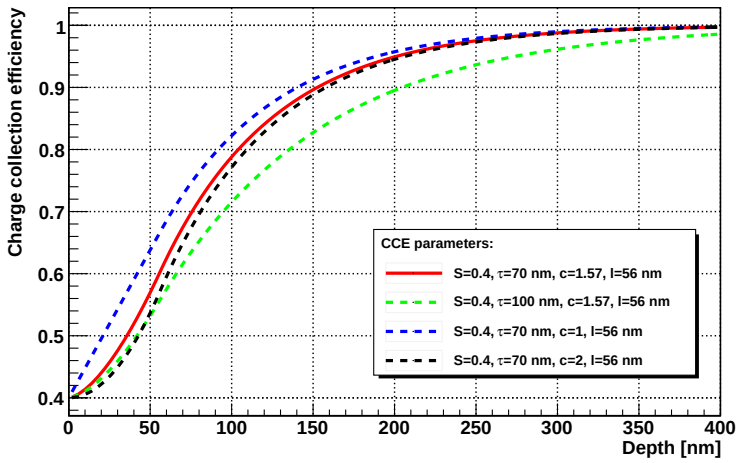

Figure 4.12: The shape of the charge collection efficiency function for different parameters. The solid, red line shows the valid CCE for the *a*SPECT detector, the dashed lines are examples for other possible shapes. In contrast to fig. 4.9 the scale on the x-axis denotes the depth of the active layer of the detector according to the definition of the CCE in eq. 4.2.

the measurements a factor of 63 ADC channels/keV was established by variation as well. The shape of the CCE is shown in fig. 4.12.

Although the main proton peaks are reproduced quite well, the simulations for the 15 kV measurements predict the low energy tail of the peak to be much lower than what was measured during the beamtime. The low energy tail is caused by protons that are backscattered or loose more energy in the dead layer or close to the surface of the active layer. The discrepancy for 50 V analysing plane voltage and 15 kV acceleration voltage is shown in fig. 4.11(b). The integral of the measured count rate between bin 80 and bin 300 is $7.03(6)\,\mathrm{s}^{-1}$, the simulation predicts $4.10(14)\,\mathrm{s}^{-1}$. For 10 kV (fig. 4.11(a)) the discrepancy cannot be seen because the peak is not separated well enough from the noise. Here, the integral of the measured count rate between bin 80 and bin 200 is $12.07(5)\,\mathrm{s}^{-1}$, the simulation predicts $11.95(24)\,\mathrm{s}^{-1}$.

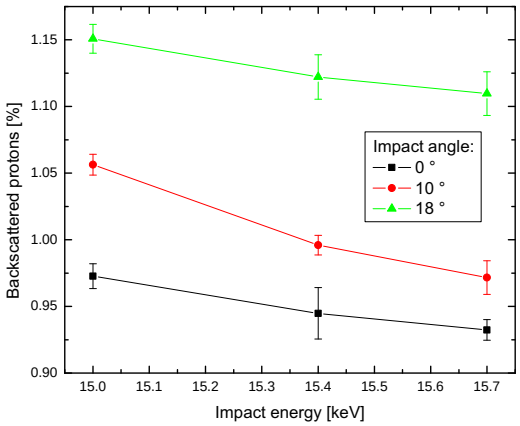

Figure 4.13: Backscattering probabilities for protons with three different impact energies and angles. Each point shows the backscattering probability of 600 000 protons.

The simulated spectra can now be used to reconstruct the proton counts below the detection limit, see sect. 6.2.4.

Backscattering of protons

A fraction of the protons hitting the detector will be backscattered. This means the proton enters the detector, is scattered several times inside the detector, and finally leaves the detector again. Due to the acceleration voltage, the proton will not escape towards the bottom of the spectrometer, but it will hit the detector again with the same energy and angle as it left the detector. The time difference between two hits is rather short ($\approx 0.5\,\mu$s), thus it is not possible that one backscattered proton is counted as two events.

Independent of actual backscattering, it is also possible that an absorbed proton does not deposit enough energy in the active region of the detector to be detected. In turn a backscattered proton might loose enough energy in the active layer to be detected.

From the simulations a relative amount of backscattered protons of 1.8 %

at 10 kV and 1.0 % at 15 kV acceleration voltage is expected. However, the differences for the initial energy spread of the decay protons are fairly small. Fig. 4.13 shows the different backscattering probabilities for protons with different impact angles and energies.

4.5.3 Electron simulations

Besides the protons also a fraction of the electrons hits the detector. These electrons form the biggest part of the background in the measurement. In contrast to the low-energetic protons which only penetrate the very surface of the detector, the electrons reach deeper into the detector or, if they have sufficient energy, even go through it. Furthermore, electrons enter the detector with any angle between 0° and 90°, whereas the protons have rather small penetration angles due to the acceleration voltage. With an acceleration voltage of 15 kV, their maximum angle of impact is about 18°.

As its name already implies, SRIM can only simulate the interaction of ions with matter. For the simulations of electrons inside the detector the program Casino ("Monte Carlo simulation of electron trajectory in solids", [45]) is used. Although this code is optimised for scanning electron microscopy, it also produces reasonable results for electrons with energies as in neutron decay. Yet, Casino is not as versatile as SRIM, it allows to simulate only one energy and impact angle at a time, thus it is not possible to reproduce the full electron energy and angular spectrum as it was done for the protons. For this a more elaborate code (e.g., Geant) would have to be used. However, for this work the results obtained with Casino are sufficient.

The penetration length of the electrons depends on their energy. Electrons with 50 keV kinetic energy in average only penetrate 10.6 μm into silicon, electrons with 750 keV penetrate 935 μm. The detector has a thickness of about 450 μm, hence a large fraction of the high energetic electrons only deposit part of their energy in the detector. The number of backscattered and transmitted electrons depends on the impact energy and angle. The predictions of the simulations for different combinations are shown in fig. 4.14.

From the amounts and the energy spectra of the backscattered and transmitted electrons, the energy deposited in the detector can be calculated. Each backscattered electron leaves the difference of entrance energy and

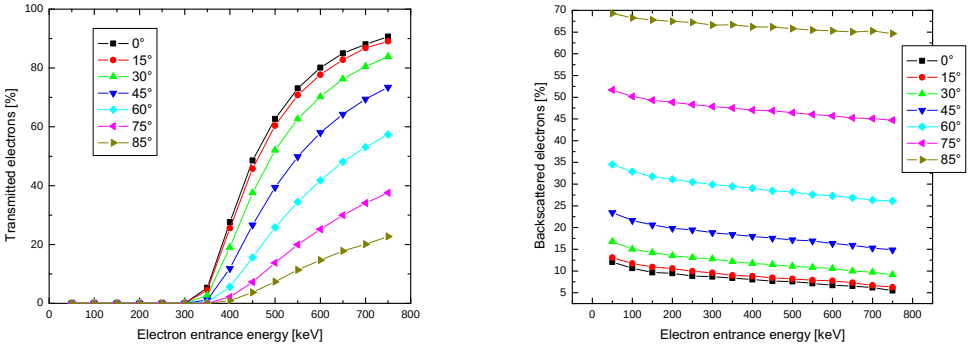

(a)

(b)

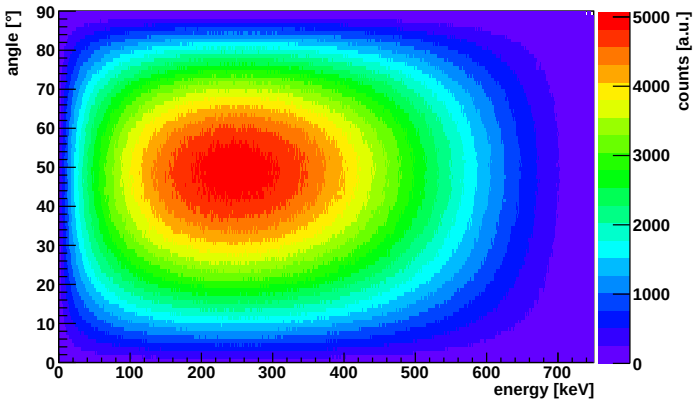

(c)

Figure 4.14: Relative amounts of (a) transmitted and (b) backscattered electrons according to the simulations for different impact angles. The scatter plot (c) shows the distribution of the angles and energies of electrons that reach the detector at 15 kV acceleration voltage. 0° is the direction perpendicular to the surface of the detector. This picture was generated by G. Konrad using a set of Monte Carlo generated electrons and simulating their path through the spectrometer [28].

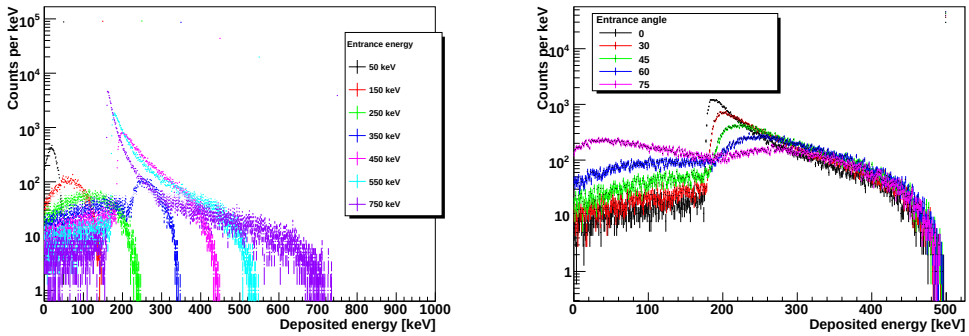

(a) Impact angle 0°.

(b) Impact energy 500 keV.

Figure 4.15: Spectra of the energy deposited in the detector by the electrons for fixed impact angle (a) and energy (b). The broad distributions are caused by backscattered, the peaks by transmitted electrons. The absorbed electrons deposit all their energy in the detector and thus create the high count rates in the bin corresponding to their entrance energy.

backscattered energy in the detector. The same relation holds for transmitted electrons. Electrons that are neither backscattered nor transmitted are stopped inside the detector and thus deposit all their energy in it. Energy spectra for different impact angles and energies are shown in fig. 4.15.

Regardless of its impact energy and angle, any electron may be stopped inside the detector and thus deposit all its energy. Electrons that loose much energy in the detector saturate the electronics, this effect is described in sec. 6.5.

4.6 Investigations of detector properties

4.6.1 Energy calibration

The output of the electronics is a pulse-height in ADC channels which is proportional to the energy deposited in the active layer of the detector. To convert the pulse-height into energy, the detector was calibrated with radioactive sources before it was installed in the spectrometer. An ideal source for the calibration would be ^{55}Fe which decays to ^{55}Mn via electron cap-

ture and produces two strong and clean X-ray lines at 5.9 (K_α) and 6.5 keV (K_β) [46]. Unfortunately, these lines are too low energetic to be resolved by the detector at room temperature. There was no cooling housing available during the beamtime, and the source cannot be placed close enough to the detector if the detector is installed in the spectrometer.

Therefore, the calibration was done with ^{133}Ba, which decays to ^{133}Cs via electron capture. It produces a rather complicated spectrum with both nuclear gammas and X-rays. The strongest peaks are the K_α lines at 31.0 and 30.6 keV, several K_β lines between 34.9 and 35.3 keV [47] and the gamma transition lines at 81.0 and 356.0 keV [48].

The gamma transitions are too high energetic and saturate the electronics. For the calibration of the detector three peaks were used: The K_α and K_β lines[9], as well as the K_α escape line. X-rays are absorbed photoelectrically in the silicon bulk material of the detector, leaving K-shell ionised silicon atoms. These atoms emit either Auger electrons or X-rays. The electrons have a very short free range in the detector and are reabsorbed, but the X-rays have a substantial probability to leave the detector. In that case, the detected energy is reduced by the energy of the silicon X-ray, in our case [49]

(4.5)
$$E_{\text{escape}} = E_{\text{Ba},K_\alpha} - E_{\text{Si},K_\alpha} = 30.85(10)\,\text{keV} - 1.74\,\text{keV} = 29.11(10)\,\text{keV}.$$

With these considerations a superposition of three Gaussian peaks was fitted to the calibration spectrum shown in fig. 4.16. From the positions of the three peaks the following calibration curve for the detector at room temperature was determined:

(4.6)
$$Ph = -4.4(80) + 65.8(3) \cdot E_{\text{Det}},$$

where Ph is the detected pulse-height in units of ADC channels and E_{Det} the energy that was detected by the detector.

The conversion factor of about 66 ADC channels/keV differs slightly from the result of the proton simulations of 63 ADC channels/keV. This can be

[9] The resolution of the detector at room temperature is not high enough to separate the single K_α and K_β lines, thus averaged energies of $E_{\text{Ba},K_\alpha} = 30.85(10)\,\text{keV}$ and $E_{K_\beta} = 35.1(2)\,\text{keV}$ were used.

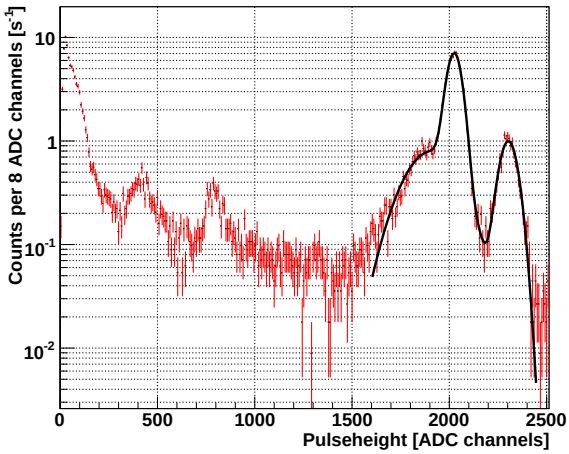

Figure 4.16: A spectrum of ^{133}Ba taken with the SDD at room temperature (red). The K_α, K_β and the escape line were fitted with three superimposed Gaussian peaks (black).

explained by the temperature of the detector. While the ^{133}Ba spectrum was taken at room temperature, the proton spectra were taken with the cooled detector. Cooling the detector reduces its sensitivity. This effect was already observed with a small test detector [38].

4.6.2 The *paff* accelerator

In order to investigate the detectors of *a*SPECT, but also for other experiments one needs a proton beam with comparable properties as the protons from neutron decay after acceleration in the spectrometer. A small accelerator was set up at the Technische Universität München to provide such protons.

This accelerator (called "proton accelerator with femto ampere flux" or "*paff*") produces protons from neutral hydrogen molecules in an extractor type ion source[10]. Similar to the acceleration principle in *a*SPECT, where the detector is put to high voltage, here the ion source is on high voltage. The beam tube is electrically separated by a CF100 insulator tube. Ions

[10]SPECS IQE 11/35 [50]

passing through this tube are accelerated towards a 30° bending magnet. In the source not only protons but also other types of ions are produced. The bending magnet separates the different types of ions according to their momentum and allows to choose a rather pure proton beam.

After the magnet the beam can be focussed or defocussed by an electrostatic lens. After a flight tube with a length of about 2 m a Faraday cup or a micro channel plate can be moved into the beam for beam diagnostics or count rate normalisation. At the end of the accelerator the detector can be mounted. The vacuum at the measurement position can be separated from the accelerator vacuum by a shutter. This allows to change the detector without venting the accelerator.

Further details on *paff* can be found in [51, 52, 25].

Although the accelerator is producing a proton beam over a wide intensity range, there are still some shortcomings which considerably reduce the usability of the measurement results. Most important, the intensity of the beam is rather unstable over time. To produce the protons hydrogen gas is fed into the ionisation chamber. The amount of produced protons strongly depends on the pressure. Unfortunately there is no active stabilisation of the pressure and it shows large fluctuations. Furthermore, the field strength of the bending magnet is hard to control and it is hard to reproduce the same field. Also, there is no online monitor for the beam which would allow for a correction of the measured count rates. Faraday cup and micro channel plate both block the beam when they are moved in, so only alternating measurements are possible. Also the composition of the beam is not completely understood, yet. For example, depending on the settings of the accelerator, a second peak at low pulse-heights appears in the spectra recorded with the SDD.

4.6.3 Detector test setup

In contrast to the beam time where the detector is installed inside the cold bore tube of the spectrometer, there is no passive source of cooling for the detector if it is installed at the accelerator. Furthermore, for part of the measurements the detector has to be moveable.

To accomplish these requirements, the detector is installed inside a copper housing with an opening for entering particles. The housing is connected

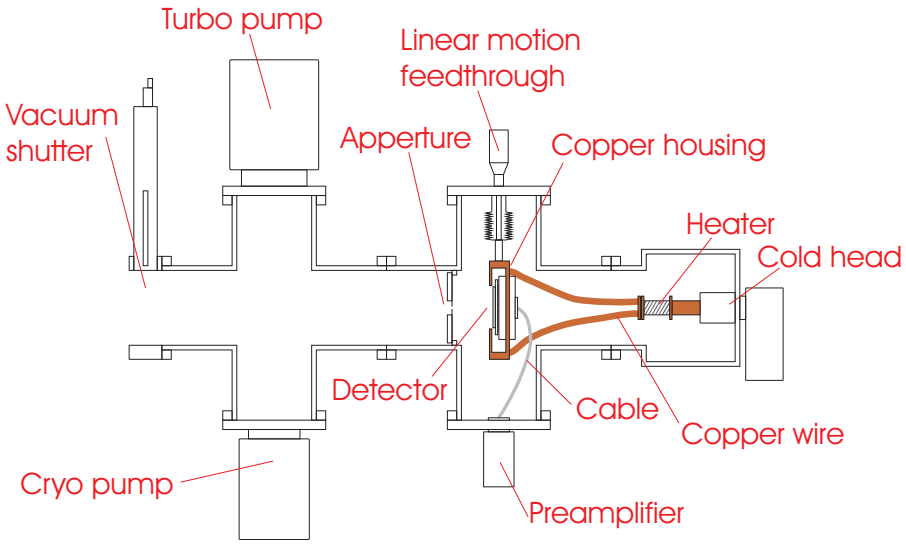

Figure 4.17: The setup for measurements with the *a*SPECT detector at the proton accelerator. Protons from the accelerator enter the setup from the left hand side, are collimated by the aperture, and hit the detector.

to a cold head with integrated heater with flexible copper wires to provide thermal contact. The cold head always runs with the same cooling power and can cool down to below 4 K. As such cold temperature is not needed by the *a*SPECT detectors, the desired temperature of the detector can be chosen by setting the current of the heater. The detector itself is cooled by radiation cooling from the housing.

To obtain a moveable system the detector housing is installed on a linear motion vacuum feedthrough with an attached micrometer screw. A CF100 cross piece is attached to the accelerator. The detector on the feedthrough is mounted from the top, and the cold head on the back. The electrical connection of the detector is done with a short cable with 50 pole SUB-D connectors to the bottom access of the cross piece, where a flange with a matching connector is mounted. The preamplifier is plugged directly into the air side of this connector. A sketch of the setup is shown in fig. 4.17.

The proton beam is collimated shortly before the detector with an aperture with a diameter of about 0.15(5) mm. The aperture consists of an aluminium ring with three thread rods pointing outwards to fix it inside

the beam tube. A piece of normal household aluminium foil with the aperture hole in the middle is attached to the ring. The hole was punched into the foil with a thin wire with a diameter of 0.1 mm, thus its exact diameter is hard to determine. To reduce possible background of electrons or x-rays, produced by protons hitting the aluminium foil, a 5 mm thick aluminium plate with a hole with 3 mm diameter is mounted on top of the foil.

Another possibility would be mounting the detector directly on a flange and use a moveable aperture. The setup with a moveable detector is favourable as, with the fixed aperture, always the same part of the beam is used. Hence, this setup avoids a systematic effect due to the spacial inhomogeneity of the proton beam. The cable between the detector and the preamplifier introduces some minor pick-up noise, but due to the amplification FET on the detector chip, a cable length of up to about 20 cm is possible without loosing too much resolution.

The linear motion feedthrough allows only a movement along one vertical line. A more elaborate setup with a motorised xy-table is under construction. This will allow to automatically scan many different points on the surface of the detector.

4.6.4 Results

First tests with the SDD at the accelerator were done in September 2008. After successful tests of the cooling system, several problems with electrostatic noise had to be solved. Finally a longitudinal scan of the third pad of detector 44-S07 (ADC channel 7) was performed. Special attention was given to the performance of the detector at the edges.

Linear scan

The obtained count rates for the different measured detector positions are shown in fig. 4.18(a). In the centre of the detector the count rate fluctuates due to the fluctuations of the accelerator. The measurements were started at the left side of the picture moving to the right, during the measurements the hydrogen pressure in the source part of the accelerator dropped. During the first measurements the pressure dropped quite fast, then the drop rate reduced. At the edges the measured count rate rises steeply, the shape of

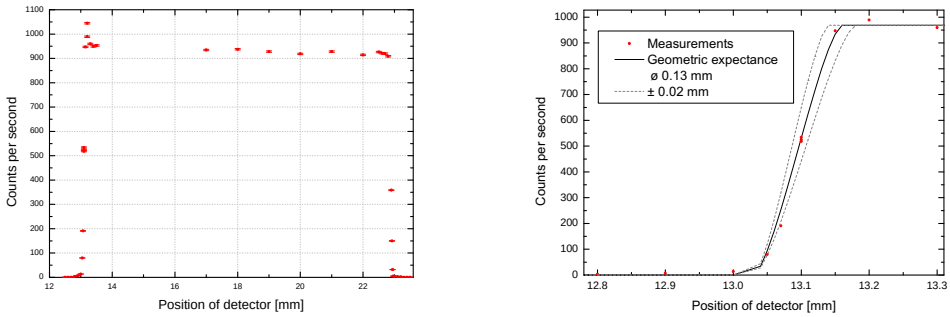

(a) Full pad. (b) Zoom on one edge.

Figure 4.18: One dimensional scan of a detector pad. The values on the x-axes refer to the reading on the micrometer screw of the linear motion feedthrough.

the rise can be explained by the geometric properties of a round aperture with a diameter of 0.13(2) mm. In a first order approximation the edge of the detector can be considered as a sharp line. Protons hitting on the one side of the line are counted, protons on the other side are not. The edge is moved behind a round aperture, the expected count rate is then proportional to a segment of a circle with the diameter of the aperture. Fig. 4.18(b) shows a zoom on the measurements close to the left[11] edge of the detector compared to the geometrically expected count rate. For the right edge a similar picture and the same result was obtained.

In reality the edge of the detector is not a sharp line, but there will be a region where the detection probability of the protons drops from the maximum to zero. Unfortunately the size of the aperture is not known well enough to give a value for the width of the edge. Due to the simplicity of the aperture, the exact diameter cannot be precisely measured, and also a perfect roundness cannot be ensured. Given the geometric value of 0.13(2) mm and the diameter of the aperture of 0.15(5) mm an upper limit of about 50μm can be deduced.

[11] I call it the left edge, as it shows up on the left side of the graph. In reality, the right edge is the border between pads 2 and 3. The left edge is at the end of the chip.

Spectra at the edges

Another interesting effect was discovered during the analysis of these measurements. The pulse-height of the protons and thus the position of the proton peak changes over the detector.

As visible in the spectra in fig. 4.19 the average pulse-height of the protons is reduced close to the edges of the detector and the peak structure changes at the edges. On the right edge only some more protons appear at very low pulse-heights between bin 100 and 200. On the left edge the peak disappears completely at a detector position of about 13.1 mm. It is uncertain if this effect appears all along the outer edges of the detector or if it is localised to a small region around the point which was measured with the linear motion feedthrough. A local effect could be caused by some dust particle on the surface of the detector at that point. Another possibility is that the protons are scattered from a bond that runs close to the measured point.

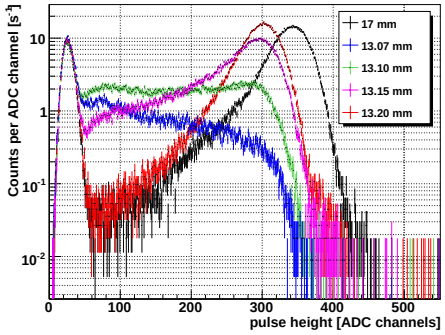

(a) Left edge.

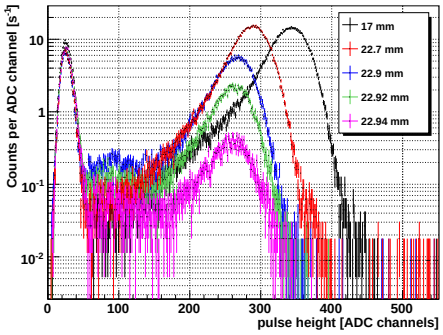

(b) Right edge.

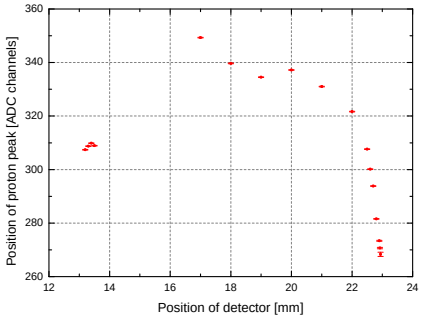

(c) Position of the proton peak depending on the detector position.

Figure 4.19: Proton spectra obtained on the left (a) and right (b) edge of the detector. The spectra at 17 mm are close to the centre of the detector and meant for comparison. c) The proton pulse-height depends on the position of the detector.

5 Beamtime

From November 2007 to June 2008 *a*SPECT was set up at the cold neutron beam position PF1b on the H113 neutron guide at the Institut Laue-Langevin (ILL) in Grenoble, France. The main focus of this beamtime was to identify and study possible systematic effects with sufficient statistical accuracy to provide a value of a with an error bar smaller than the ones given by prior experiments.

5.1 Experimental setup

The PF1b position [53] offers an experimental zone of about $3 \times 10\,\mathrm{m}^2$ (width×length). The neutron guide ends in a casemate before the experimental zone and is closed with an aluminium window. Inside the casemate a supermirror neutron polariser can be moved into the beam. *a*SPECT uses unpolarised neutrons, hence the distance from the end of the neutron guide to the experimental zone was bridged by an additional 2 m piece of guide, followed by a 2 m long aluminium flight tube containing boron apertures to collimate the beam. Both, apertures and additional neutron guide, were inside a long, evacuated beam tube with a diameter of 200 mm. To allow a possible small misalignment between the beam tube and the spectrometer they were connected via two ISO-K 200 bellows. The rough vacua of about 10^{-2} mbar before and after the spectrometer were separated from the main ultra high vacuum ($\sim 10^{-9}$ mbar) by magnesium-aluminium (MgAl3Zn1) alloy windows with thicknesses of 250 μm. The entrance side of the beam tube was closed with an aluminium window.

Biological shielding was provided by layers of boron loaded rubber in- and outside the beam tube and 5 to 10 cm of lead.

5.1.1 Beam tailoring

The initial neutron beam has to be optimised to fulfil several requirements in the decay volume of the spectrometer. The H113 neutron guide has a size of $60\times200\,\mathrm{mm}^2$ (width×height), the additional piece of neutron guide $50\times116\,\mathrm{mm}^2$. The decay volume of the spectrometer is much smaller, hence the beam size has to be reduced. Inside the spectrometer there should be only minimal collimation to avoid background radiation which cannot be shielded. For the same reason no primary neutrons should hit the inner walls. As far as possible also scattered neutrons should hit no walls. Finally, the beam should have a homogeneous spacial distribution over the width of the decay volume to minimise the edge effect[1]. Therefore, a beam profile with a broad, flat central part and sharp edges is desired.

The beam collimation to achieve these requirements always has to be a compromise between clean systematics and good statistics. On the one hand, a long flight path reduces the neutron beam's divergence and results in a clean beam profile, on the other hand a very stringent collimation reduces the amount of neutrons passing through the spectrometer considerably.

The additional neuron guide is smaller than the H113 guide, hence its edges were covered with boron rubber to avoid neutrons damaging the glass plates of the guide. The positions and sizes of the different apertures were optimised with two different Monte-Carlo simulation programs. For details on the simulations the reader is referred to [54]. According to the results of these simulations three apertures before the spectrometer and five apertures inside the spectrometer were used, three before and two after the decay volume.

The main apertures before the spectrometer had a size of $45\times70\,\mathrm{mm}^2$ (width×height). One was placed shortly after the end of the neutron guide, still inside the PF1b casemate, the other one was placed in front of the entrance window of the spectrometer. In between these two apertures a bigger aperture ($50\times75\,\mathrm{mm}^2$) was used to cut away neutrons with a high divergence. According to the simulations the first aperture absorbs about 46 % of the neutrons, the bigger aperture in the middle 21 %, and the one in front of the spectrometer 13 %[2].

[1] See sect. 3.4.6.

[2] The values refer to the number of neutrons at the exit of the additional neutron guide.

Name	Width [mm]	Height [mm]	Distance to DV [mm]	rel. Absorption [%]
n-guide	50	116	3175	
P0	45	70	3174	46
P1	50	75	1600	21
P2	45	70	690	13
Entrance Window	Ø=110		625	
E1	48	80	480	0.3
E2	45	70	280	3
E3	48	80	120	0.1
DV			0	
A1	48	90	-120	0.8
A2	47	80	-280	1
Exit window	Ø=140		-625	
Beamstop			-2270	15

Table 5.1: The collimation system at the ILL: Positions, dimensions, and simulated relative absorption of the apertures before the spectrometer (P0 to P2), on the entrance side (E1 to E3), and on the exit side (A1, A2) of the decay volume (DV). All positions are relative to the centre of the decay volume.

Inside the spectrometer three apertures before and two after the decay volume were used for fine collimation of the beam and to avoid neutrons hitting the spectrometer walls. Details about the sizes and positions of all apertures are shown in table 5.1.

The two main apertures before the spectrometer were made from 5 mm thick sintered boron carbide (B_4C). This material is very hard and can be cut precisely with electro-erosion. The apertures consisted of a round piece of B_4C with a rectangular hole in the middle glued to a 50 mm thick lead piece with the same shape to shield the gamma rays produced by the boron. The inside of the lead was covered with 1 mm thick lithium loaded rubber, the backside with boron rubber to avoid scattered neutrons hitting the lead. To allow a minor adjustment of the apertures in the beam tube, the lead pieces had a smaller diameter than the beam tube and were clamped inside it with three screws. The bigger aperture in the middle was made from

boron rubber glued to an aluminium ring. This simpler design is sufficient as this aperture does not directly define the shape of the beam but only cuts away the neutrons with high divergency.

Boron (^{10}B) absorbs neutrons via an (n,α) reaction

$$^{10}\mathrm{B} + n \rightarrow ^{4}\mathrm{He} + ^{7}\mathrm{Li} + \gamma \tag{5.1}$$

with a very high absorption cross section for neutrons of $\sigma = 3835(9)$ barn [55]. Disadvantages of boron are that it produces gamma rays with an energy of 477.6(7) keV [56] and that most materials containing boron cannot be used in ultra high vacuum. Therefore we decided to use isotopically enriched lithium fluoride (^{6}LiF) where the production of gamma rays is suppressed by a factor of 10^{-4}:

$$^{6}\mathrm{Li} + n \rightarrow ^{4}\mathrm{He} + ^{3}\mathrm{H}. \tag{5.2}$$

Lithium's absorption cross section for neutrons is about four times lower than the one of boron, still it is high enough that a 2 mm thick plate of ^{6}LiF absorbs practically all neutrons. Another setback of lithium is the production of fast neutrons, but this effect is suppressed by a factor of 10^{-4} and our experiences from the first beam time at the FRM-II [32] showed us that fast neutrons are not critical for our experiment.

The ^{6}LiF was sintered into plates which were then cut into defined stripes and glued into rectangular tunnels of boron glass plates (thickness 8 mm). The boron glass helps to absorb scattered neutrons.

Finally the neutron beam exits the spectrometer through another magnesium-aluminium window into the beam stop. The beam stop is a sintered boron carbide plate at the end of a big vacuum vessel made from aluminium ($150 \times 50 \times 50\,\mathrm{cm}^3$). The side walls of this aluminium box are covered from the inside with boron loaded aluminium to absorb scattered neutrons. For the same reason a single aperture at the entrance of the beam stop was installed.

A ^{6}Li neutron counter with an efficiency of about $2 \cdot 10^{-6}$ was installed as a beam monitor behind the B_4C plate which had a hole in the middle to let some of the neutrons pass to the monitor. The neutrons that passed the monitor were stopped by boron loaded rubber. Outside the beam stop 10 cm

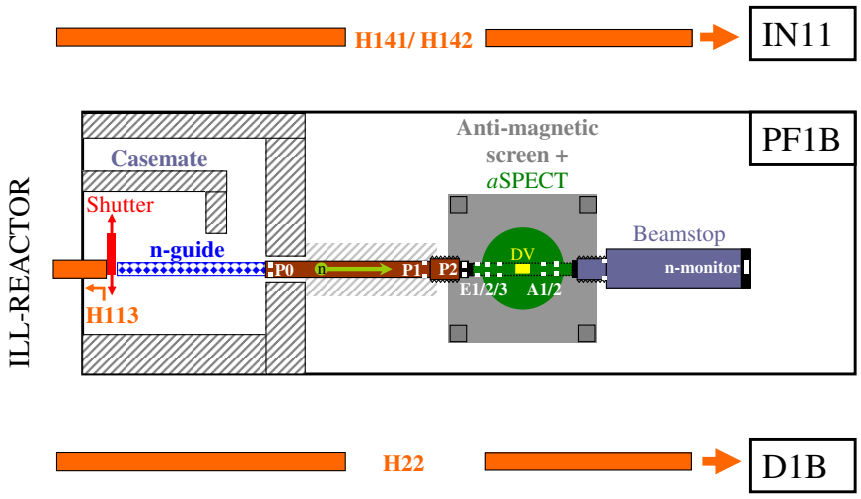

Figure 5.1: Schematic of the collimation system. Picture courtesy of M. Borg [54].

thick lead plates provided biological shielding of the gamma rays produced by the boron. The signals from the neutron counter were digitised into TTL[3] pulses and read with a National Instruments PCI-6602 interface.

To allow automated background measurements a B_4C shutter was installed inside the casemate, between the end of the H113 neutron guide and the entrance window of the vacuum tube containing the additional neutron guide and the collimation. The shutter was moved with pressurised air and operated with a 24 V control voltage which could be switched automatically by the control PC via an USB relay card[4]. To verify the position of the shutter and exclude the possibility of unwanted shutter movements during a measurement, end switches on both sides of the shutter were constantly monitored by the DAQ with the same PCI-6602 interface as the neutron counter.

[3]Transistor-transistor logic.
[4]Quancom USBREL8.

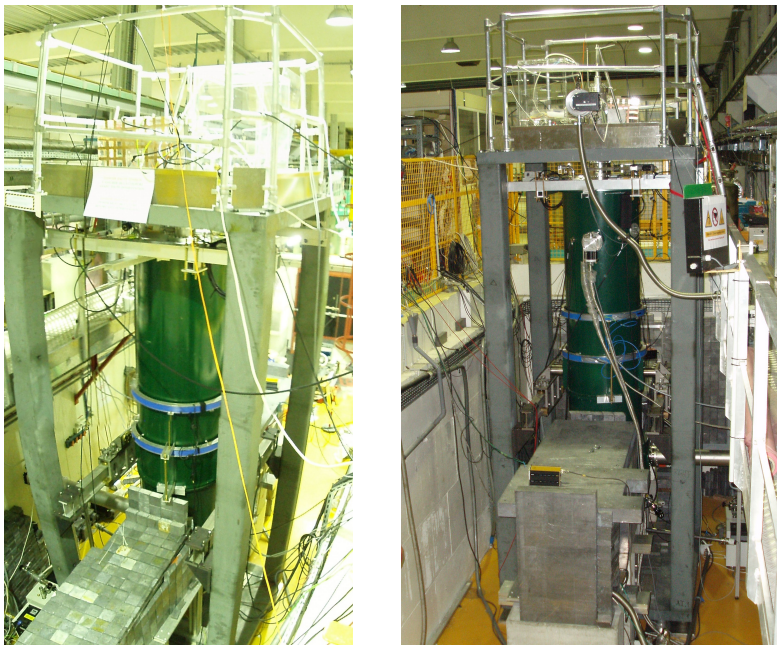

(a) entrance side (b) exit side

Figure 5.2: The *a*SPECT spectrometer at the ILL beam position PF1b.

5.1.2 Alignment of the spectrometer

During the measurement the neutron collimation system and the spectrometer have to be aligned precisely with respect to the neutron beam to optimise the number of neutrons going through the spectrometer, but also to minimise the edge effect and to avoid that the neutron beam hits the spectrometer walls. Because of the distance of about 5.5 m from the end of the H113 neutron guide to the decay volume, a misalignment of 0.1° would result in a displacement of the decay volume of about 1 cm with respect to the original direction of the neutron beam.

For the rough alignment a laser mounted in a predefined position[5] at the end of the experimental zone pointed to the centre of the exit window of the neutron guide. For fine alignment a theodolite behind the spectrometer was

[5]The position of the laser was already defined for a previous experiment by a neutron flight path measurement.

used. The theodolite was set up with the help of the laser and enabled us to check the positions of all important parts through the open beam ports of the spectrometer. After the beam tube and the additional neutron guide were aligned, the first two apertures, P0 and P1, were adjusted within the beam tube. The third aperture is installed right before the entrance window of the spectrometer and thus has to be aligned after the beam ports of the spectrometer are closed.

The spectrometer itself was adjusted by moving the entire anti-magnetic screen with the magnet in it on four air cushions. This procedure was necessary as the overall weight of the system is higher than the maximum load of the crane in the neutron guide hall. The height was adjusted by aluminium plates with different thicknesses under the feet of the bottom plate. Finally the internal apertures (E1 to A2) were aligned. Before the beam ports were closed with the magnesium windows an additional laser was placed in the centre of the additional neutron guide and pointed to the centre of the theodolite. With the help of this laser the last aperture P2 was aligned in front of the entrance window of the spectrometer.

Furthermore, the spectrometer had to be aligned within its anti-magnetic screen. Since there are high forces between the superconducting coils and the solid iron parts of the screen, a misalignment could lead to distortions of the magnetic field inside the spectrometer or, in the worst case, even break the holders of the coils. The magnet is fixed inside the iron screen with a support that allows a three dimensional movement of the magnet inside the screen [28]. During the adjustment, the fixations are opened and the magnet can freely move within a certain range in the xy-plane. The magnetic field is slowly ramped up and the magnetic centre can be identified by pushing the magnet around in the xy-plane. The magnetic centre is the point where the magnet does not move due to the magnetic forces. The best height was determined by lifting the magnet with the crane, with a hanging scale between the crane and the magnet, and again ramping up the field. The measured weight changes due to the magnetic force and the vertical magnetic centre can be identified.

It would be better to do this before the alignment to the neutron beam, as the position of the magnet and thus the internal apertures changes slightly. But the magnetic field can only be switched on if the magnet is cold, whereas the beam ports have to be open to align to the neutron beam. This would

mean cooling the magnet down and warming it up again. Unfortunately, this procedure takes at least ten days, which would have meant too much time loss in December 2007. However, the magnet was reopened in the break between the reactor cycles in January 2008 and the positions of the apertures were checked for the beam time in April and May 2008.

5.1.3 Neutron beam profiles

To verify the neutron beam profile, several copper foil activations were performed in front of the entrance window and behind the exit window of the spectrometer. Thin copper foils were irradiated with the neutron beam for about 80 minutes. The copper isotopes ^{63}Cu and ^{65}Cu are converted by neutron capture to ^{64}Cu and ^{66}Cu, respectively. ^{66}Cu is short lived ($\tau = 5.1\,\mathrm{min}$ [57]), whereas ^{64}Cu has a longer lifetime of $\tau = 12.7\,\mathrm{h}$ [58]. After waiting a sufficiently long time (about 1 to 2 hours), the activity of ^{66}Cu is very low and an almost pure ^{64}Cu beta decay can be detected. This method improves the accuracy and linearity of the measurement [59].

To detect the electrons emitted by the copper foils a silicon PIN-diode was mounted to a robotic arm 35 mm above the foil[6]. A lead shielding with a 3.5 mm diameter hole was used as a collimator between the detector and the foil. With this setup the foils were scanned in a grid pattern with 2.5 mm step and a size of 36×48 steps. Each point was measured for 5 s. After all points were scanned, the measurement was repeated in reversed scanning sequence until 6 full scans of each copper foil were performed. This provides a first order correction for the exponential decay of the intensity during the time needed for one scan ($\sim 2.5\,\mathrm{h}$). The overall spacial accuracy is about 1 mm, due to the uncertainties in the positioning of the foil in the beam line and the scanner.

For systematic studies of the edge effect, measurements with three different beam widths were performed. The beam size was reduced with an additional aperture in front of P2. From the resulting beam profiles before and after the spectrometer (fig. 5.3) the beam profile in the decay volume can be calculated (fig. 5.4). Further details on the beam profile measurements and the edge effect calculations may be found in [28, 54].

[6] Usually the copper foils are analysed with radiation sensitive image plates. Unfortunately, the image plate scanner was broken at the time of beam profile measurements.

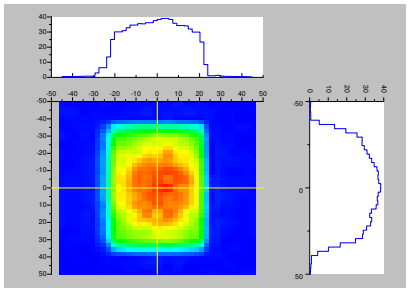

(a) Entrance side, full beam.

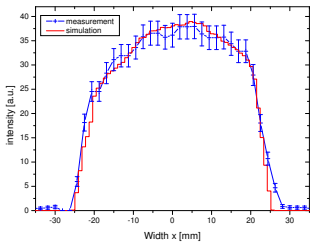

(b) Entrance side, full beam.

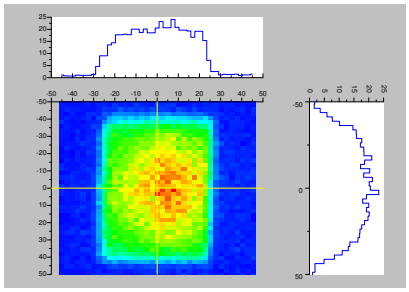

(c) Exit side, full beam.

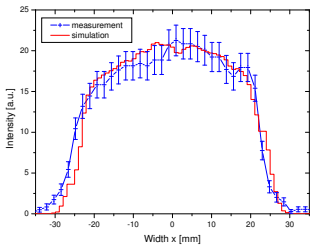

(d) Exit side, full beam.

Figure 5.3: Left side: Beam profiles measured before and after the spectrometer. Right side: Horizontal cut through the centre of the decay volume ($y = z = 0$) and comparison with simulated profiles.

The absolute neutron capture flux density after the exit flange of the spectrometer was $6 \cdot 10^9\,\mathrm{cm^{-2}s^{-1}}$. This was measured by a gold foil activation. The flux at the exit of the H113 neutron guide is about $2 \cdot 10^{10}\,\mathrm{cm^{-2}s^{-1}}$ [53][7].

5.1.4 Magnetic field measurements

The transmission function given in eq. (3.26) depends on the ratio of the magnetic fields in analysing plane and decay volume. Furthermore the transmission function can only be applied if the change of the magnetic field from the decay volume to the analysing plane stays within the adiabatic

[7] After changes in the in-pile part of the neutron guide the estimated flux given in this paper was verified by flux measurements.

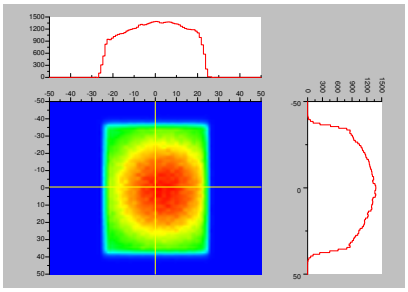

(a) Decay Volume, full beam.

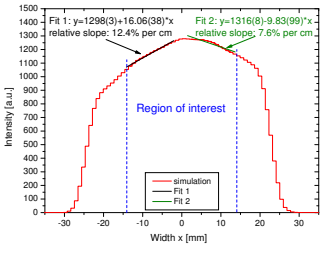

(b) Decay Volume, full beam, cut through $y = z = 0$.

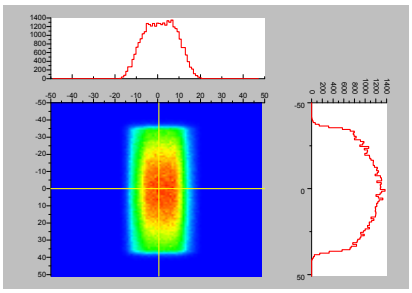

(c) Decay Volume, 20mm aperture.

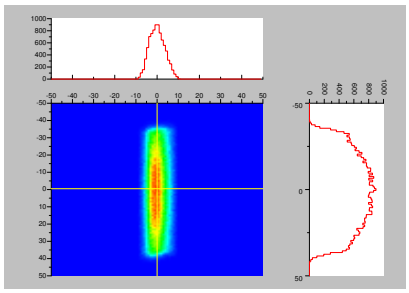

(d) Decay Volume, 5mm aperture.

Figure 5.4: Simulations of the beam profiles in the Decay Volume for three different beam widths. The parameters of the simulations were optimised to achieve the best possible agreement with the measured beam profiles outside the spectrometer (fig. 5.3).

limit.

The iron magnetic screen had to be dismantled for the transport and was reassembled at the beam position. To eliminate the possibility of an altered magnetic field ratio r_B due to a different contact between the pillars and plates of the iron screen or due to other surrounding magnetic materials the field was precisely measured during the reactor shut-down in winter 2008. Besides the determination of r_B, the long and short term stability as well as the reproducibility of the magnetic field were investigated. Furthermore, a field map for the calculation of proton and electron trajectories was measured.

Relative variation	longitudinal	radial
Decay volume	$9 \cdot 10^{-4}$	$5 \cdot 10^{-4}$
Analysing plane	$3 \cdot 10^{-4}$	$7 \cdot 10^{-4}$

Table 5.2: Relative variations of the magnetic field.

To measure the magnetic field the electrode system has to be removed from the main bore tube. It is replaced by a special, non-magnetic, hollow dewar. With this the central part of the bore stays at room temperature and the magnetic field can be measured with a hall probe[8]. A non-magnetic tube is fixed inside the dewar at the top, the bottom, and in the middle of the dewar. The hall probe just fits inside the tube and can be moved up and down with a long rod. The tube can be mounted in different positions on and off the axis of the spectrometer. With this setup a map of the magnetic field can be determined.

Preliminary results for the decay volume and the analysing plane are shown in fig. 5.5. For the resulting error bar on the magnetic field ratio the relative variation of the field is important:

$$G = \frac{B_{\max} - B_{\min}}{B_{\text{avg}}}, \tag{5.3}$$

where $B_{\max}$ is the maximal, $B_{\min}$ the minimal, and B_{avg} the average magnetic field. Both for decay volume and analysing plane there is a longitudinal and a radial gradient. The values are shown in table 5.2. These values lead to $r_{\text{B}} = 0.2030(1)$. The error bar is a worst case estimation. Several values were estimated in a conservative way, for example the decay volume was estimated to go from $z = -5\,\text{cm}$ to $+5\,\text{cm}$. For the longitudinal gradient in the analysing plane a difference of 5 cm between the maximum of the electric field and the local maximum of the magnetic field was used. Further details on the magnetic field measurements and their results can be found in [29].

Unfortunately, the magnet quenched during the beam time, due to an interruption in the cooling water supply. The compressors driving the cryo

[8] Group 3 technologies MPT141.

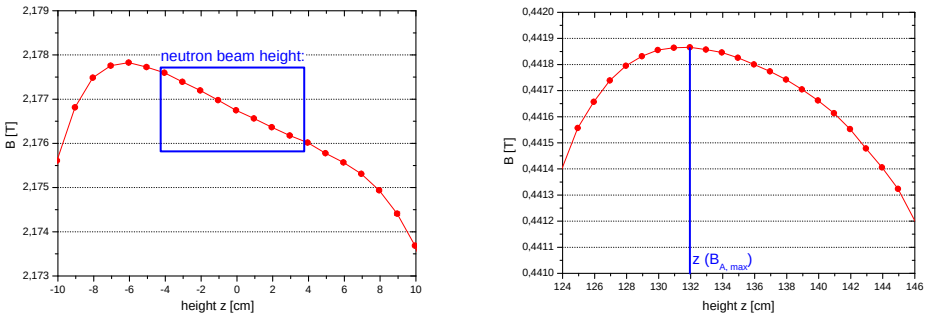

(a) Decay Volume. (b) Analysing plane.

Figure 5.5: The shape of the magnetic field on the axis of the spectrometer in the decay volume (a) and around the analysing plane (b).

coolers are water cooled. A safety mechanism switches them off if there is not enough cooling water to protect the compressors from overheating. This, of course, causes the magnet to warm up and, as soon as it goes above the superconducting edge temperature, the coils become normal conducting, and the current collapses due to the resistance. This effect is called quenching and heats up the magnet very fast and causes a fast heat expansion and possibly a movement of the coils. Due to this uncertainty we decided to measure the magnetic field again after the beam time. The measurements showed only minor differences compared to the measurements before, but the final analysis is not finished yet [29].

5.2 Data taking

5.2.1 Measurement process

The shape of the proton spectrum is measured by counting all protons that overcome a certain barrier potential in the analysing plane. After a rather short measurement time of about 10 to 180 s the barrier potential is altered. The measurement time is kept short to reduce trapping effects.

In the standard measurement mode seven different voltages in the ana-

lysing plane electrode are used. For the extraction of a measurements with only 50, 400, and 780 V would offer the best statistical sensitivity, but to gain a more precise knowledge of the shape of the spectrum and to learn about systematics effects 0, 50, 250, 400, 500, and 600 V are measured. At 780 V no proton can pass the analysing plane (AP) while electrons pass unaffected. These measurements are used to determine the background that has to be subtracted from the other measurements. To learn about systematic effects and to empty the potential trap between electrostatic mirror and analysing plane measurements with 0 V are performed. Usually, every fourth measurement was done with 780 V, followed by 0 V. In between were measurements with 50 V and one other voltage. Although measurements at 0 V offer the best counting statistics, the count rate might be altered due to low energetic ions from residual gas. Thus measurements with 50 V are used to normalise the count rates in the fit of a.

The voltage on the analysing plane is set by a HCN 0,8M-800 high voltage power supply manufactured by FUG. The exact voltage is read by a calibrated Agilent 3458A digital multimeter. Both devices can be controlled from a PC via GPIB[9] interfaces. The multimeter is read out twice per second and the measured voltage values are dumped into a logfile. The voltage is set by sending the desired value to the power supply and then reading the multimeter and correcting the set voltage in several loops. In total the ramping process takes about 30 to 40 s. First the voltage is ramped in 10 steps to about 97-99 % of the desired voltage within 8 s, followed by 5 s of waiting time during which the voltage is monitored with the multimeter. Afterwards the voltage is set to the desired value and the system waits until the difference of the voltage of the last and the last but one reading is less than 0.2 mV. After 2 s of waiting time the mean value of the voltage during 5 s is measured. With the help of this mean value a last fine correction of the votltage is done. A final 5 s waiting period allows some more stabilisation before the measurement is started. With this technique the applied voltage can be reproduced with very high precision. Evaluations of different data sets showed fluctuations of less than 1 mV during one measurement and a reproducibility of about 1 mV. These values are better than the absolute calibration of the multimeter and make the analysis much easier, as it is not necessary to use a special voltage for every single measurement in the fit of

[9] General Purpose Interface Bus.

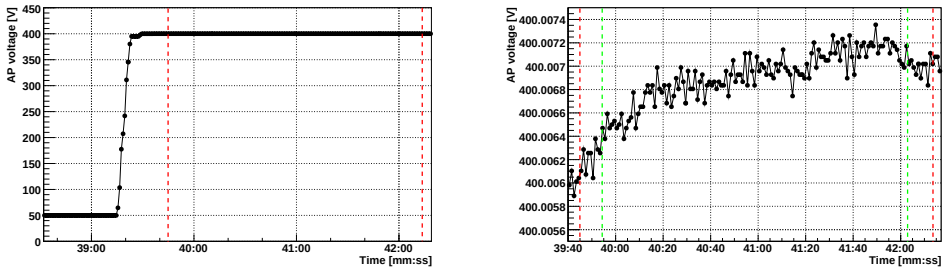

(a) (b)

Figure 5.6: An example for a ramping process (a) and the stability of the analysing plane voltage during a measurement (b). The red dashed lines denote the beginning and the end of the measurement, the green dashed lines the period during which the shutter was opened.

the integral proton spectrum, but it is possible to sum up all measurements with one voltage. A random example for a ramping process from 50 to 400 V is shown in fig. 5.6(a). The voltage monitored during the following measurement is shown in fig. 5.6(b).

After the ramping the next measurement is started. In the automated measurement mode, the single data files are assigned increasing numbers with the appendix `.dat`, starting with `-1.dat`. Due to technical reasons the analysing plane voltage is not ramped before the first measurement, thus it is assigned the number -1 and not taken into account during the analysis. The full measurement runs are typically at least several hours long, hence the time loss of one or two minutes due to this behaviour is negligible.

5.2.2 The instrument control setup

Besides the pure readout of the detector data, several voltages and other values have to be set and monitored during the measurements and the measurements have to be started and stopped.

For data taking and instrument control five personal computers were used:

- The **control PC** sets the voltage on the AP electrode, controls the movement of the neutron shutter, writes several log files, and gives

start and stop signals for the different operations done by the other PCs.

- The **DAQ PC** controls and reads the data from the sADC. See sect. 4.4.4 for details on the detector readout.

- The **data server** is used to store the data from the detector. The DAQ PC is connected to the data server via the network and the data is written directly to the hard drives of the data server.

- The **decode PC** decodes the data files immediately after each single measurement is finished. This task could as well be done by one of the other PCs, but an extra PC minimises unnecessary workload on the other PCs.

- The **magnet control PC** reads the temperature sensors of the magnet and is used to set and monitor the detector high voltage and the voltage of one side of the upper $\vec{E} \times \vec{B}$ electrodes. The power supply for the other side cannot be remotely controlled or read out.

The operating system of the control PC and the magnet control PC is Microsoft Windows XP. The data server runs under Suse Linux. The other PCs use a version of Debian Linux with some adaptions for the DAQ. For control and readout of the different devices several LabVIEW programs on the different computers are used. The communication between the different PCs is done via DataSocket, a standard developed by National Instruments which allows to transfer data values via the network. A DataSocket server is started on the DAQ PC and all variables that need to be shared between two or more computers are registered in the server application. Now any LabVIEW program in the network can publish and read the registered values via the server.

Details on the used programs can be found in app. A.2.

5.2.3 Neutron counter performance

To reach a high precision, the count rates of the proton detector have to be normalised to the number of neutrons passing through the decay volume. This number may fluctuate throughout the beamtime because of a changing

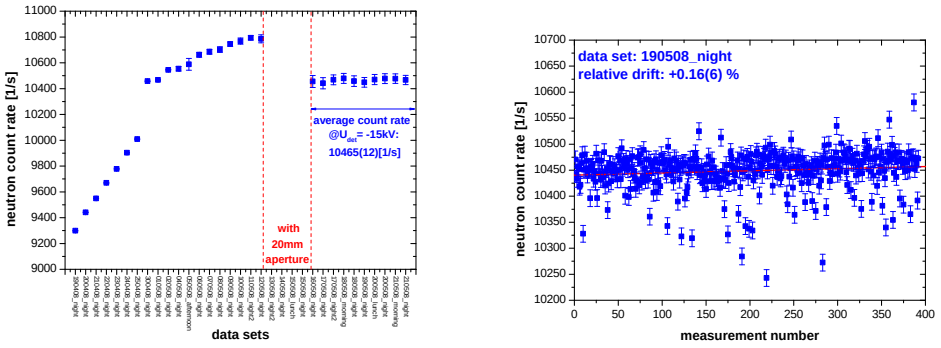

(a) (b)

Figure 5.7: a) The development of the neutron count rate over the beamtime. b) Stability of the neutron count rate over the night measurement run of May 19$^{\text{th}}$, 2008.

reactor power, changing conditions of the cold source or the instrument setup. For example, a well-known effect is a change of the neutron flux due to the control rod of the reactor. Throughout one reactor cycle the control rod is slowly extracted more and more from the core to keep the reactor power stable. Due to this movement the centre of the fission zone in the fuel element changes in height, whereas the position of the cold source remains the same. The normalisation can be done with the neutron counter installed in the beam dump.

Due to various problems with electrical connections the neutron counter did not run stable from the beginning of the data taking but showed a drift of +1.4 % per day, uncorrelated to the reactor power or any other changes. The drift is shown in fig. 5.7(a). The reason for it might be a bad grounding or an unstable reference voltage. The whole electrical setup was improved and the neutron count rate became more stable from May 16$^{\text{th}}$ on. However, close analysis still showed a small drift of +0.15% per day. Again, this drift cannont be matched with the course of the reactor power or other effects.

Besides the comparison of proton count rates from different measurement runs the neutron counter data can be used to reduce fluctuations in the proton count rates during one run, if those fluctuations are linked to

fluctuations of the neutron flux. As shown for a sample measurement run in fig. 5.7(b), the statistical error bar of the average neutron count rate for one measurement is typically about 0.1 to 0.15 %, the fluctuations are of the order of 1 to 2 %. Thus the fluctuations are non-statistical and should be used to correct the proton count rates, if the fluctuations show up there as well. In a close analysis of the neutron and proton count rates, no correlation between the fluctuations was found. For these reasons the neutron monitor was not used for the normalisation of the proton count rate.

5.3 Overview of the beamtime

The beamtime in December 2007 was mostly used to set up the spectrometer at the beam position, as described before. In the last week of the beamtime some measurements were performed, at first with the old silicon strip detector as it was used in the previous beamtime in Munich [32]. The new SDD was delivered shortly before the beamtime and the production of the new electronics could not be finished in time. As soon as the new detector and its electronics were ready, it was installed in the spectrometer for about one week of measurements. After opening the neutron beam, a slow but continuous drop of the count rate, especially at measurements with 50 and 250 V, was discovered. The maximum count rate was recovered after closing the beam for several hours.

This effect was caused by two ceramics rings which were located between the three parts of the decay volume[10] to keep them at a constant distance and centre them. Each of those rings had a smaller diameter than the cylindrical electrodes and was thus hit by the protons and electrons from the decay. This caused surface charges on the insulating material which created a barrier voltage for low energy protons.

The rings were removed just before the measurements on April 6$^{\text{th}}$, 2008. After the magnet was cold and ramped to a current of 70 A, the detector was inserted into the cryostat and the voltage slowly ramped up on April 16$^{\text{th}}$, 2008. The high voltage during the ramping process is depicted in fig. 5.8(a). Although no major breakdown occurred, the high voltage became unstable after it was ramped to 10 kV. After the voltage was reduced to 9 kV, where

[10] Electrodes e3 to e6 in fig. 3.4.

it was stable for about 15 minutes it was increased again. At about 11 kV again minor instabilities occurred and at 13 kV the ramping was stopped and the voltage was first reduced to 7.5 kV and then increased back to 10 kV. After a second attempt to go to a higher voltage with the same result, the voltage was ramped to 0 V and the detector was tested. Only the central pad was working. After the problem could not be solved with some tests of the accessible part of the electronics, it was decided to continue with this detector, as the central pad is the most important one. The high voltage was ramped to 9 kV without problems and left at that value during the night. The next morning it was increased to 10 kV without problems. In a later analysis of the logfiles of the high voltage and the leakage current, no breakdown of the voltage besides the minor instabilities was found, see fig. 5.8(b). However the leakage current shows two very high but short spikes during the ramping process. It is not clear if those spikes were real or if it is a malfunction of the readout soft- or hardware. The spikes in the logfiles are 20.8 and 26.6 μA high. The power supply has a current limit set to about 2 μA which should prevent such high leakage currents. Furthermore, the spikes in the logfile are only one measurement point long each. A measurement point is taken every 0.5 s, it is unlikely that such a high leakage current appears and disappears again so fast.

Thus most of the beamtime only data from the central detector pad is available. The outer pads would have allowed to perform additional systematic studies, like comparison of the count rate ratios on the different pads or particles from the electrode system being detected on one of the pads. On May 6^{th} the high voltage was ramped down to improve the cooling of the detector and make some changes to the electronics. The temperature readout of the detector was not working due to a wrong connection on the adapter board. After the high voltage was ramped up to 10 kV again, detector pad 1 (ADC channel 5) was working, but its resolution was not as good as the central pad's one. Unfortunately, after a few hours of measurements the first detector pad suddenly stopped working again for no obvious reason. For the rest of the beamtime again only the central pad was working.

Finally, on 15^{th} of May the high voltage was increased to 15 kV. It was kept at this value until the end of the beamtime.

In the beginning of the beamtime the values for a extracted in a preliminary analysis from the single measurement runs fluctuated non-statistically.

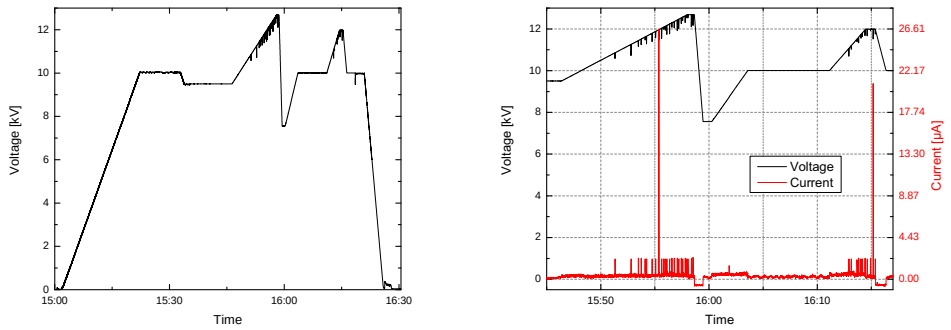

(a) (b)

Figure 5.8: a)The high voltage during the initial ramping process. The instabilities are clearly visible. b) Comparison of high voltage and leakage current during the attempts to ramp the voltage beyond 10 kV.

This behaviour was caused by several problems which were solved throughout the beamtime. A power supply for one side of the lower $\vec{E} \times \vec{B}$ electrodes was replaced because it was unstable, several ground loops were removed, and the connections of the electrode system were improved. Therefore the data analysis mostly focussed on data taken in the last weeks of the beamtime, from 13^{th} to 23^{rd} of May 2008.

During the beamtime many systematic effects were investigated. The most important measurements were:

Beam profile. As already explained in sect. 5.1.3, three different widths of the beam were used to investigate the edge effect (sect. 3.4.6).

Mirror off. The electrostatic mirror was switched off and the count rates with and without mirror were compared. This ratio allows to check the shape of the magnetic field inside the decay volume. To avoid a possible trapping of protons inside the decay volume, the magnetic field is not entirely constant but has a slope with the maximum below the decay volume. This creates a small magnetic mirror which ensures that the decay particles can leave the decay volume. This is also the reason why about 51 % of the protons go directly towards the detector

and only 49 % towards the mirror. This number was confirmed by the measurements during the beamtime.

Lower ExB settings. To investigate trapping effects between analysing plane and electrostatic mirror, the $\vec{E} \times \vec{B}$ drift potential was reduced from the standard setting of $U_{\mathrm{E\times B,1}} \,|\, U_{\mathrm{E\times B,2}} = -1000\,\mathrm{V} \,|\, -50\,\mathrm{V}$ on the two half cylinders of the electrode in several steps down to $-2.5\,\mathrm{V} \,|\, 0\,\mathrm{V}$. The analysing plane was set to 780 V and the neutron shutter was opened and closed during the measurements.

Decay volume gradient. Over the three parts of the decay volume electrode a gradient voltage was applied. A difference in the count rate compared to the normal count rate would point to a trapping of protons inside the decay volume.

Second analysing plane. To investigate possible background contributions due to the electrons, the lower $\vec{E} \times \vec{B}$ electrodes were used as a second analysing plane. Both sides were set to the same value, from +100 up to +1000 V, to block part or all of the protons.

Acceleration voltage. Two different acceleration voltages were used during the beamtime (10 and 15 kV) in order to search for a possible influence on a.

Magnetic field ratio. The ratio of the magnetic fields in analysing plane and decay volume r_{B} was changed with the external Helmholtz coils. A coil current of 50 A changes r_{B} by about 1 %, from the normal value of $r_{\mathrm{B}} = 0.2030$ to $r_{\mathrm{B}} = 0.2049$.

Main magnetic field. The strength of the magnetic field determines the gyration radii of the particles in the spectrometer and thus changes the edge effect. Furthermore the the non-adiabatic proton motion becomes stronger. At the end of the beamtime a measurement run was done with 30 A coil current instead of the standard setting of 70 A.

6 Data analysis

The following section gives detailed information about the analysis of the data taken during the beamtime at the ILL. The analysis was mostly done by Michael Borg [54] and me. To avoid a biased analysis the values of a used during the process of the analysis were altered in the following form:

$$a_{\text{cheat}} = a \cdot v_1 + v_2, \tag{6.1}$$

where v_1 and v_2 were chosen in a way that the influence on the error bar of a is rather small. The values were only known to two people not directly involved in the analysis. Thus it was impossible for us to push the value of a towards or away from previously measured values, neither willingly nor subconsciously. Only after the analysis was completed the values were revealed to be $v_1 = 1.2477$ and $v_2 = 0.0008$. The values of a given in the following chapter have been corrected according to eq. (6.1) after the end of the analysis.

Unless otherwise stated all presented plots and examples are from data with an acceleration voltage of 15 kV.

6.1 Fitting of the pulses

6.1.1 The pulse function

As explained in sect. 4.4.2, for every trigger a sequence of ADC values with predefined length (usually 100 bins $\hat{=}$ 5 μs) is written to the PC. This sequence is called one event (see fig. 6.1).

To extract the spectrum for one measurement run, the pulse-height of each event has to be determined. The simplest way to do this is to take

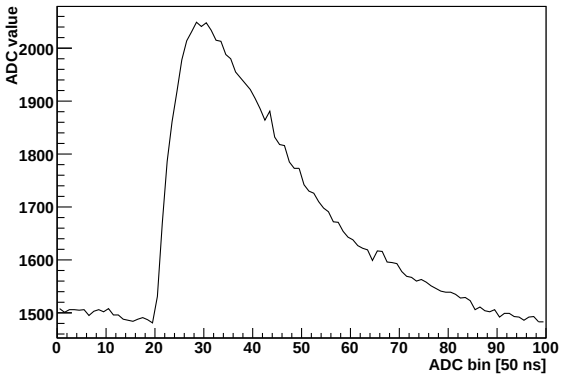

Figure 6.1: A typical proton event (event 2345 from may 19, 2008/night, file 5).

the maximum of each event and subtract a fixed baseline[1], but this method is insensitive to possible baseline fluctuations. Calculating the baseline separately for each event from the first 15 bins avoids this problem. Still, one cannot be sure if the highest point of the event is really the maximum of the pulse or a spike from the electronic noise.

The shape of the pulse can be described as a mathematical function with 5 parameters:

$$y_{\mathrm{Fit}}(x) = \begin{cases} y_0 & ;\ x \leq x_0 \\ y_0 + A\left(1 - e^{-\frac{x-x_0}{t_1}}\right)^p e^{-\frac{x-x_0}{t_2}} & ;\ x > x_0 \end{cases} , \tag{6.2}$$

where y_0 is the baseline of the pulse. x_0 is the start point of the pulse, t_1 and t_2 denote the rise and decay time of the pulse, respectively. p influences the shape of the pulse and A the height of the pulse. t_1, t_2, and p are given by the electronics, thus they are fixed when the function is used for fitting our pulses. x_0 depends on the settings of the trigger algorithm and, due to the principle of the trigger, also slightly on the height. Therefore it is not fully fixed in the fitting routine, but only restricted to a certain range (13 to 23.5). The baseline y_0 is restricted in the fit to ADC values from 800 to 2000. A, which is proportional to the height of the pulse, can take positive

[1]The result of this method is called h_{nf} in the following.

values only. Table 6.1 shows the exact limits of the fit parameters. From the parameters, the fitted pulse-height h_{fit} is determined as the analytical maximum of eq. (6.2).

Parameter	**Lower limit**	**Upper limit**
y_0	800	2000
x_0	13	23.5
t_1	77.49 (fixed)	
t_2	10.47 (fixed)	
p	0.394 (fixed)	
A	1	$2 \cdot 10^5$

Table 6.1: Limits of the used fit parameters.

The pulse is only fitted from ADC bin 10 to 40. This significantly reduces the computing power and thus the time needed for each fit.

6.1.2 Event types

According to the result of the fit, the events are classified as different types. Only events without ADC values above 3500 before bin 30 are fitted, the others are assigned status 3. Because the high energetic electrons and gammas are cut off by the maximum amplification of the electronics, the exact pulse-height of these events cannot be reproduced by the fit. Events where the fit did not converge are assigned status 4, events with converging fits are classified according to their pulse-height and the χ^2 of the fit. Events with $\chi^2/(h_{\text{fit}} \cdot NDF) < 0.00741$, where NDF is the number of degrees of freedom of the fit, are status 0. Examples for states 0 and 3 are shown in fig. 6.2. If the fit result has a bad χ^2 (e.g., $\chi^2/(h_{\text{fit}} \cdot NDF) \geq 0.00741$) the event is classified according to its pulse-height: noise events ($h_{\text{fit}} < 80$) are status 2 (fig. 6.5), the other events are status 1 (fig. 6.3). A scatter plot of the distribution of $\chi^2/(h_{\text{fit}} \cdot NDF)$ for one measured file is shown in fig. 6.4. Events with status 1 are separated from those with status 0. There is no clear separation of states 0 and 2, but these events are in the pulse-height region of the noise and thus are not considered for the further analysis. The limits have been chosen manually to get the best possible separation of

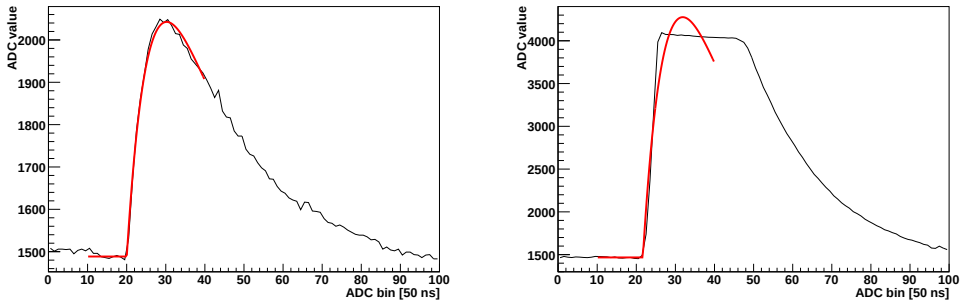

(a) (b)

Figure 6.2: (a) The same event as in fig. 6.1 with the resulting fit (red line): $x_0 = 20.0(1)$, $y_0 = 1489(6)$, and $A = 29040(455)$. The pulse-height from the fit is $h_{\mathrm{fit}} = 554.0$ compared to $h_{\mathrm{nf}} = 549.8$ from the maximum−baseline method. (b) A high energetic electron or gamma which is cut off due to the limited maximum amplification of the electronics. In the normal analysis these events are not fitted as the routine gives nonsensical results due to the different shape of the pulse.

good and bad events. The error for the value of each ADC bin of an event is fixed to 20, thus the usual relation of $\chi^2/NDF \approx 1$ as argument for a good quality of the fit is not valid in our case.

Pulses with status 4 (fit not converged) are fitted again with the improved fit routine of ROOT and, if the fit still does not converge, the pulse is rebinned to even out short spikes in the electronic noise and fitted again. With this technique practically all events can be fitted. The improved fit routine of ROOT uses the integral values of the fit function instead of the value at the centre of the bin. This method gives more precise results but needs more computing time.

Examples for events with status 1 and 2 are shown in fig. 6.3 and fig. 6.5, respectively. An overview of the different fit states is given in table 6.2.

6.1.3 Incorrectly sorted events

Unfortunately not all events are sorted correctly by the standard fit routine. Especially in two cases events are sorted as status one or two, although they

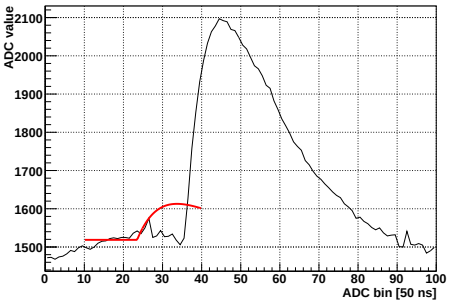

(a) event 3045: $h_{\mathrm{fit}} = 94.1$, $h_{\mathrm{nf}} = 594.6$.

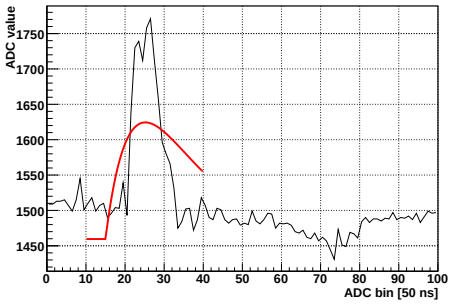

(b) event 9779: $h_{\mathrm{fit}} = 164.8$, $h_{\mathrm{nf}} = 260.9$.

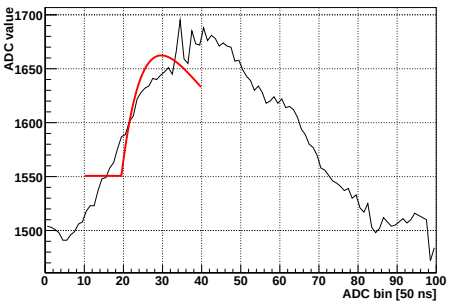

(c) event 10073: $h_{\mathrm{fit}} = 111.7$, $h_{\mathrm{nf}} = 182.3$.

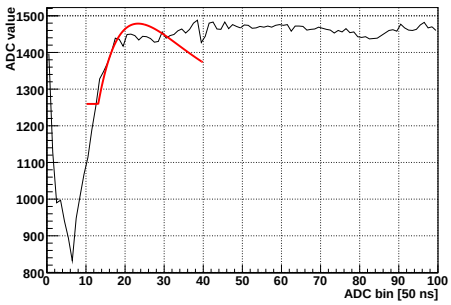

(d) event 16866: $h_{\mathrm{fit}} = 219.0$, $h_{\mathrm{nf}} = 394.1$.

Figure 6.3: Events with fit status 1, from 17_05_08/night2, file 5. (a) shows an event where the trigger was caused by electronic noise followed by a proton shorty after. These events have to be sorted out to keep the dead time correction simple. (b) to (d) show different examples of unwanted events.

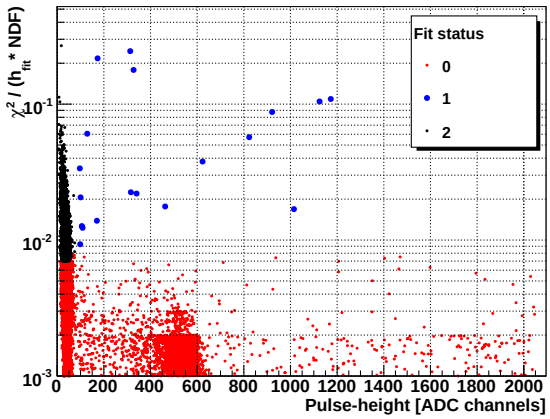

Figure 6.4: Distribution of $\chi^2/(h_{\mathrm{fit}} \cdot NDF)$ versus the pulse-height. The different colours show the different fit states for a file with 50 V in the analysing plane (19_05_08/night, file 5).

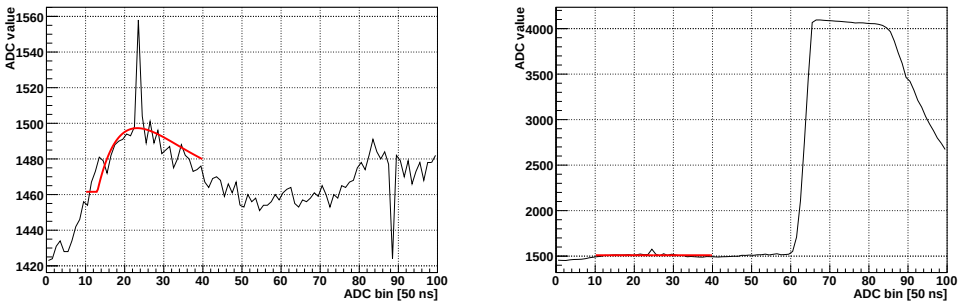

(a) event 297: $h_{\mathrm{fit}} = 35.7$, $h_{\mathrm{nf}} = 108.1$. (b) event 9783: $h_{\mathrm{fit}} = 2612.7$, $h_{\mathrm{nf}} = 0.02$.

Figure 6.5: Events with fit status 2, from 17_05_08/night2, file 5. (a) shows some normal noise, (b) noise followed by an electron.

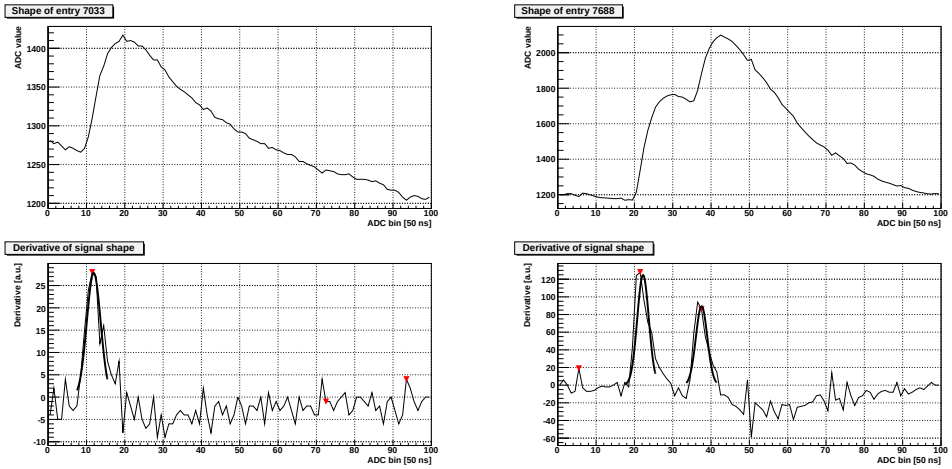

(a) event 7033.

(b) event 7688.

Figure 6.6: Top: Events from 17_05_08/night2, file 5. These events were incorrectly sorted into fit status 1. Bottom: To separate these events from unwanted noise events the derivative of the event is investigated. The peak candidates found by the peak finding algorithm are shown as red triangles, the thick black line is showing the Gaussian fits to the relevant peak candidates.

are valid proton events:

1. **Pile-up:** When a second proton is detected shortly after the triggering one the fit does not work, as the shape of the signal is altered by the rising edge of the second proton. Since the standard fit goes from bin 10 to bin 40 this happens when the second proton peak starts before bin 40 in the recoded event window. Fig. 6.6(b) (top) shows such an event.

2. **Proton after electron:** The falling edge of high energetic electrons is longer than the length of one ADC event. Thus, if a proton follows shortly after such an electron it is on the exponentially decaying edge of the electron (see fig. 6.6(a) (top)).

To identify and separate these events from the correctly sorted ones the derivative of the event shape is calculated. This means, a new histogram

is created from the ADC values $h(i)$ of the event shape histogram with the derived values $d(i)$:

$$d(i) = h(i) - h(i-1). \tag{6.3}$$

Two examples are shown in fig. 6.6. The steep rise of the signals causes distinct peaks in the derivative. From the number and position of those peaks the two above mentioned cases can be identified. Pile-up events cause two peaks in the derivative, the first one around bin 23, the second one between bin 25 and 40. Protons after electrons are triggered later than normal events, thus these events show one single peak at low bin numbers (below bin 14).

To automise the process, the `TSpectrum::Search` peak finding routine is used. This function is implemented in the ROOT data analysis framework and is based on the Markov chain algorithm [60]. It returns the position of possible peaks in the derivative. Between bin 5 and 45 the algorithm returns one or two peak candidates, only those are used for further investigation. Although the exact shape of the derivative follows a quite complicated function (the derivative of eq. (6.2) superimposed by the electronic noise), a simple Gaussian fit can be used to get the needed information about the peak:

$$G(x) = m_{\mathrm{G}} e^{-\frac{1}{2}\left(\frac{x-x_{\mathrm{G}}}{\sigma_{\mathrm{G}}}\right)^2}, \tag{6.4}$$

where m_{G} is the maximum of the peak, x_{G} the centre, and σ_{G} the width.

The event is classified as a pile-up, if there are two peaks, the first peak is behind bin 10, both peaks have heights bigger than 10, and a width between 0.5 and 4 bins. In this case the pulse is fitted with the standard fit function eq. (6.2), but with different limits of the fit. The fit now starts at bin 5 and ends at the position of the second Gaussian peak x_{G2} minus the width σ_{G2} of the peak:

$$x_{\mathrm{end}} = x_{\mathrm{G2}} - \sigma_{\mathrm{G2}}. \tag{6.5}$$

This method works to time differences of the two pile-up events down to about $0.25\,\mu$s (fig. 6.7). A comparison of the result of the standard fit and the adapted fit is given in fig. 6.8(b).

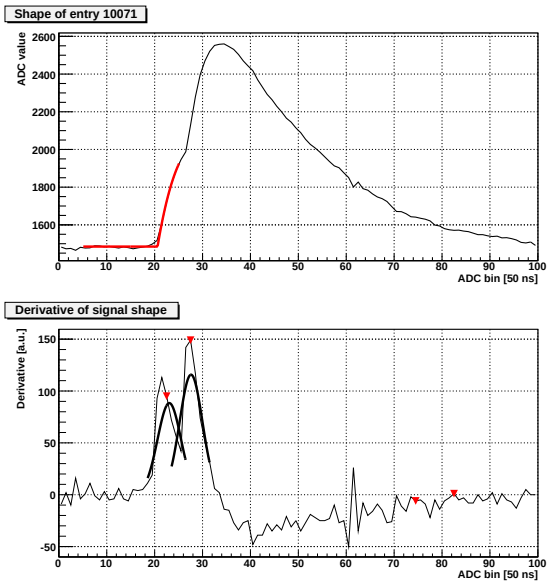

Figure 6.7: An example for a pile-up event with a very short time difference of only about 4.5 bins $\hat{=}$ 225 ns (event 10071 from 17_05_08/night2, file 9). In the derivative the two peaks can still be clearly separated and reasonable limits for the fit can be set. Although only the rising part of the event is fitted, the result gives a reasonable pulse-height of 572.5 for the first proton.

A proton after an electron is identified via a Gaussian peak in the derivative before bin 13.5, with a height bigger than 10, and a width of at least 0.8 bins. A special fit function is used to fit those events:

$$y_{\mathrm{PaE}}(x) = y_{\mathrm{Fit}} + e^{x_1 + p_1 x} - 1, \tag{6.6}$$

where y_{Fit} is the standard fit function eq. (6.2). x_1 and p_1 are the Parameters of the additional exponential decay. The event is now fitted from bin 1 to 35 to get a more precise knowledge of the changing baseline. A comparison of the result of the standard fit and the adapted fit is given in fig. 6.8(a). The pulse-height of the event is then calculated from the parameters of the standard fit y_{Fit}, this means the pulse-height the event would have if it was sitting on a flat baseline is used for the further analysis.

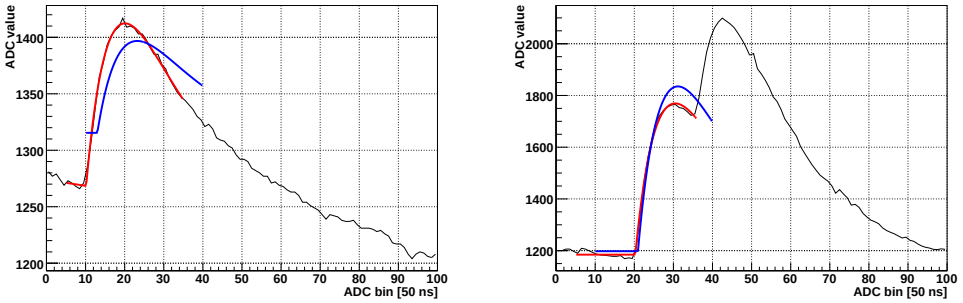

(a) event 7033: $h_{\mathrm{fit}} = 151.5$, $h_{\mathrm{nf}} = 115.9$. (b) event 7688: $h_{\mathrm{fit}} = 584.8$, $h_{\mathrm{nf}} = 906.2$.

Figure 6.8: Events with fit status 5, from 17_05_08/night2, file 5. The results of the standard fit and the adapted fit are shown in blue and red, respectively.

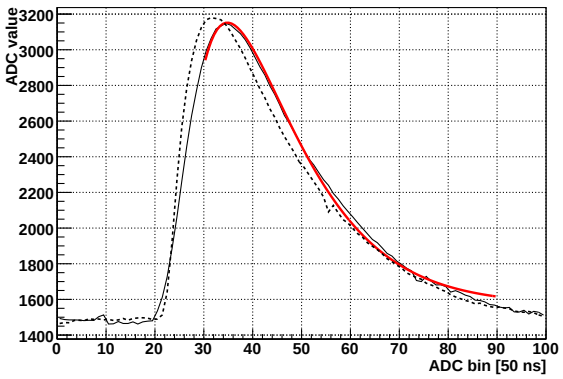

Figure 6.9: An example for a status 7 event. Event 3782 from file 5 in run 17_05_08/night2 (solid black line) with the adapted fit (solid red line). A normal event, number 2831 from the same file, is drawn for comparison (dashed black line).

After the above procedure, there are still some proton events with status 1. These have a slightly different shape in the rising part of the pulse, the rising edge is not as steep as for the normal events and the maximum of the pulse is shifted to higher time bins. These events are treated with the same fit as the other events, but instead of fitting mostly the rising edge of the pulse, like the standard bin 10 to 40 method does, the fit focuses on the falling edge of the pulse from bin 30 to 90. Furthermore the x_0-restriction is now widened from bin 13 to bin 25. If the χ^2-condition given in sect. 6.1.2 is fulfilled the event is assigned status 7. An example for such an event is shown in fig. 6.9.

Fig. 6.10 shows a comparison of fitted and non-fitted spectra. The separation of noise and proton peak is much better in the fitted spectra. Table 6.2 shows an overview of the different fit states.

The results of the fit are written to a ROOT tree for further analysis, the detailed structure of the tree is described in app. A.3.2.

Status	**Description**
0	normal events with good χ^2 ($\chi^2/(h_{\text{fit}} \cdot NDF) < 0.00741$)
1	events with bad χ^2 and $h_{\text{fit}} \geq 80$
2	events with bad χ^2 and $h_{\text{fit}} < 80$
3	high energy events
4	fit failed
5	refitted status 1 events
6	refitted status 2 events
7	events with different shape

Table 6.2: Overview of the different fit states.

6.2 Extraction of the correlation coefficient

After the fitting of the pulses, the value for a has to be extracted from the proton spectra. First, the count rate of each measurement has to be corrected for the dead time of the electronics. Then the background has to be subtracted and the count rate has to be extracted by integration over the pulse-height histograms. Finally different corrections have to be applied.

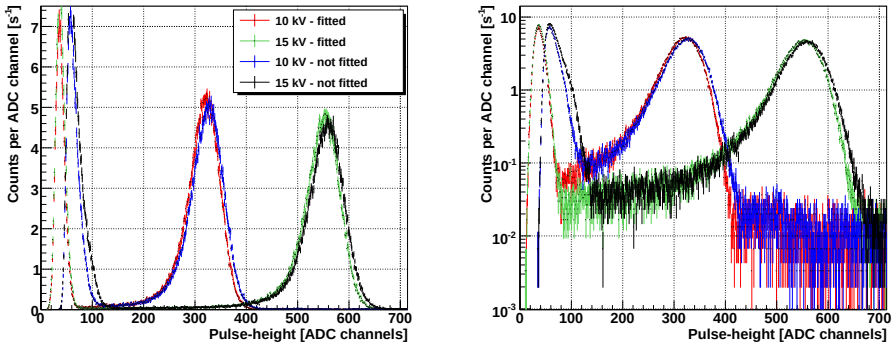

(a) (b)

Figure 6.10: Spectra from 15_05_08/rampHV for 10 and 15 kV acceleration voltage in linear (a) and logarithmic (b) depiction. For each acceleration voltage the electronic noise peak (left peak) is much lower for the spectra from the fitted pulses, whereas the proton peak (right peak) stays almost the same. The slightly lower right edges of the proton peaks from fitted pulses can be explained with the statistical noise on the signals: The fit evens out spikes from the thermal noise. For the non-fitted spectra a positive noise spike at the maximum of the pulse increases the calculated height of the pulse significantly. In the opposite case, a negative spike will only have a minor influence on the height of the pulse, as the maximum of the pulse will then be in one of the bins next to the negative spike.

6.2.1 Dead time correction

Every event has a length of $5\,\mu$s, during this time no other event can be registered[2]. Due to the nature of the trigger the next event has a minimum time difference of $5.2\,\mu$s. This defines a "non-extendable" [61] dead time which causes a reduction of the count rate which depends on the absolute count rate:

$$C_{\mathrm{corr}} = \frac{C_{\mathrm{meas}}}{1 - C_{\mathrm{total}} \cdot T_{\mathrm{dead}}}, \tag{6.7}$$

where $T_{\mathrm{dead}} = 5.2\,\mu$s is the dead time per event. C_{corr} and C_{total} are the corrected and the total measured count rate, respectively. C_{meas} is the measured count rate in the region of interest. Due to the rather high count rate on one detector pad, the dead time correction has a rather strong impact on the result for a. For example, for a count rate similar to the proton count rate at $U_{\mathrm{A}} = 0\,\mathrm{V}$ of $C_{\mathrm{meas}} = C_{\mathrm{total}} = 500.0(5)\mathrm{s}^{-1}$ the count rate loss would be $\approx 1.3(5)\mathrm{s}^{-1}$, causing a shift of a of 3.5 %. This shift can be corrected very well, as long as the dead time is precisely known. Taking a dead time of $6.0\,\mu$s instead of the true $5.2\,\mu$s would cause a systematic error of $\frac{\Delta a}{a} = 0.2\,\%$.

6.2.2 Background subtraction

The background is measured by applying 780 V in the analysing plane. It has to be subtracted from the measurements with lower analysing plane voltage to obtain the pure proton count rates. The principle is shown in fig. 6.11. There are two possible strategies to do so:

1. For each single measurement the count rate of the closest background measurement in time is subtracted.

2. The count rate averages for every voltage are calculated by summing up all measurements with the respective voltage. Then the average background count rate is subtracted.

[2]The fit routine ensures, that in the case of a pile-up of two protons only the first one is counted, see fig. 6.7.

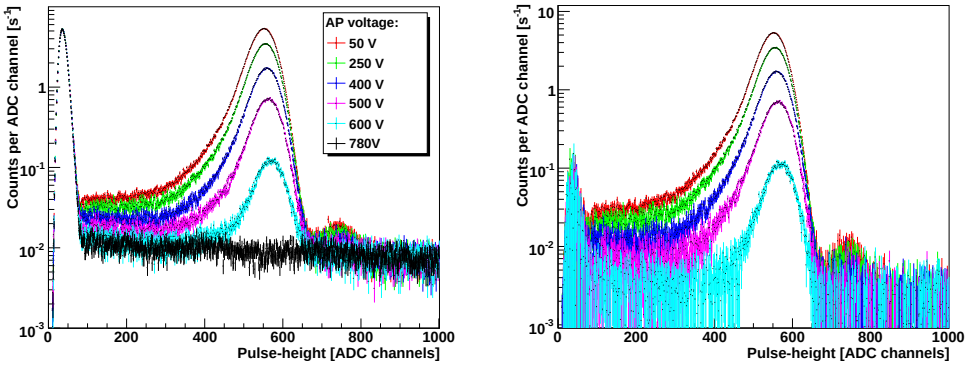

(a) (b)

Figure 6.11: Subtraction of the background: (a) shows the sums of all measurements for each measured voltage in the analysing plane from 19_05_08/night. (b) The 780 V measurement is subtracted from the other measurements to obtain the pure proton spectra.

The first option has the advantage of a correction of short term fluctuations in the count rate. However, it is difficult to avoid introducing a systematic effect. If some background measurements are used more often than others, the errors become correlated and different weighting of the measurements would be necessary. Although the background is measured in a regular pattern in every fourth file, some measurements had to be excluded because of malfunctions of the data taking system. Furthermore, in a detailed analysis of the background (see sect. 6.3) no short term fluctuations in the background count rate were found. Because of these two reasons, the second method (subtraction of averages) was chosen for the analysis.

6.2.3 Integration of the count rate

The shapes of the spectra in fig. 6.11(a) are the result of a combination of several components. On the far left side, at pulse-heights below 100, the noise of the electronics is visible. Usually the trigger settings are chosen in a way that some noise is recorded to be able to perform studies on changes

of the noise, see sect. 6.6.

The electrons form a broad, almost constant distribution over the entire visible part of the spectra. They are best visible in the 780 V spectrum, as there are no protons. The protons form the peaks around 550 ADC channels. The asymmetry is caused by the energy loss in the dead layer, as explained in sect. 4.5. The positions of the proton peaks depend slightly on the analysing plane voltage. The maxima are 552 ADC channels for 50 V, 559 ADC channels for 400 V, and 567 ADC channels for 600 V. This is because only protons with sufficient energy can pass the analysing plane and the higher the voltage, the higher is this energy. The resolution of the detector is high enough that the width of the proton energy distribution is a visible contribution to the total width of the peak. The other main contributions to the peak width are the energy straggling in the dead layer and the electronic noise.

The small peak at about 750 ADC channels was not expected and has been carefully investigated. The pulse shapes in that peak look like ordinary events, also the count rate behaves exactly like in the main peak. During the detector tests with a proton beam, a dependence of the peak position on the position of the aperture was found, thus the probable reason for the extra peak is a slightly higher amplification on a small spot of the detector. The counts in the extra peak were included in the further analysis.

To extract the count rates for each analysing plane voltage from the background-subtracted spectra in fig. 6.11(b), they have to be integrated, this means the sum of the counts of all ADC channels within certain limits is calculated. Usually the lower limit is set as close as possible to the noise at ADC channel 80, the upper limit is set well above the proton peak at channel 1200.

With the integration a single data point for every measured voltage is retrieved. For the standard measurement settings we obtain 6 data points which can be plotted as a function of the voltage, see fig. 6.12. The final step is then a fit to the integral of the proton spectrum described in eq. (2.33):

$$\rho_{\mathrm{tr}}(U_{\mathrm{A}}) = N_0 \int dT_0 F_{\mathrm{tr}}(T_0, U_{\mathrm{A}})(g_1(T_0) + a g_2(T_0)). \tag{6.8}$$

The fit parameters are the count rate at 0 V N_0 and of course a. The

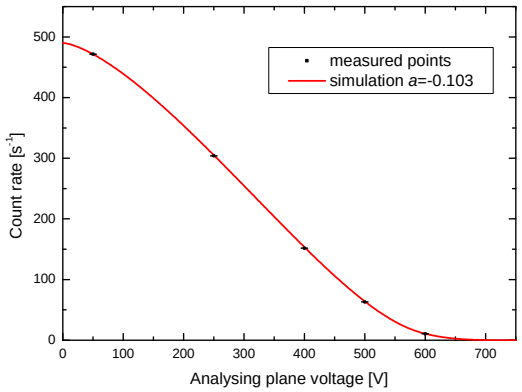

Figure 6.12: The integral proton spectrum. The proton count rates after the integration of the spectra are plotted against the analysing plane voltage, these points are then fitted to obtain a. For comparison a simulation of the integral proton spectrum for $a = -0.103$ is plotted. The horizontal lines indicate the data points. The error bars are smaller than the data points.

measurements with 0 V analysing plane voltage are not used for the fit of a, thus N_0 is a free parameter in the fit.

6.2.4 Dependence on the integration limits

In the following sections values of a are given. These values are only corrected for the cheat of the blind analysis and the dead time. Thus they do not represent a real, final value of a but they are only given for comparative reasons. Several corrections (e.g., for the edge effect) still have to be done to obtain a final value.

During the analysis the integration limits were varied and a dependence of the value for a on the lower integration limit was found. As can be seen in the black curve in fig. 6.13, the value for a is -0.094(3) for a lower integration limit of 80 ADC channels. The value then drops to -0.103(3) for a lower limit of 340 ADC channels. For even higher integration limits

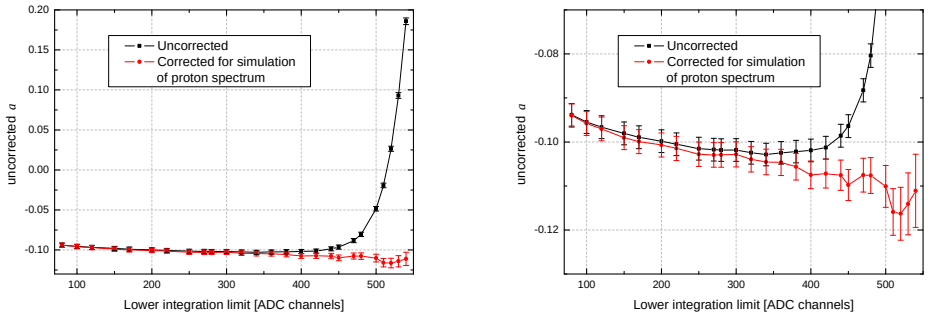

(a) Full picture.

(b) Zoom.

Figure 6.13: Dependence of a on the lower integration limit in the run 16_05_08/night. The left picture shows the full range of applied integration limits, the right one a zoom for values around $a = -0.1$ for better visibility of the drift. The error bars are purely statistical and, as it is the same measurement run for all integration limits, strongly correlated. The lines between the points are to guide the eye.

the value rises steeply to positive numbers.

The rise for high limits can be explained with the retardation principle that is used by aSPECT. As mentioned before, the analysing plane cuts away the low energy part of the spectrum, thus, for a fixed integration limit for all voltages, one cuts away more counts for the lower voltages than for the higher ones. This is visible in fig. 6.11(b), an integration limit of 400 ADC channels cuts away a considerable part of the 50 V measurement, whereas only a small fraction is cut away from the 600 V measurement. The proton simulations described in sect. 4.5 describe this effect correctly and the measured count rates can be corrected by the simulations. For each integration limit and analysing plane voltage, the simulated spectrum is scaled to give the same count rate as the measured one above the integration limit. The count rate expected by the simulations below the integration limit is added to the measured count rate above the limit. The resulting count rate is then used to fit a. The results are plotted in red in fig. 6.13. The strong increase at high limits disappears in the corrected values. However, the slope at lower limits persists. It is obviously caused by a different systematic effect.

For the general analysis the integration limit should be chosen as close to the noise as possible to minimise the needed correction on a. For a lower integration limit of 80 ADC channels, the correction is only $\Delta a = 0.13(9)\,\%$.The error bar is dominated by the statistics of the proton simulations and thus can be lowered by simulating more protons.

This systematic test was also performed for the upper integration limit by fixing the lower and varying the upper limit. No dependence of a on the upper integration limit was found, even if the limit is below the extra peak visible in fig. 6.11.

6.3 Background

In the beamtime with aSPECT at the FRM-II fluctuations in the background count rate turned out to be the major problem in the data analysis and prevented us from giving a value for a. Several changes were made in the spectrometer to improve the background conditions[3].

One of the most important improvements was the installation of an automatic neutron shutter. Although this does not directly improve the background conditions, it opens the possibility to study the background shortly after measurements with neutron beam.

6.3.1 Automated shutter movements

During the last days of the beamtime a new method to operate the neutron shutter was implemented, allowing to open and close it during a running measurement. In the previous method the measurement was stopped and a new one started. The sADC needed about 7 s to be initialised before each measurement, shutter movement and computing need some time as well, thus fast decaying background cannot be seen in the mode with separate measurements. In the new mode, the measurement is divided into the five shutter states shown in table 6.3. The shutter states were defined by the states of the end switches: For 2 and 4, both end switches were open, for the others one was closed.

[3] See sect. 3.4.4.

Shutter status	Description
1	Shutter is closed for measurement of the background.
2	Shutter is opening.
3	Shutter is open, normal measurement with beam.
4	Shutter is closing.
5	Shutter is closed, measuring the background again.

Table 6.3: The different shutter states.

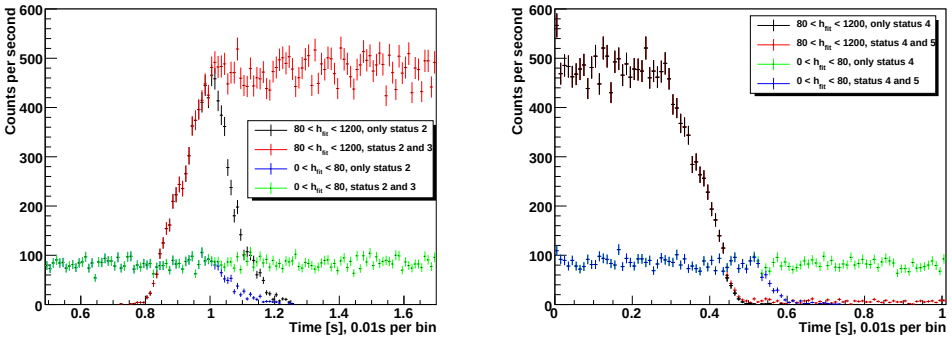

(a) Opening the shutter.

(b) Closing the shutter.

Figure 6.14: The count rates during the opening and closing of the shutter, plotted against the time since the first events with shutter status 2 and 4, respectively. Graphs show the sum of all measurements of 20_05_08/night. The black and red curves curves show events in the proton window, black is status 2 for the opening (4 for the closing) only, red the sum of states 2 and 3 (4 and 5). Green and blue show the same shutter states but for events in the electronic noise.

The shutter opens and closes quite fast. Typically, status 2 is about 1.1 s long, status 4 only 0.6 s. Fig. 6.14 shows different count rate distributions for the opening and closing of the shutter.

To gain enough statistics, all measurements with 50 V analysing plane voltage from one run were summed up. The different measurements were synchronised by assigning the time 0 to the first event with shutter status 2 for opening (4 for closing), for each file.

The graphs show that the actual closing time of the beam is much shorter than the length of the corresponding shutter states. Although the distributions are smeared out by the summation over the files, the opening takes place between 0.8 and 1.0 s, the closing between 0.3 and 0.5 s after the start of status 2, 4, respectively. There are two reasons why the shutter states are longer than the opening and closing times of the beam: On the one hand the shutter is displaced more than the actual width of the neutron beam, thus the driving time of the shutter is longer than the closing time of the beam. On the other hand the shutter states are defined by the DAQ in a way that ensures that states 1, 2, and 3 are correct. This means, for example for the opening of the shutter the DAQ sets the status on 2, then gives the command to open the shutter, status 3 only starts after the DAQ has received the signal from the end switch. The switches are read in loops, this adds some extra time to the duration of the states.

If only state 2 or 4 are drawn the count rates go back to 0, simply because the shutter reaches the end switch and the further events are assigned the next shutter state. The smearing out comes from the different durations of the shutter states for the single files that were summed up. From the blue curve in fig. 6.14(b) it is clearly visible that this happens about 0.1 s after the neutron beam is blocked.

Several systematic investigations exploiting the automatic shutter were done. For example, to investigate trapping effects, different settings of the voltages on the lower pair of $\vec{E} \times \vec{B}$ electrodes were used. Fig. 6.15 shows a comparison of the evolution of the count rate over the measurement time in the proton window for two different settings of the $\vec{E} \times \vec{B}$ field.

For the very low drift potential of $U_{\mathrm{E\times B,1}} \mid U_{\mathrm{E\times B,2}} = -2.4\,\mathrm{V} \mid 0\,\mathrm{V}$ the count rate starts to fluctuate as soon as the shutter is opened and even after it is closed again particles still reach the detector. For $-200\,\mathrm{V} \mid 0\,\mathrm{V}$ the count rate is stable as long as the shutter is open and drops back to the normal background count rate after the shutter is closed.

6.3.2 Closed shutter

The parts of the measurements without neutron beam before and after a period with open shutter allow for a detailed search for background produced inside the spectrometer, either by the neutron beam, the decay pro-

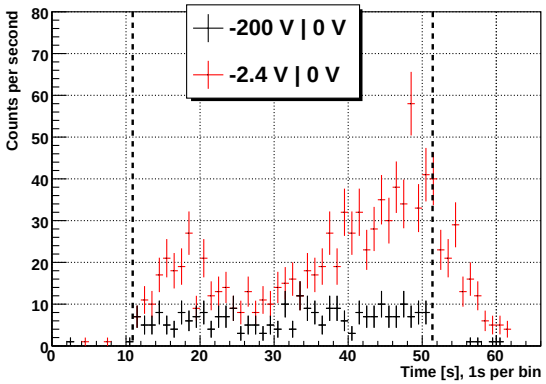

Figure 6.15: Comparison of measurements with two different settings of the lower $\vec{E} \times \vec{B}$ electrodes. The thick, dashed, black lines denote the opening and closing of the neutron shutter, showing the efficiency of the $\vec{E} \times \vec{B}$ field for removing trapped, charged particles.

ducts, or by other sources (e.g., field emission of electrodes).

The count rate in a single measurement without neutron beam is far too low to draw any conclusions. Only after summing up all measurements from one full run of typical duration and plotting the results in logarithmic scale, a small background contribution was found.

As visible in fig. 6.16, one or two small peaks arise in the spectra for shutter status 5, depending on the analysing plane voltage. Peak 1 is between ADC channels 350 and 450 and is visible for all voltages, peak 2 appears only for measurements with 0 and 50 V. It is situated between ADC channels 500 and 600, thus has roughly the same pulse-height as the proton peak. The pulse-height of peak 1 increases slightly with the analysing plane voltage. For the second peak no shift is visible, but the difference between 0 and 50 V is too small to be visible anyway. The intensity of this peak is lower for 50 V than for 0 V, whereas the intensity of peak 1 increases minimally with the analysing plane voltage.

The time distribution of the events with closed shutter reveals further information about the sources of the background. Fig. 6.17(a) shows the time distribution for 780 V before and after the shutter was open, fig. 6.17(b)

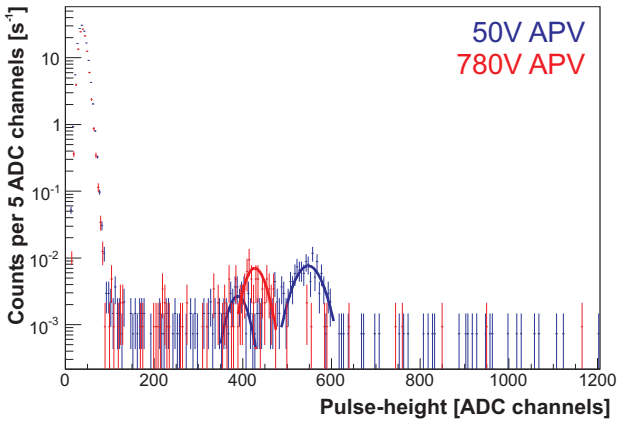

Figure 6.16: Spectra for shutter status 5. One peak for 780 V and two peaks for 50 V were found in the background analysis. To retrieve visible peaks all measurements from a full run were summed up and the spectra were rebinned by a factor of 5. This means the counts of 5 ADC channels are summed up and plotted as one point in the spectrum. The red and blue lines are Gaussian fits to the peaks in the 780 and 50 V spectra, respectively.

for 50 V. Again, all measurements from one data set were summed up to gain sufficient statistics. For 780 V the count rate after the open shutter is higher than before, but no significant time dependence is visible. However, for 50 V the count rate clearly decreases in shutter status 5, i.e. after the shutter was open.

The count rate with closed shutter is not statistically distributed over the measurements. Many measurements show count rates of none or only one count in 10 s, others show much higher count rates up to about $1.5\,\mathrm{s}^{-1}$. The source of the background is obviously fluctuating.

Detailed studies of the background[4] revealed the following information about the background peaks:

Peak 1 is situated between ADC channels 350 and 450.

- Visible for all analysing plane voltages, both in shutter status 1 and 5.

[4]These studies were performed by M. Borg and are discussed in detail in [54].

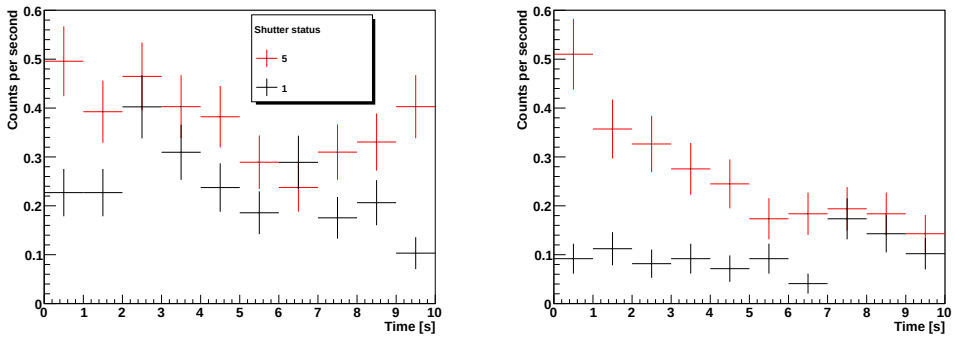

(a) 780 V. (b) 50 V.

Figure 6.17: Evolution of the count rates before (black) and after (red) the beam was open, for 50 and 780 V analysing plane voltage. Graphs show the sum of all measurements of 19_05_08/night.

- Appears both for 10 and 15 kV acceleration voltage.
- The intensity of the peak is fluctuating randomly.
- The peak superimposes the measurements with open shutter.
- The particles are produced above the analysing plane by a mechanism coupled to the electron trap between the lower $\vec{E} \times \vec{B}$ electrodes and the negative high voltage at the detector and the upper $\vec{E} \times \vec{B}$ electrodes.

Peak 2 is situated between ADC channels 500 and 600.

- Visible only for 0 and 50 V analysing plane voltage in shutter status 1.
- The intensity decreases from 0 to 50 V analysing plane voltage, at 250 V or higher it cannot be observed. Therefore, the source of the background has to be below the analysing plane.
- After closing the neutron shutter, the peak decays exponentially with a time constant of 2 to 3 s. This long time constant points to a production mechanism involving trapped electrons that ionise residual gas molecules.

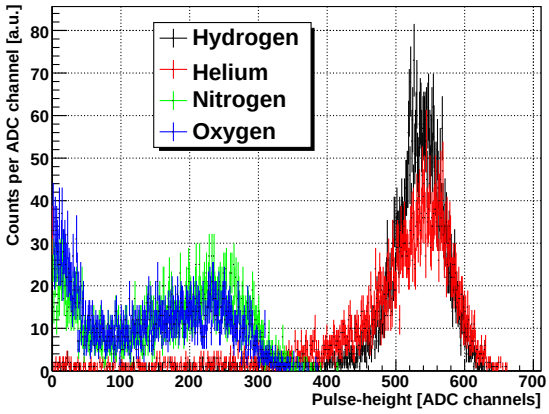

Figure 6.18: Simulated spectra for different ion types with 15 keV impact energy and 0° impact angle.

- The effect fluctuates and appears randomly, also when the shutter is open.

To identify the types of ions in the background, simulations for the most probable ions were done with SRIM and analysed with the routines described in sect. 4.5. The resulting spectra are shown in fig. 6.18. Unfortunately the results are not conclusive. Whereas protons or helium ions may be the cause for peak 2, heavier residual gas ions, like oxygen and nitrogen, are expected only at pulse-heights below ADC channel 300. A hypothetical explanation for peak 1 is of course protons with a reduced energy of about 12 keV, pointing to a production region close the the detector or the upper $\vec{E} \times \vec{B}$ electrodes.

Although there are still background contributions which depend on the analysing plane voltage, their intensity was reduced by a factor of 5 to 10 in comparison to the beamtime at the FRM-II.

In a future beamtime, the exact value where peak 2 disappears should be determined and this voltage should be used instead of the 50 V measurements for the fit of a.

6.4 Correlated events

Due to kinematics reasons, only a fraction of the decay electrons reaches the detector and is detected in coincidence with the proton from the same decay. There are two possibilities for the electrons to reach the detector. On the one hand they can be emitted into the upper hemisphere and reach the detector directly. Simulations show that these are about 14.7 % of the electrons. Hence, in absolute numbers and extracted from the proton count rate at 0 V analysing plane voltage, one expects a count rate of $\approx 72(2)\,\mathrm{s}^{-1}$ for these electrons. On the other hand, electrons that were initially emitted into the lower hemisphere, can be backscattered on the grid wires of the mirror electrode or the bottom plate of the electrode system. According to simulations, up to 15 % of the electrons may be backscattered [28], but the exact amount is difficult to predict due to the complicated geometry of the surface. Only a fraction of the backscattered electrons reaches the detector due to the magnetic mirror. In the experiment an average electron count rate of $97.5(8)\,\mathrm{s}^{-1}$ was observed.

Due to their higher energies and lower weight, the electrons arrive at the detector much faster than the protons. Compared to the proton time of flight, the electron's is very short and the time difference between them is essentially the time of flight of the proton from the decay volume to the detector. The proton's minimal flight time was calculated to be 6 μs, but this value depends on the setting of the analysing plane voltage. At high barrier voltages the protons travel with reduced velocity through a long part of the spectrometer[5], hence the protons have shorter times of flight at 50 V than at 600 V. Therefore, a time dependent loss mechanism has a stronger influence on measurements with low analysing plane voltages and thus has a strong influence on a. Fig. 6.19 shows time of flight spectra for all measured voltages.

Such time dependent loss mechanisms were discovered during the analysis and will be described in the next section.

[5] The analysing plane electrode and the surrounding electrodes are about 1 m long in total.

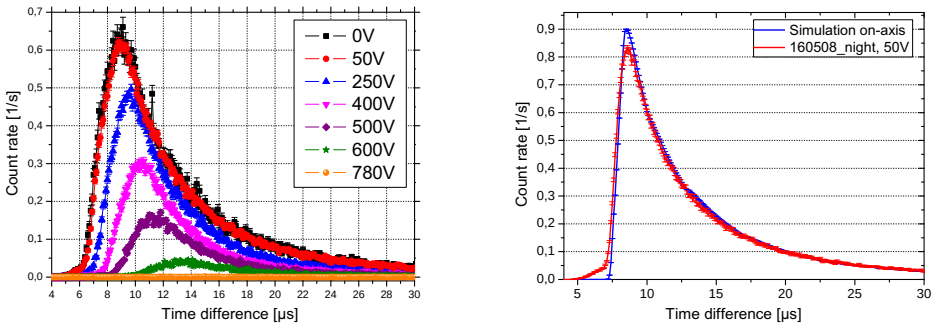

(a) (b)

Figure 6.19: a) Time of flight spectra for all measured analysing plane voltages. Higher voltages shift the starting points and positions of the maxima to higher flight times. The amount of consecutive events decreases due to the potential. b) Comparison of measured and simulated time of flight spectra. Simulation done by G. Konrad [28].

6.5 Baseline shifts

The pulses of high energetic electrons are longer than the event window, so it is possible that correlated protons following the electron after a short time are on the tail of the electron event. Additionally, after high energetic electrons the baseline drops to values between 1000 ADC channels and the normal baseline value of about 1500 ADC channels. A typical example for this is shown in fig. 6.20(a). Most events have a baseline of 1490 ± 20 ADC channels, but baselines for events shortly after saturating events have a lower baseline. Those form the broad pedestal from ADC channels 1000 to 1400 in fig. 6.20(b).

Although the pulse-height of such events can be roughly corrected with the fits, this behaviour causes two effects with consequences for the result of the measurement:

First, the trigger efficiency is altered for protons on the tail of an electron. On the falling edge of an electron, the value of window w1 is shifted to higher values compared to the value of the real baseline at the position of window

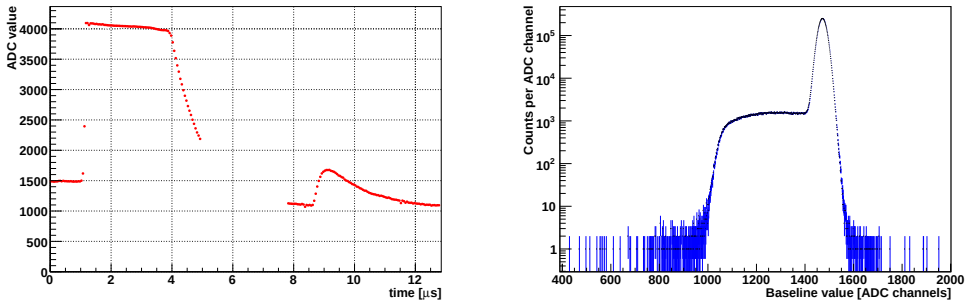

(a) (b)

Figure 6.20: a) An electron followed by a proton. The electron event (starting at $\sim 1\,\mu$s) saturates the electronics and is therefore cut off. After the electron the baseline drops to ADC values around 1100 and the following proton (starting at $7.8\,\mu$s) has a lower and changing baseline. The red dots show the ADC values of two successive events, the information in between the events was not recorded. b) Distribution of baseline values for one file.

w2[6]. Events will be lost if they have a rather low pulse-height and the shift of the first trigger window is too high.

6.5.1 Trigger efficiency

The effect of the reduced trigger efficiency after electrons was investigated with a program that creates artificial double event data of electrons and protons and applies the same trigger algorithm as the sADC board to these artificial pulses. This is necessary as not all the ADC values used for the trigger decision by the sADC board are contained in the event data written to the PC. Furthermore, this method allows to freely choose the different parameters which are important for the trigger. Besides the settings of the trigger algorithm, these are the exact point where the saturation of the electron ends, the time difference between electron and proton, the pulse-height of the proton, and the value the baseline drops to. The slope of the electron was determined by exponential fits to electron pulses measured

[6]See sect. 4.4.2 for details on the trigger algorithm.

during the beamtime. Additionally, artificial noise can be added to the signals to get a more realistic result. Fig. 6.21 shows two such events. In both pictures, the baseline drops to 1200, the saturation ends at bin -15, and the proton pulse-height is 250. This analysis shows that, for the usual trigger settings, the proton would be triggered if it arrives 6 μs after the electron (case (a)), but not if it arrives only 5.5 μs after the electron (case (b)).

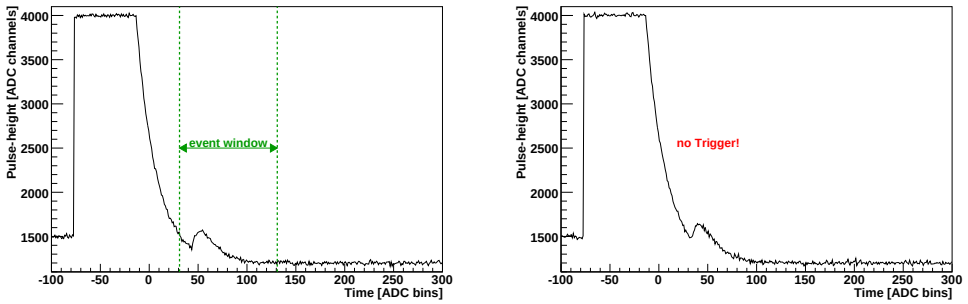

(a) time difference 6.0 μs. (b) time difference 5.5 μs.

Figure 6.21: Two simulated events where the baseline drops after an electron and the proton is on the tail of the electron pulse.

With this technique the parameter space of the time difference, the lowered baseline, the end point of the saturation, and the pulse-height of the proton can be scanned within reasonable limits for the single values and a map can be created which tells for which combinations of parameters a trigger is expected. Fig. 6.22 shows two such maps for different parameter combinations. For example, a proton with a pulse-height of 150 ADC channels following 6 μs after an electron would be triggered if the saturation of the electron ends at bin 75, but not if it ends at 80.

Typically, the baseline drops at most to about 1000 ADC channels (see fig. 6.20(b)), the saturation of the electron ends at latest at bin 85 for practically all electrons.

These maps, together with simulations of proton and electron flight paths in the spectrometer, would allow estimations of the amount of protons lost due to the reduced trigger efficiency at short time distances after high ener-

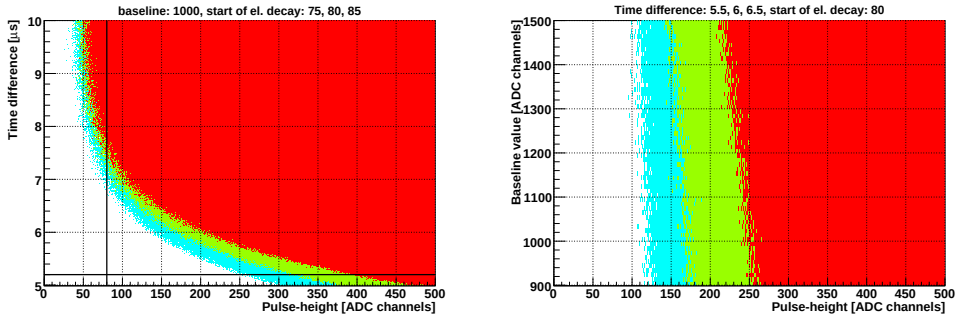

(a) (b)

Figure 6.22: Two scatter plots of expected trigger regions for the simulated double events: a) Proton pulse-height versus time difference to the electron event for a baseline lowered to 1000 ADC channels. The horizontal black line denotes the minimal time difference in the real measurement, given by the dead time of the electronics. The vertical line denotes the usual lower integration limit of the pulse-height spectra. The colours show the expected trigger regions for the start of the electron decay at bin 75 (blue), 80 (green), and 85 (red) in the window of the electron event. b) Proton pulse-height versus minimum of the baseline. Here the colours denote a time difference between the two events of 5.5 (red), 6.0 (green), and 6.5 μs (blue). The blur of the borderlines in both pictures comes from the artificial noise that was added during the calculation of the pictures.

getic electrons. Unfortunately, another effect caused by the electronics at short time differences was discovered which will be described in the following section.

6.5.2 Pulse-height effects

In fig. 6.23 measured pulse-height spectra for events after high energetic electrons are shown. To create these spectra, all measurements with 50 V in the analysing plane from the night of May 20, 2008 were used. Each high energetic event that saturated the shaper was used as a start signal and all following events up to the next high energetic one were filled into the

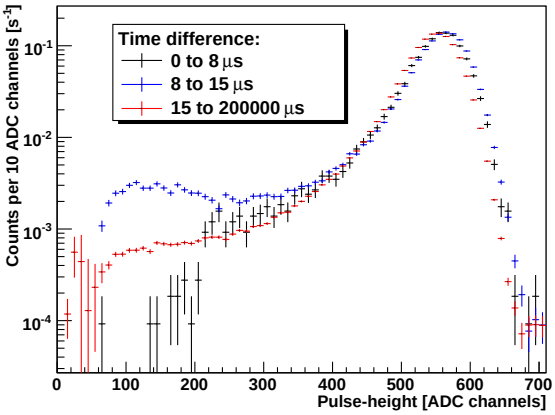

Figure 6.23: Pulse-height spectra for events arriving at the detector in different time ranges after an high energetic electron.

spectra depending on the time since the high energetic event. Afterwards, for each spectrum the background was subtracted and it was normalised to the count rate between pulse-height 500 and 600.

For events less than 8 μs after an electron, there are almost no counts with pulse-heights below 200 ADC channels. This is due to the alteration in trigger efficiency, described in sect. 6.5.1.

On the other hand, between 8 and 15 μs after an electron, there are more counts with low pulse-heights. Further information was revealed by scatter plots of the baseline value versus the pulse-height of each event after an electron. Fig. 6.24 shows such a plot for a file with 50 V in the analysing plane. As expected, a strong horizontal band of events shows the distribution of the proton events with lowered baselines. However, the additional count rate already observed in fig. 6.23 is not randomly distributed, but forms a diagonal branch. There seems to be a mechanism that links an only slightly lowered baseline to a strongly reduced pulse-height of the proton. Investigations showed that the extra count rate appears only after electrons that saturate the electronics for a very long time (about 60 ADC time bins).

The effect can be explained by a saturation of the preamplifier: As explained in sect. 4.4, signals from the detector are amplified, shaped and finally digitised. The cut-off of the events seen in the pulse shapes is due

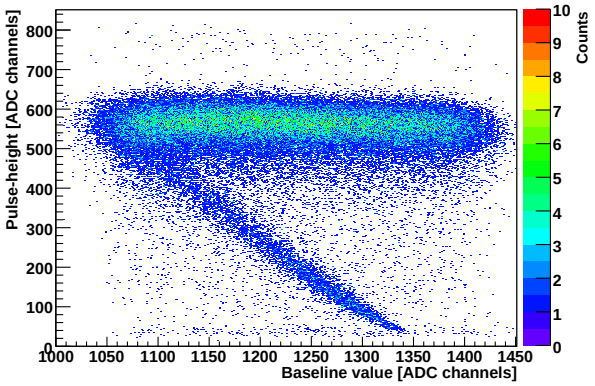

Figure 6.24: Scatter plot of the drop value of the baseline versus the pulse-height.

to a saturation of the shaper, but for very high energetic events also the preamplifier may saturate. The principle is shown in fig. 6.25. The original pulse given by the detector consists of a steep rising part with a rise time of typically 25 ns and a long decay with a decay time of about 150 μs. Thus any event following after a short period will sit on the shoulder of the previous pulse. The shaper then differentiates and integrates the signal and is mostly sensitive to the rising edge of the signal. The height of the pulse after the shaper is proportional to the change in pulse-height before the shaper.

If now an electron deposits so much energy in the detector that the preamplifier comes close to saturation or even saturates, an event following after a short time will drive the preamplifier into saturation and thus cut off the second peak. After the shaper the peak will have a lower pulse-height as well.

To verify that the saturation of the preamplifier really causes the effect of the reduced proton pulse-heights, the electronics was tested in several steps. First the waveform produced by the detector before the preamplifier was determined. Then the detector was disconnected from the electronics and electron-like and proton-like pulses were generated with a waveform generator and fed through the electronics. These pulses were observed with an oscilloscope at different stages of the electronics chain. Finally, the pulses

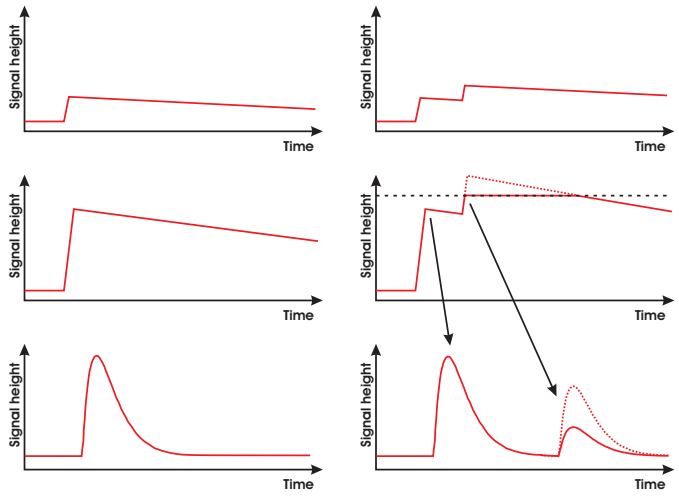

Figure 6.25: Schematic of the preamplifier saturation. Left: Single event. Right: Saturation for subsequent events.

were also observed with the sADC. Details of the electronics tests and their results will be discussed in the following section.

6.5.3 Electronics tests

To test the behaviour of the electronics an arbitrary waveform generator (Agilent 33250A) was used. The freely programmable waveform generated by this device was fed through the electronics chain and read out with a Tektronix 3034 oscilloscope before and after the preamplifier and after the shaper. The same electronics components as during the beam time were used.

Waveform of cosmic events

To figure out the correct waveform, the detector was connected to the electronics and the signals produced by cosmic rays were read out after the preamplifier board with the oscilloscope. Then, instead of the detector, the waveform generator was connected to the input side of the preamplifier board. The waveform is given by the same mathematical function as

the fit function eq. 6.2 but the values of the parameters are different. The parameters were optimised to reproduce the signals of the cosmic rays as precisely as possible. This is of crucial importance as the input waveform also determines the shape of the signal after the shaper and thus influences the performance of the triggering algorithm. Fig. 6.26 shows a comparison of the resulting waveforms after the preamplifier.

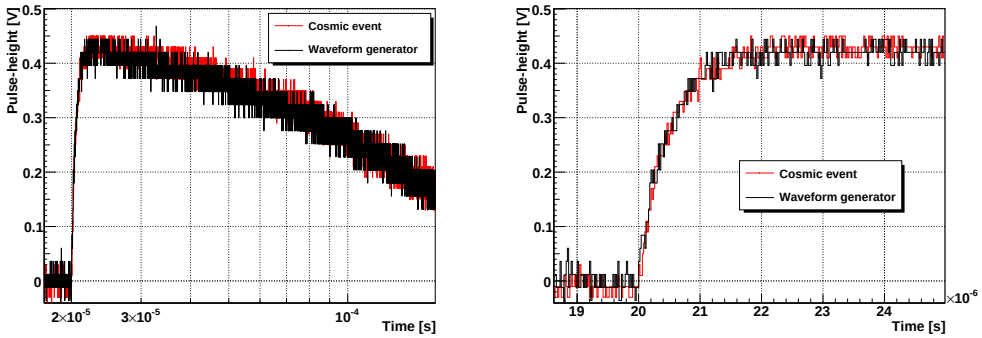

(a) (b)

Figure 6.26: Comparison of the pulse form of a cosmic event and an event generated by the arbitrary waveform generator. (a) shows the full pulse, (b) is a zoom on the rising part of the pulse. The rise time is 25 ns, the fall time 150 μs.

Investigations with the oscilloscope

Instead of the detector, the waveform generator was connected to the input side of the preamplifier board. The waveform determined by the cosmic rays was then used to investigate the effect of a high pulse followed by a low pulse after a short time. The resulting waveforms, captured with the oscilloscope, are shown in fig. 6.27.

An electron-like pulse at time 0 s is followed by a proton-like pulse after 7.5 μs. Different heights of the electron-like pulse were used, the height of the proton-like pulse was kept constant. Before the preamplifier (fig. 6.27(a)) the proton-like pulse is hardly visible due to the noise of the oscilloscope. The detector senses the electrons that drift into its centre,

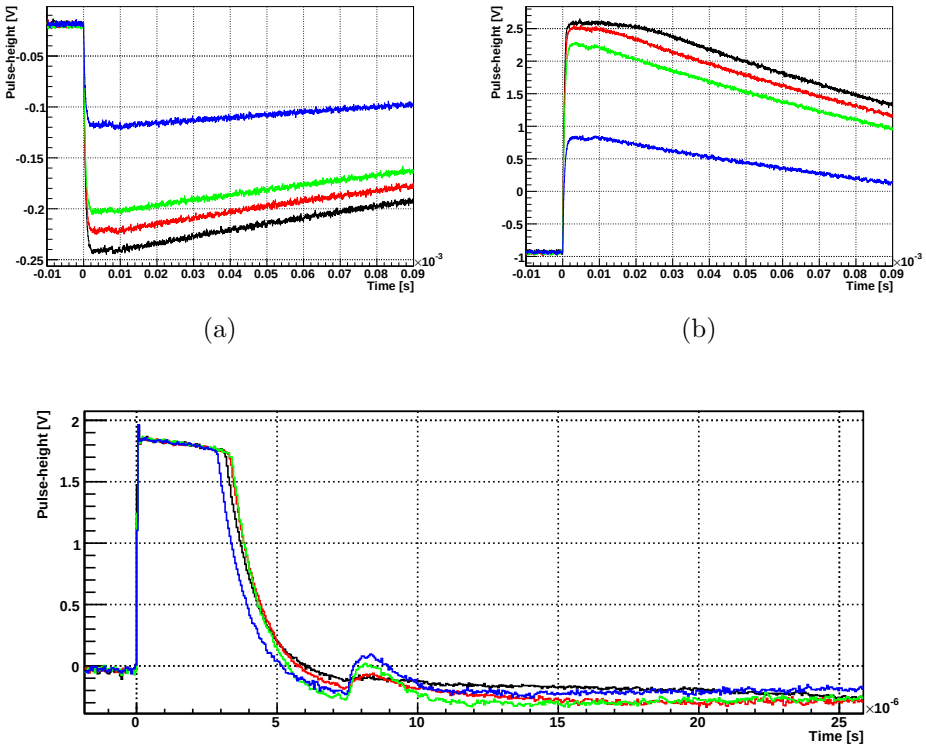

Figure 6.27: A high, electron-like pulse followed by a low, proton-like pulse with a time difference of 7.5 μs. The graphs show the input waveform (a), the waveform after the preamplifier (b), and after the shaper (c). Note the different time-scale in (c).

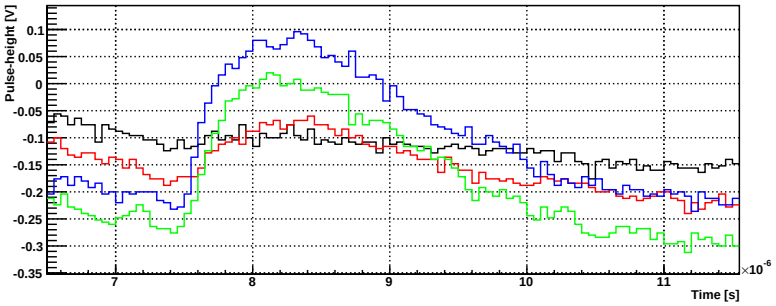

(a)

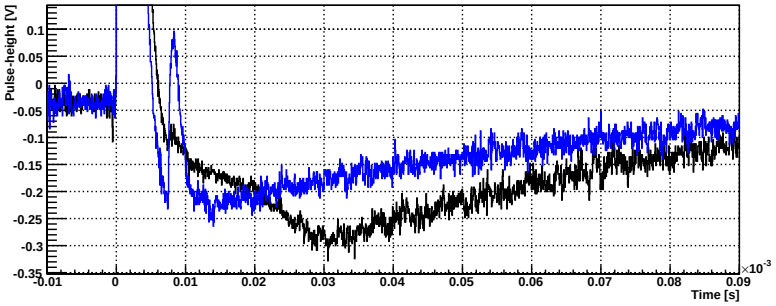

(b)

Figure 6.28: Different displays of fig. 6.27. a) Zoom on the region where the proton-like event would be triggered by the sADC. b) Temporal evolution of the baseline after the pulses. For better visibility only the waveforms with the lowest and the highest electron-like pulse-height are plotted.

hence the pulses are negative. The preamplifier inverts and amplifies the pulses (fig. 6.27(b)). For very high electron-like energies (red and black curves) the maximum amplitude of the preamplifier is reached and the waveform becomes more or less flat in the time region of the proton-like pulse. The shaper shortens the pulses (fig. 6.27(c)). All used electron-like pulses saturate the shaper and thus the pulses after the shaper are flat at their tops.

Fig. 6.28(a) shows a zoom on the region of the proton-like pulses. For the waveforms where the electron-like pulse does not saturate the preamplifier

(blue and green curve), the pulse-height of the proton-like pulse is the same, only the baseline drops more for the higher electron-like pulse. However, as soon as the preamplifier saturates, the pulse-height of the proton-like pulse is lowered (for the red curve) or even almost vanishes for a strong saturation (black curve).

The stronger the saturation, the less is the reduction of the baseline in the region of the proton-like pulse. Due to the flat top of the saturating pulses after the preamplifier the baseline after the shaper first forms a pedestal during the saturation and drops as soon as the saturation ends. This effect, shown in fig. 6.28(b), allows to explain the diagonal branch in fig. 6.24. A strong saturation of the preamplifier makes the baseline drop less and at the same time lowers the pulse-height of the following proton more.

Reproduction of the saturation effect

After the tests with the oscilloscope, pulses from the waveform generator with different heights of the electron-like pulse and different time differences of the proton-like pulse were fed through the entire electronics chain, including the digitising by the sADC and the readout by the DAQ PC. The same trigger settings as in the beamtime were used. The height of the proton-like pulses was roughly kept constant for the different electron-like pulse-heights. The programming scheme of the waveform generator does not allow to set the height of the proton-like pulses separately. The entire waveform has to be created and then the overall amplitude of the waveform can be set. Therefore the proton-like pulse-heights differ between about 520 and 700 ADC channels. Five different amplitudes were used, from values far below the saturation to clearly above it. The waveforms before and after the preamplifier are shown in fig. 6.29.

Fig. 6.30 shows spectra taken with the sADC for different amplitudes and time differences. The noise level was much lower than usual, since the detector was not connected. Thus no noise is triggered with the used settings of the trigger. For an amplitude below the saturation (fig.6.30(a)) there are only minor fluctuations in the pulse-height for the different time differences. These fluctuations are caused by the uncertainty of the baseline determination. For short time differences the pulses are on the falling part of the baseline, for longer time differences they are on the part where the baseline rises, and for very long time differences the baseline already recovered to

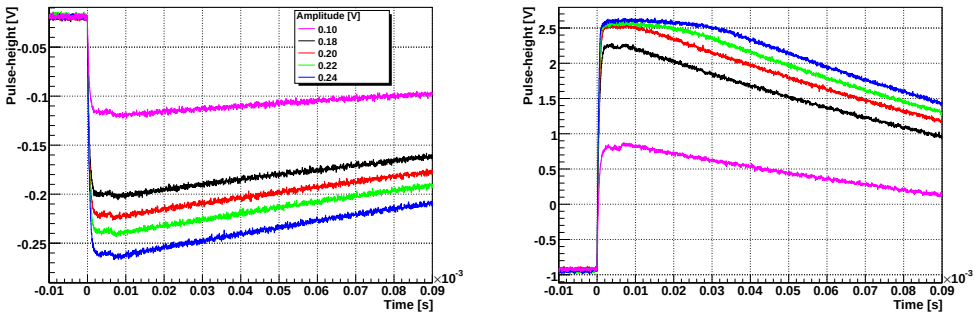

(a) Input signal.

(b) After preamplifier.

Figure 6.29: Different amplitudes used for the investigations with the sADC.

its original value. The strange shape of the peak at 7 μs time difference is caused by the fitting process. The proton-like pulses are on the falling baseline, part of the pulses just fulfil the χ^2-condition and are fitted with the normal fit function (fit status 0), whereas the others are fitted with the special function on an exponentially dropping baseline (fit status 5). The baseline values y_0 determined by the normal fit are too high and those pulses are thus assigned a lower pulse-height[7]. A measurement with a time difference of only 6 μs showed no proton-like counts, due to the reduced trigger efficiency on the falling edge of an electron-like pulse, described in sect. 6.5.1. The proton-like pulse is visible in the waveform picture taken with the oscilloscope, but it is not triggered by the sADC.

For higher electron-like pulse amplitudes, the saturation of the preamplifier shifts the proton-like pulse-heights to lower values and the minimum time difference to detect the proton-like pulse at all becomes larger. Spectra with lower time differences than the lowest one in each of the pictures in fig. 6.30 do not show any proton-like counts. Even if the preamplifier is in saturation, the proton-like pulse is detected with a very low pulse-height, as long as it is not too close to the electron-like pulse and thus sitting on the falling part of the baseline. The baseline reaches its minimum after about

[7]The shift of this peak is also visible in the non-fitted spectra, where the baseline is determined from the first 15 ADC bins.

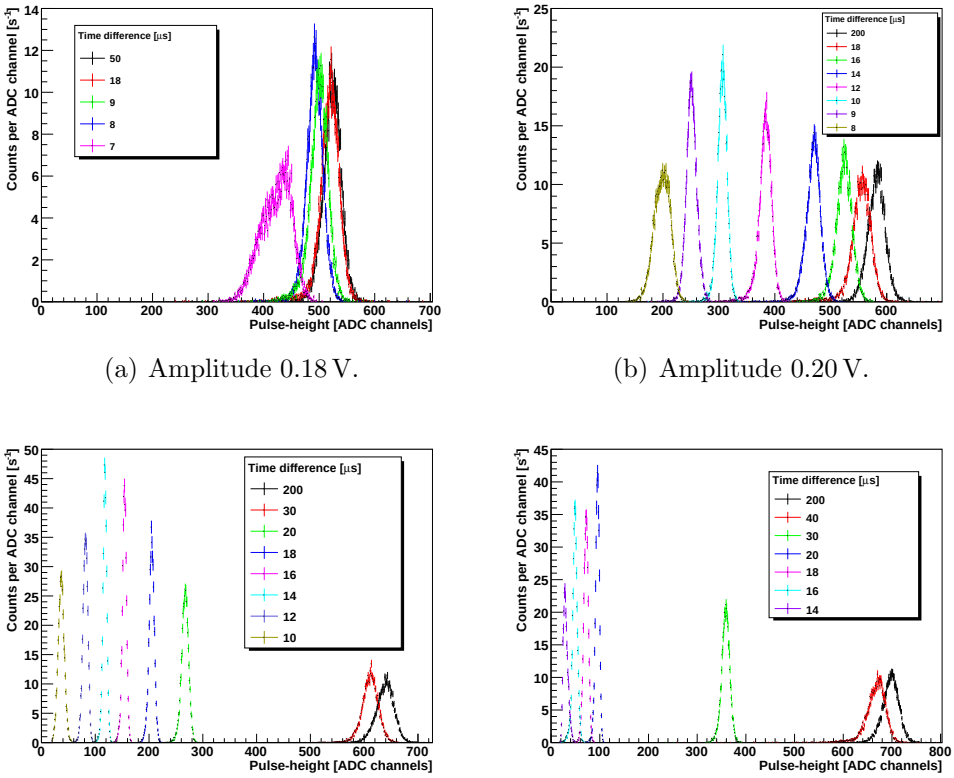

(a) Amplitude 0.18 V.

(b) Amplitude 0.20 V.

(c) Amplitude 0.22 V.

(d) Amplitude 0.24 V.

Figure 6.30: The pulse-height spectra for different amplitudes of the electron-like pulse and several time differences between electron-like and proton-like pulse. Note that the colours in the single plots do not correspond to a fixed time difference. For better visibility, only a selection of spectra for each measured amplitude is shown.

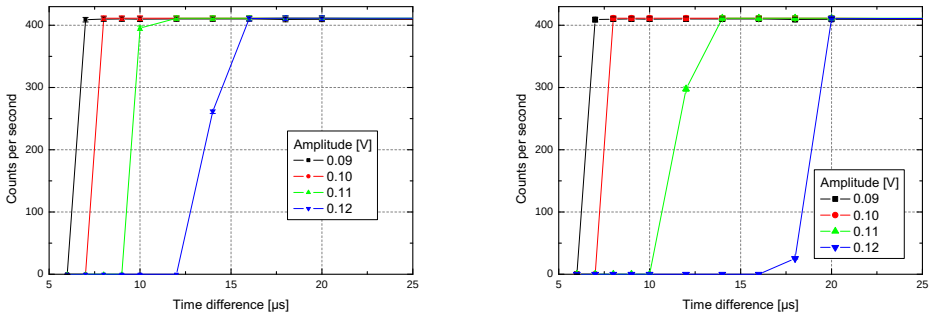

(a) Lower integration limit ADC channel 0. (b) Lower integration limit ADC channel 80.

Figure 6.31: Integral count rates for different electron-like pulse-heights and time differences. (a) shows all events that were triggered, (b) only the ones which would be counted with the usual lower integration limit for the spectra.

10 to 15 μs.

These results explain both effects shown in fig. 6.23. At very low time differences protons are not triggered, as demonstrated here with the measurement with 0.18 V amplitude. For slightly higher time differences protons are detected with a lower pulse-height, depending on the pulse-height of the electron.

Fig. 6.31(a) and fig. 6.31(b) show the integral count rates of the spectra shown in fig. 6.30 for a lower integration limit of 0 and 80 ADC channels, respectively. For high electron-like amplitudes, proton-like pulses with lower time differences are counted as well and the integral count rate reaches its maximum earlier. There is no slow rise in the count rate, but it rises from no counts to the full count rate quite quickly. Unfortunately, even though the pulses with low pulse-height can be detected with the test setup, in the real measurement they are pushed into the region of the electronic noise. Due to fluctuations of the noise, lowering the lower integration limit in the real measurement would cause a very large error bar on the value for a and thus does not allow to gain further knowledge about the value of a.

From the measurements, and with the conversion factor of 63 ADC channels per keV energy, the minimum energy to saturate the preamplifier that has to be deposited in the detector by an electron can be calculated to be about 400(20) keV. The rather large error bar comes from the difficulty to determine the exact point where the saturation starts. Even after the preamplifier is clearly in saturation the maximum voltages still rises a little bit. This does not mean that every electron with more than 400 keV saturates the preamplifier. The simulations in sect. 4.5.3 have shown that only a fraction of the high energetic electrons is actually stopped inside the detector. About 12 % of the electrons arriving at the detector deposite more than 400 keV in it. The distribution of all electrons arriving at the detector is shown in fig. 4.14(c).

However, the energy needed to saturate the preamplifier might change as soon as the detector is connected, as it might alter the performance of the preamplifier (e.g., by introducing an offset in the baseline).

The tests of the electronics with the waveform generator clearly revealed the saturation of the preamplifier and the resulting shift of the pulse-height of protons arriving at the detector shortly after a high energetic electron. In combination with the fact that the flight time differences of correlated electrons and protons depend on the analysing plane voltage (sect. 6.4) the dependence of a on the lower integration limit (sect. 6.2.4) can be explained. For low analysing plane voltages more protons are shifted to low pulse-heights. Depending on the lower integration limit a fraction of them is not taken into account for the fit of a. Thus also a depends on the lower integration limit.

6.5.4 Correction of the saturation effect

Two possible ways may lead to a correction of the data. Either a corrective curve from the measurements with the waveform generator has to be extracted, or a cut in the measured time of flight spectra at a sufficiently long time difference has to be applied.

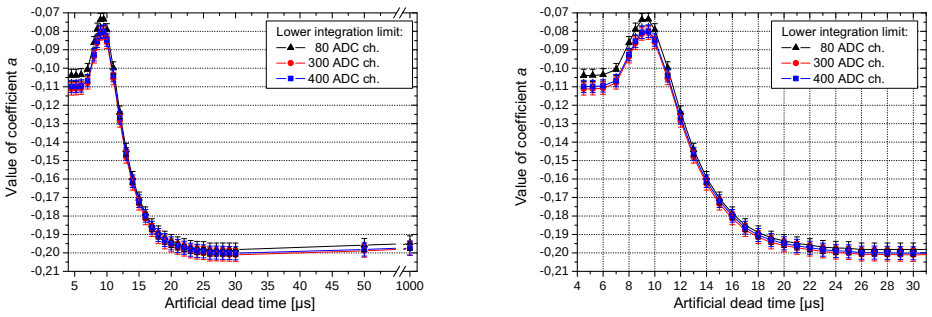

(a) Full picture. (b) Zoom.

Figure 6.32: Dependence of a on an artificial dead time after electrons, for the data set 17_05_08/night.

Time cut

The saturation of the preamplifier only alters the count rates at short time differences after electrons. A defined cut at a sufficiently high time difference removes all events where a saturation of the preamplifier may have happened. Artificial dead times from 4.5 to 1000 μs were assigned to all electrons with pulse heights above 1200 ADC channels. The influence on a is shown in fig. 6.32. Increasing the dead time after electrons shifts the value retrieved for a up to $\Delta a/a \approx 100\,\%$. The huge shift is caused by the different amounts of correlated events that are excluded for each analysing plane voltage.

Calculations done by G. Konrad [28] show a similar behaviour, but they their shape depends strongly on the input parameters and several eligible combinations have different outcomes. These parameters are not restricted enough by the band of curves extracted from the data. The biggest uncertainty comes from the non-predictable angular and energy distribution of the backscattered electrons. Thus, a reliable characterisation of protons lost by the saturation effect does not seem to be achievable on a admissible level of accuracy.

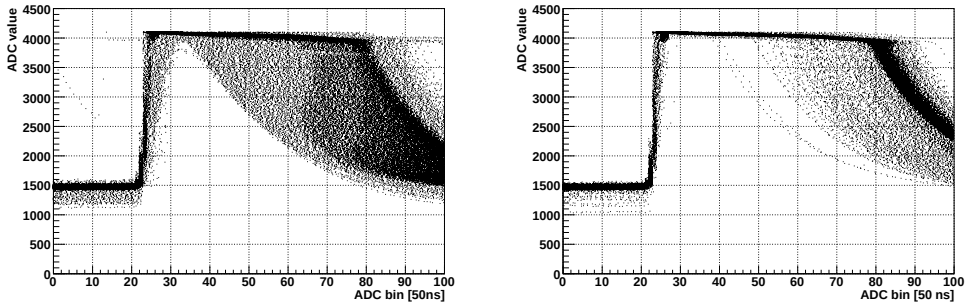

(a) (b)

Figure 6.33: Comparison of pulse shapes of electrons that are followed by a proton with normal pulse-height (a) and with low pulse-height (b). Each picture shows a multitude of electron events. Each point corresponds to one ADC value in the respective time bin of the event.

Correction curve

The correction curve would have to provide the relation between the electron energy, the time of flight of the proton and the resulting pulse-height of the proton. The convolution with the trigger efficiency would then reconstruct the lost proton counts for each measurement.

Unfortunately, there are far too many parameters which can only be determined with large uncertainties to be able to construct this curve. Most important, due to the saturation of the shaper, all high energetic electron pulses look very similar. There is no handle to decide if and for how long a specific electron saturated the preamplifier or not. Although protons with reduced pulse-height mostly show up after electrons that saturated the shaper for a very long time (fig. 6.33(b)), also electrons which are followed by a proton with normal pulse-height partly saturate the shaper for the same time (fig. 6.33(a)). Several different techniques were studied, for example fits to the rising or falling part of the electron signal. But with none of them it was possible to separate electrons that saturate the preamplifier from the rest of the electrons. Furthermore, any correction would have to rely on the simulated time of flight spectra (fig. 6.19(b)). Those spectra do not match the measured ones precisely enough. If this is caused by

missing proton pulses due to the saturation effect or by a problem with the simulations cannot be decided. Further needed parameters are for example the backscattering of the electrons on the bottom flange and the energy deposited by the electrons in the detector.

6.6 Electronic noise

So far no active temperature stabilisation or control for the detector has been implemented. It is cooled by the surrounding cold bore tube and heated at the same time by the excess heat of the preamplifier. Additionally, some of the heat is taken away by the cooling air pumped into the preamplifier tube with a plastic tube, as described in sect. 4.3.2. The temperature of the pressurised air depends on the temperature in the guide hall, as a long tube is needed to bring the air to the top of the spectrometer and the guide hall is not temperature stabilised. These temperature fluctuations can also be seen in the noise of the electronics, as shown in fig. 6.34.

Fig. 6.34(b) shows the pulse-height spectra, focussed on the noise region, for several measurements with closed neutron shutter in the night run of May 6^{th}, 2008. This run was started about 20 minutes after midnight on 7^{th} of May[8]. Before the measurement the electronics were switched off for some time for maintenance. At first the system heats up due to the heat produced by the preamplifier, then, as the temperature in the hall drops during the night, the noise level goes down as well. In the late morning both temperature and noise level reach a minimum before they rise again until the run was stopped at 16:30.

Fortunately, only the amount of noise fluctuates, the pulse-heights stay practically constant, as can be seen in fig. 6.34(b). Thus there is no need to adapt the integration limits for different noise levels. However the total event rate changes, of course. Thus also the dead time of the detector does depend on the temperature and has to be corrected file-wise.

Although the influence of the temperature fluctuations on the results of the measurement is rather low, an active stabilisation of the temperature

[8] Although the measurement was only started in the early morning of May 7^{th} and all data was taken on that day, the run is still considered as the night run of May 6^{th}, according to the general naming convention.

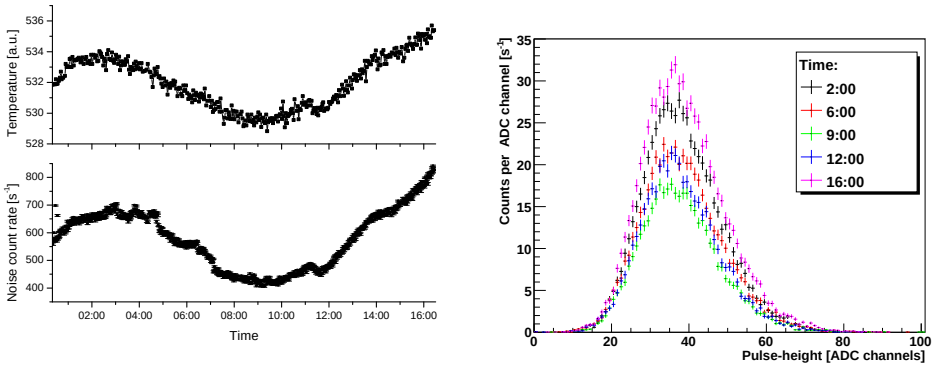

(a) (b)

Figure 6.34: a) Integral noise count rate and the temperature of the detector during a full measurement run. The temperature was measured with the diode on the detector chip and read out with the sADC. b) The electronic noise of the detector for different measurements during the same day.

could improve the stability of the measurements. An active and stabilised cooling system may improve the proton spectra further.

6.7 Trigger settings

On May 22nd the influence of different trigger settings on the measured count rates was investigated. The parameters of the trigger were varied over a wide range and for each setting a 300 s long file with 50 V in the analysing plane and a 120 s long file with 780 V was taken.

The resulting count rates in the proton window are shown in fig. 6.35, the trigger settings of each measurement are shown in table 6.4. The file numbers are the numbers of the 50 V files, for each one the corresponding 780 V measurement[9] was subtracted. Unfortunately, the reactor power was increased during files 22/23, thus another set of measurements with standard trigger settings was done with the files with numbers 24/25.

[9]The file with the odd number after the given number.

Within the error bars the count rate does not depend on the trigger settings, as long as window 1 is not chosen to be longer than 4. However, in a future beamtime, this measurement should be repeated with higher statistics to exclude a minor dependence of the count rates on the trigger settings.

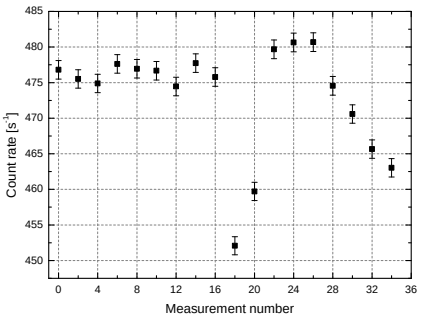

Figure 6.35: Impact on different trigger settings on the measured count rate.

File	w1	w2	Delay	Threshold
0	4	4	3	36
2	4	3	3	50
4	4	2	3	60
6	4	1	3	70
8	3	4	3	37
10	1	1	3	65
12	1	1	2	67
14	1	1	1	70
16	4	1	1	72
18	9	5	3	40
20	9	4	3	52
22	4	1	2	68
24	4	4	3	36
26	4	1	3	67
28	5	4	3	40
30	6	4	3	44
32	7	4	3	48
34	8	4	3	50

Table 6.4: Table of the trigger settings. The window sizes in time bins are 2^n, where n is the value given in the table.

7 Conclusion and outlook

During this thesis the retardation spectrometer *a*SPECT was set up for a first beamtime at the Institut Laue-Langevin with a new detection system. This beamtime mainly served to investigate systematic effects. The overall goal with *a*SPECT is to improve the accuracy of the world average value of the electron antineutrino angular correlation coefficient of $a = -0.103(4)$ [2]. With only one of three detector pads operational a statistical sensitivity of about 2 % per day was reached.

For the first time a silicon drift detector supplied by PNSensor was used to detect the low energetic protons. Due to its excellent noise characteristics, this detector has a much better resolution than the previously used silicon strip detector. With the new detector the acceleration voltage could be reduced by a factor two down to 15 kV. This solved the problem of frequent electrical breakdowns and, in combination with the redesign of several electrodes, significantly improved the background conditions.

During the data analysis a variety of systematic effects was studied. Fluctuating contributions to the background were found on a very low level. However, an energy dependent saturation effect of the preamplifier prevented the extraction of a value for a with a reasonable error bar. An upper limit for the error due to this effect is $\Delta a/a = ^{+30}_{-60}$ %. This effect was unfortunately discovered only after the beamtime but can be easily avoided in future measurements. Despite the effect valuable knowledge was gained about the performance of the spectrometer. Many other systematic effects are now well understood and lead to rather small corrections and systematic errors. The most important ones are listed in table 7.1.

The new detector was taken into operation and its properties investigated at a proton beam test facility. For its implementation in the spectrometer

Type of correction	Relative correction [%]	Relative error [%]
Magnetic field ratio r_B	0	$< \pm 0.5$
Dead time	4	$< \pm 0.04$
Edge effect	≈ 1.2	± 0.1
Background	2.2	± 0.5
Proton simulations	0.13	± 0.09

Table 7.1: Corrections and systematic errors.

parts of the electronics and the mechanical setup were redesigned. The interactions of the protons and electrons in the detector were carefully simulated and the measured proton spectra could be reconstructed. During the beamtime the beam profile and the magnetic field inside the spectrometer were precisely measured. The data acquisition and instrument control programs were improved or newly programmed. Also for the analysis of the data a set of programs was developed, including a fit routine that allows to reconstruct the pulse-height for almost any event.

The knowledge about different systematic effects acquired during this thesis suggests various improvements of the spectrometer. First, the saturation effect can be removed by simply reducing the amplification of the preamplifier by a factor of two to three, which still keeps the pulse-height of the protons on a reasonable level. A shorter shaping time will reduce the event length and the probability of pile-up. With a proper choice of parameters the undershoot of the baseline after high pulses can be removed. A further, optional feature would be a non-linear (e.g., logarithmic) amplification for high resolution of the small proton signals, while avoiding saturation due to the high energetic electrons. A stabilised cooling system for the electronics can improve the level and the stability of the electronic noise. A new mechanics moveable in the horizontal plane will allow to position the detector in the centre of the beam profile, thereby minimising the edge effect.

Complementary investigations of the detector should be performed using the proton test facility. The detector surface should be scanned with a well

defined, narrow proton beam, notably to study the edges of the detector. If unwanted effects will turn out to be too large, a thin collimator can be installed to cover the edges of the detector.

A better vacuum in the spectrometer will reduce the probability of rest gas ionisation and thus also the amount of uncorrelated background. Further investigations to identify sources of background should be performed (e.g., with conversion electron sources inside the spectrometer). Also the stability of the neutron beam monitor has to be improved. To exclude fluctuations of the magnetic field ratio r_{B} a monitoring system based on the nuclear magnetic resonance of protons has been developed and is ready for installation [29].

With these improvements in place a measurement of a with a total uncertainty of the order of $\Delta a/a \approx 1\,\%$ should be in reach. A new beamtime is envisaged for spring 2011.

A Appendix

A.1 Detector voltages

Each detector needs a special set of voltages to be operated correctly. These voltages are given by the manufacturer. Tables A.1, A.2, and A.3 show the values for the two fully functional detectors and the test detector (usually called "dummy"). On the dummy only two pads were working from the beginning. It was purchased for test purposes for a lower price. Table A.1 also explains the abbreviations used for the different supply voltages. These abbreviations are also printed on the voltage converter boards described in sect. 4.4.5.

Voltage	description	Pad 1 [V]	Pad 2 [V]	Pad 3 [V]
BC	back contact	-130	-135	-138
R1	first ring	-21	-16	-8
BR	bias ring	-140		
RX	last ring	-230		
IG	inner guard ring	-17		
FD	FET drain	9		
RD	reset diode	-15		
CSS	current source source	-8.89		
CSG	current source gate	-4.17		

Table A.1: Supply voltages for detector 1 (production code 44-S02). If only the voltage for pad 1 is given, it is common for all three pads.

Voltage	Pad 1 [V]	Pad 2 [V]	Pad 3 [V]
BC	-132	-140	-140
R1	-21	-14	-15
BR	-142		
RX	-230		
IG	-17		
FD	9		
RD	-15		
CSS	-8.89		
CSG	-4.17		

Table A.2: Supply voltages for detector 2 (production code 44-S04). If only the voltage for pad 1 is given, it is common for all three pads.

Voltage	Pad 1 [V]	Pad 2 [V]	Pad 3 [V]
BC	-140	-140	-140
R1	-15	-15	-15
BR	-148		
RX	-180		
IG	-17		
FD	9		
RD	-15		
CSS	-8.89		
CSG	-4.17		

Table A.3: Supply voltages for the "dummy" detector (production code 44-S07). If only the voltage for pad 1 is given, it is common for all three pads.

A.2 Instrument control programs

The beamtimes of *a*SPECT are quite long. In 2007/2008 in total 80 beam days were used. As the beamtime is too valuable to shut down the instrument over night and it is very difficult to do permanent shifts over this long time with limited manpower, a set of programs was developed that allows fully automatic measurements. The hardware setup is explained in sect. 5.2.2. On each of the computers LabVIEW programs are used to control the instrument[1]. Some of the programs have to be started for an automised measurement, others are optional.

A.2.1 DAQ PC

The readout of the detector has already been explained in sect. 4.4.4. However, for the automised measurements a complied version of the DAQ control program is used. LabVIEW allows to compile programs into normal executable files which can then be started from the command line without having to start LabVIEW. This turned out to run much more stable than the uncompiled version. Furthermore the compiled version can be started with a simple batch script that automatically restarts the program if it should crash. This helps to avoid loss of beamtime due to program crashes during the night. The compiled program used for measurements with automated shutter movements is called "`aSPECT_DAQ_SDD`", the batch file for automated measurements is "`run2.bat`". Both files are in the home folder of the user "`aspect`" in the sub-folder "`/LabVIEW Data/app`". Additionally, a logfile of the movements of the neutron shutter is written by "`aSPECT_DAQ_SDD`".

A.2.2 Decode PC

The decode PC is an additional PC that helps to distribute the work load better, but it is not absolutely needed. This PC was used during the beamtime to run two programs.

The first program decodes the data from the detector. After a measurement is finished, the DAQ PC sends a signal to the decode PC which

[1] Except the data server, which is only used for data storage.

accesses the file on the data server, decodes it and displays the generated pulse-height histograms from the last four measurements. The histograms are also sent back to the DAQ PC. For measurements with shutter movements during one file "`decode_split.vi`" is needed, otherwise the simpler version "`decode.vi`" can be used.

A second program called "`watchdog.vi`" can be started to monitor if the automated measurement is still running. This program simply checks the date and time of the last data file written to the data server. If that file is older than five minutes, the program sends an email to a special server at the ILL which converts the email to a text message and sends it to a previously registered mobile phone.

A.2.3 Magnet control PC

The most important task of the magnet PC is to read out the temperature sensors of the spectrometer. 20 temperature sensors are placed on different points inside the spectrometer. The sensors are read out by one Keithley voltmeter in a ring mode, this means a special switching box connects one sensor after the other to the voltmeter. Each value is transferred to the PC via GPIB where the values are displayed and stored in a logfile by a LabVIEW program. This program was developed by Cryogenics Ltd., the manufacturer of the magnet.

Besides the magnet temperature readout this computer can also be used to read and log pressures with the "`Maxigauge.vi`". This program reads pressures from up to 6 pressure gauges connected to a Pfeiffer TPG 256 A Maxiguage pressure sensor controller. The controller is connected to the PC via RS232.

Furthermore, during the beamtime also the high voltages on the detector and on one side of the upper $\vec{E} \times \vec{B}$ electrodes were set and read out with this PC, with the programs "`HV control_Grenoble-switched supplies`" and "`ExB control_Grenoble-switched supplies`". The voltages are set by two FUG HCN 35-35000 power supplies. Each one has an analogue input. An input voltage of 0 to 10 V scales to an output voltage of 0 to 35 kV. To produce the input voltage USB-to-analogue converters (UTA12 by Elektro-Automatik) are used. They convert a digital input via the USB port to an analogue voltage.

A.2.4 Control PC

The control PC is the central hub for the instrument control. The Data Socket server is running on this machine, it controls and reads the analysing plane voltage, and performs several other tasks.

To read and set the analysing plane voltage two programs are used. "`read AP_2.vi`" reads the voltage from the multimeter and writes it to a logfile, to change the voltage "`ramp AP_with_mean.vi`" is used.

The neutron counter is read with the "`Read n counter_mx2.vi`", the values are published and written into the logfile of the analysing plane voltage. Furthermore, this program controls the movement of the neutron shutter by operating the USB relay card.

The most important program running on the control PC is the program "`Control DAQ_2.5.vi`". As the name already implies, this program controls the other programs during the automated measurement cycles. A text file is used as input. Each line contains the information for one measurement cycle: The analysing plane voltage, the times to measure with each shutter state, and the settings of the USB controlled relays. The program reads the content from the file into a two-dimensional array when it is started. Then it reads the values from the first line, signals the desired voltage to the ramping program, waits until the ramping is finished and starts the measurement. After the measurement is finished, the next line is read and the procedure repeated. After each measurement a line in a logfile with the most important information is written.

A.3 ROOT data structure

The raw data from the sADC has a quite inconvenient structure to work with, thus several output files are produced at different stages of the data analysis. As described in sect. 4.4.4 the data is transferred to the structure of the ROOT data analysis framework with a custom program called "`online_decode`". During the decoding process a file with pulse-height histograms for each measurement and detector channel is produced for a quick but not very precise analysis. This file is usually called "`histograms.root`". These histograms are integrated within pre-set limits to produce a text file with the count rates. The most important output of the decode routine is

a file containing a tree with information about the measurement.

A tree is a predefined data structure in the ROOT framework and is meant to store many objects each containing the same type of information. In our case each event from the DAQ contains the same type of information. The tree structure is optimised to reduce disk space and enhance access speed. It consists of several branches, each containing a specified information of each event. A branch can be any C/C++ structure, like integers, doubles or arrays. During the decoding process, the events are read one by one from the raw data file, analysed, and filled into the tree. In the tree each event is assigned a number, according to the filling process. Detailed information can be found in the ROOT user guide [62].

A.3.1 Decode tree

A file containing this tree is created by the "`online_decode`" routine. Usually the name of this file consists of the same number as the raw data file, but with "`.root`" as file name extension. The tree consists of 9 branches that are used for the analysis:

- The timing information is contained in the branches "`timestamp`" and "`time_interval`". The "`timestamp`" represents the number of clock cycles of the sADC. In the raw data structure only 30 bit are reserved for this value. With a clock frequency of 20 MHz, this leads to an overflow every 53.7 s. If the length of the measurement is longer, the "`timestamp`" starts at 0 again and the "`time_interval`" is increased by one. Thus the time T_{event} at which an event occurred can be calculated for every event as:

  $$T_{\text{event}} = \frac{t_{\text{S}}}{2 \cdot 10^7} + t_{\text{I}} \frac{2^{30}}{2 \cdot 10^7}, \tag{A.1}$$

  where t_{S} is the value of the "`timestamp`" and t_{I} the "`time_interval`".

- "`time_diff_us`" gives the time difference of the current to the previous event in microseconds. This value is calculated from T_{event} for two consecutive events and stored for practical reasons.

- "`nslices`" is the length of the event as number of ADC bins.

- "adc_slices" is an array with the length specified in "nslices". It contains the single values of each ADC bin that was stored around the event.
- "Baseline_value" is the average value of the first 15 ADC bins, calculated during the decode process.
- "HistMax" is the highest ADC value of each event. Together with "Baseline_value" a simple pulse-height can be calculated.
- The type of the event is classified in "evtype". Normal data events are type 1, events from the temperature sensor type 3, and type 2 is used for events that were written in the heartbeat mode of the sADC.
- "channel_id" is the channel of the sADC in which the event occurred.

Two more branches ("badflags" and "good_events'') are obsolete. The routine was originally developed for the analysis of the data from the beamtime at the FRM-II and only adapted to the new detector.

A.3.2 Fit tree

The fit routine described in sect. 6.1 reads the data from the decode tree and the logfile of the shutter movements, fits each event, and writes the results to a second tree for each measurement file. These trees are all written in an output file, the same file for all fit trees. The branches of the fit tree are:

- "shutter" is the status of the automated neutron shutter, as described in table 6.3. For measurements without shutter movements during one file status -1 is assigned.
- The status of the fit (see table 6.2) is stored in "fit_status".
- "voltage" is the voltage of the analysing plane of the current file.
- "y_0", "x_0", and "A" are the resulting parameters of the fit.
- From the parameters of the fit, the pulse-height is calculated and stored in "pulseheight".

- "`chisqr`" and "`NDoF`" are the χ^2 and the number of degrees of freedom of the fit, respectively.

For the analysis the fit tree is loaded as a so-called friend tree of the decode tree. Thus, if an event is accessed, the information from both the decode and the fit tree is loaded into memory.

Bibliography

[1] S. K. Lamoreaux and R. Golub. Experimental searches for the neutron electric dipole moment. *J. Phys. G*, 36(10):104002, 2009.

[2] C. Amsler *et al.* Review of Particle Physics. *Phys. Lett. B*, 667:1+, 2008.

[3] S. Arzumanov *et al.* Neutron life time value measured by storing ultracold neutrons with detection of inelastically scattered neutrons. *Phys. Lett. B*, 483(1-3):15 – 22, 2000.

[4] A. Serebrov *et al.* Measurement of the neutron lifetime using a gravitational trap and a low-temperature Fomblin coating. *Phys. Lett. B*, 605(1-2):72 – 78, 2005.

[5] J. D. Jackson *et al.* Possible Tests of Time Reversal Invariance in Beta Decay. *Phys. Rev.*, 106(3):517 – 521, 1957.

[6] B. Povh *et al. Particles and Nuclei*. Springer, Berlin, Heidelberg, New York, 3rd edition, 2002.

[7] E. Fermi. Versuch einer Theorie der β-Strahlen. *Z. Phys.*, 88(3-4):161 – 177, 1934.

[8] T. D. Lee and C. N. Yang. Question of parity conservation in weak interactions. *Phys. Rev.*, 104(1):254 – 258, 1956.

[9] C. S. Wu *et al.* Experimental test of parity conservation in beta decay. *Phys. Rev.*, 105(4):1413 – 1415, 1957.

[10] G. Gamow and E. Teller. Selection rules for the β-disintegration. *Phys. Rev.*, 49(12):895 – 899, 1936.

[11] F. Glück *et al.* Measurable parameters of neutron decay. *Nuc. Phys. A*, 593(2):125 – 150, 1995.

[12] A. Salam. *in Elementary Particle Theory: Relativistic Groups and Analyticity (Nobel Symposium No. 8), edited by N. Svartholm.* Almqvist and Wiksell, Stockholm, 1968.

[13] S.L. Glashow. Partial-symmetries of weak interactions. *Nucl. Phys.*, 22(4):579 – 588, 1961.

[14] S. Weinberg. A model of leptons. *Phys. Rev. Lett.*, 19(21):1264 – 1266, 1967.

[15] N. Cabibbo. Unitary symmetry and leptonic decays. *Phys. Rev. Lett.*, 10(12):531 – 533, 1963.

[16] M. Kobayashi and T. Maskawa. CP-Violation in the Renormalizable Theory of Weak Interaction. *Prog. Theor. Phys.*, 49(2):652 – 657, 1972.

[17] H. Abele. The neutron. Its properties and basic interactions. *Prog. Part. Nucl. Phys.*, 60(1):1 – 81, 2008.

[18] F.E. Wietfeldt *et al.* acorn: An experiment to measure the electron-antineutrino correlation in neutron decay. *Nucl. Instr. and Meth. A*, 611(2-3):207 – 210, 2009.

[19] V.K. Grigorev *et al.* Experimental test of parity conservation in beta decay. *Sov. J. Nucl. Phys.*, 6:239, 1968.

[20] Chr. Stratowa *et al.* Ratio $|\frac{g_A}{g_V}|$ derived from the proton spectrum in free-neutron decay. *Phys. Rev. D*, 18(11):3970 – 3979, 1978.

[21] J. Byrne *et al.* Determination of the electron-antineutrino angular correlation coefficient a_0 and the parameter $|\lambda| = |G_\mathrm{A}/G_\mathrm{V}|$ in free neutron β-decay from measurements of the integrated energy spectrum of recoil protons stored in an ion trap. *J. Phys. G*, 28:1325 – 1349, 2002.

[22] O. Nachtmann. Relativistic Corrections to the Recoil Spectrum in Neutron β-Decay. *Z. Phys.*, 215(5):505 – 514, 1968.

[23] C. Habeck. *Experimental determination of the weak coupling constant ratio G_a/G_v in neutron decay.* PhD thesis, University of Sussex, 1997.

[24] P. G. Dawber *et al.* Determination of the electron-antineutrrino correlation coefficient a in neutron β-decay by measurement of the integrated proton spectrum. *Nucl. Instr. and Meth. A*, 440(3):543 – 547, 2000.

[25] M. Simson. First Measurements with the New Neutron Decay Spectrometer aSPECT at the Munich Research Reactor, Diploma Thesis, 2006. Technische Universität München.

[26] J.D. Jackson. *Classical Electrodynamics.* John Wiley & Sons, New York, Chinchester, Brisbane, Toronto, Singapore, 2nd edition, 1975.

[27] F. Glück *et al.* The neutron decay retardation spectrometer aSPECT: Electromagnetic design and systematic effects. *Europhys. J. A*, 23(1):135 – 146, 2005.

[28] G. Konrad. PhD thesis, Johannes Gutenberg Universität Mainz, 2010.

[29] F. Ayala Guardia. PhD thesis, Johannes Gutenberg Universität Mainz, 2010.

[30] R.O. Dendy. *Plasma Dynamics.* Claredon Press, Oxford, 1990.

[31] R. Muñoz Horta. *First measurements with the aSPECT spectrometer.* PhD thesis, Johannes Gutenberg Universität Mainz, 2010.

[32] S. Baeßler *et al.* First measurements with the neutron decay spectrometer aSPECT. *Europhys. J. A*, 38(1):17 – 26, 2008.

[33] C. Kittel. *Einführung in die Festkörperphysik.* Oldenbourg, München, 14^{th} edition, 2006.

[34] G. Lutz. *Semiconductor Radiation Detectors.* Springer, Berlin, Heidelberg, New York, 1st edition, 1999.

[35] H. Bethe. Zur Theorie des Durchgangs schneller Korpuskularstrahlen durch Materie. *Ann. Phys.*, 397(3):325 – 400, 1930.

[36] F. Bloch. Zur Bremsung rasch bewegter Teilchen beim Durchgang durch Materie. *Ann. Phys.*, 408(3):285 – 320, 1933.

[37] E. Gatti and P. Rehak. Semiconductor drift chamber - an application of a novel charge transport scheme. *Nucl. Instr. and Meth. A*, 225(3):608 – 614, 1984.

[38] M. Simson *et al.* Detection of low-energy protons using a silicon drift detector. *Nucl. Instr. and Meth. A*, 581(3):772 – 775, 2007.

[39] G. Petzoldt. *Measurement of the electron-antineutrino angular correlation coefficient a in neutron beta decay with the spectrometer aSPECT.* PhD thesis, Technische Universität München, 2007.

[40] A. Mann *et al.* A sampling ADC data acquisition system for positron emission tomography. *Nuclear Science, IEEE Transactions on*, 53(1):297 –303, 2006.

[41] B. Grube. *A Trigger Control System for COMPASS and a Measurement of the Transverse Polarization of* Λ *and* Ξ *Hyperons from Quasi-Real Photo-Production.* PhD thesis, Technische Universität München, 2006.

[42] R. Brun and F. Rademakers. ROOT - An Object Oriented Data Analysis Framework. *Nucl. Instr. and Meth. A*, 389(1-2):81 – 86, 1997.

[43] J.F. Ziegler *et al.* SRIM - The Stopping and Range of Ions in Matter. Computer Program. http://www.srim.org, 2008.

[44] M. Popp *et al.* Modeling the energy response of pn-CCDs in the 0.2–10 keV band. *Nucl. Instr. and Meth. A*, 439(2 - 3):567 – 574, 2000.

[45] P. Hovington *et al.* CASINO: A new monte carlo code in C language for electron beam interaction - part I: Description of the program. *Scanning*, 19(1):1 – 14, 1997.

[46] G. Hölzer *et al.* $K_\alpha 1,2$ and $K_\beta 1,3$ x-ray emission lines of the $3d$ transition metals. *Phys. Rev. A*, 56(6):4554 – 4568, 1997.

[47] J.A. Bearden. X-Ray Wavelengths. *Rev. Mod. Phys.*, 39(1):78 – 124, 1967.

[48] R.G. Helmer and C. van der Leun. Recommended standards for γ-ray energy calibration (1999). *Nucl. Instr. and Meth. A*, 450(1):35 – 70, 2000.

[49] S. J. B. Reed and N. G. Ware. Escape peaks and internal fluorescence in X-ray spectra recorded with lithium drifted silicon detectors. *J. Phys. E*, 5(6):582 – 583, 1972.

[50] SPECS GmbH Surface Analysis and Computer Technology, Berlin. *PU-IQE 11 Manual*, 2000. Version 1.2.1.

[51] A.R. Müller *et al.* PAFF, a low-energy, low-flux proton accelerator for detector tests. *Nucl. Instr. and Meth. A*, 582(2):395 – 400, 2007.

[52] A.R. Müller. *Characterization of solid deuterium as a source material for ultracold neutrons (UCN) and development of a detector concept for the detection of protons from the neutron decay.* PhD thesis, Technische Universität München, 2008.

[53] H. Abele *et al.* Characterization of a ballistic supermirror neutron guide. *Nucl. Instr. and Meth. A*, 562(1):407 – 417, 2006.

[54] M. Borg. *The anti neutrino-electron angular correlation coefficient a in free neutron decay: Tests of the Standard Model with the aSPECT-spectrometer.* PhD thesis, Johannes Gutenberg Universität Mainz, 2010.

[55] V.F. Sears. Neutron scattering lengths and cross sections. *Neutron News*, 3(3):26 – 37, 1992.

[56] H.D. Choi *et al. Database of Prompt Gamma Rays from Slow Neutron Capture for Elemental Analysis.* IAEA, Vienna, 2007.

[57] E. Browne and J.K. Tuli. Nuclear Data Sheets for A = 66. *Nucl. Data Sheets*, 111(4):1093 – 1209, 2010.

[58] B. Singh. Nuclear Data Sheets for A = 64. *Nucl. Data Sheets*, 108(2):197 – 364, 2007.

[59] J. Krempel. *Optimierung und Durchführung einer Beta-Asymmetriemessung im Zerfall polarisierter Neutronen, Diploma Thesis*, 2004. Universität Heidelberg.

[60] Z.K. Silagadze. A new algorithm for automatic photopeak searches. *Nucl. Instr. and Meth. A*, 376(3):451 – 454, 1996.

[61] W.R. Leo. *Techniques for Nuclear and Particle Physics Experiments.* Springer, Berlin, Heidelberg, New York, 2nd edition, 1994.

[62] The ROOT team. *ROOT An Object-Oriented Data Analysis Framework, User's Guide.* 5.26 edition, 2009.

Acknowledgements

I want to thank the following people:

Prof. Dr. Oliver Zimmer for introducing me to the world of neutron physics.

My Parents for supporting and helping me throughout my entire life.

My Brother Georg for always having a bed for me when I was in Munich.

Ida Berts for lots of motivation, but also the sometimes needed distraction, during the last months of my thesis.

Prof. Dr. Torsten Soldner for his help as instrument responsible during the beamtime and with the data analysis afterwards.

Michael Borg, Gertrud Konrad and Fidel Ayala Guardia, the PhD students working on the same project.

Dr. Hans-Friedrich Wirth and Heinz Angerer for the construction of the analogue electronics and the detector holder.

Igor Konorov and Alexander Mann for the development of our digital electronics and the firmware for it.

Adrian Niculae and PNSensor for supplying their great detectors.

All my other collaborators.

Everyone at the chair E18. Although I did not spend a lot of time there during my thesis I was always heartily welcomed when I came there.

Sebastian Pfister for many funny chats.

My fellow PhD students at the ILL for being good colleagues and also friends. And for many funny parties.

All my other relatives, friends, and colleagues.